

## Multifunctional epitaxial systems on silicon substrates

Srinivasa Rao Singamaneni,<sup>1,2,3,a)</sup> John Thomas Prater,<sup>1,2</sup> and Jagdish Narayan<sup>1</sup>

<sup>1</sup>Department of Materials Science and Engineering, North Carolina State University, Raleigh, North Carolina 27695, USA

<sup>2</sup>Materials Science Division, Army Research Office, Research Triangle Park, North Carolina 27709, USA

<sup>3</sup>Department of Physics, The University of Texas at El Paso, El Paso, Texas 79968, USA

(Received 8 June 2015; accepted 15 June 2016; published online 18 July 2016)

Multifunctional heterostructures can exhibit a wide range of functional properties, including colossal magneto-resistance, magnetocaloric, and multiferroic behavior, and can display interesting physical phenomena including spin and charge ordering and strong spin-orbit coupling. However, putting this functionality to work remains a challenge. To date, most of the work reported in the literature has dealt with heterostructures deposited onto closely lattice matched insulating substrates such as DyScO<sub>3</sub>, SrTiO<sub>3</sub> (STO), or STO buffered Si(100) using concepts of lattice matching epitaxy (LME). However, strain in heterostructures grown by LME is typically not fully relaxed and the layers contain detrimental defects such as threading dislocations that can significantly degrade the physical properties of the films and adversely affect the device characteristics. In addition, most of the substrates are incompatible with existing CMOS-based technology, where Si (100) substrates dominate. This review discusses recent advances in the integration of multifunctional oxide and non-oxide materials onto silicon substrates. An alternative thin film growth approach, called “domain matching epitaxy,” is presented which identifies approaches for minimizing lattice strain and unwanted defects in large misfit systems (7%–25% and higher). This approach broadly allows for the integration of multifunctional materials onto silicon substrates, such that sensing, computation, and response functions can be combined to produce next generation “smart” devices. In general, pulsed laser deposition has been used to epitaxially grow these materials, although the concepts developed here can be extended to other deposition techniques, as well. It will be shown that TiN and yttria-stabilized zirconia template layers provide promising platforms for the integration of new functionality into silicon-based computer chips. This review paper reports on a number of thin-film heterostructure systems that span a variety of ferroelectric, multiferroic, magnetic, photocatalytic, and smart materials. Their properties have been extensively investigated and their functionality found to be comparable to films grown on single-crystal oxide substrates previously reported by researchers in this field. In addition, this review explores the utility of using laser processing to introduce stable defects in a controlled way and induce magnetism and engineer the optical and electrical properties of nonmagnetic oxides such as BaTiO<sub>3</sub>, VO<sub>2</sub>, NiO, and TiO<sub>2</sub> as an alternative for incorporating additional magnetic and conducting layers into the structure. These significant materials advancements herald a flurry of exciting new advances in CMOS-compatible multifunctional devices. Published by AIP Publishing. [<http://dx.doi.org/10.1063/1.4955413>]

## TABLE OF CONTENTS

I. INTRODUCTION: OPPORTUNITIES AND CHALLENGES IN FUNCTIONAL HETEROSTRUCTURES INTEGRATION WITH SILICON .....	2
II. DOMAIN MATCHING EPITAXY (DME) .....	3
A. General DME framework .....	4
B. <i>In-situ</i> X-ray diffraction measurements: Demonstration of DME paradigm .....	5

<sup>a)</sup>ssingam@ncsu.edu

### III. INTEGRATION OF KEY BUFFER LAYER

PLATFORMS .....	7
A. MgO/TiN .....	7
B. c-YSZ .....	8

### IV. DME-GROWN EPITAXIAL LAYERS ON SI—GROWTH AND PHYSICAL PROPERTIES

A. Ferroelectrics .....	8
1. Pb(Zr <sub>0.2</sub> Ti <sub>0.8</sub> )O <sub>3</sub> (PZT) .....	8
B. Multiferroelectrics (ferroelectric and ferromagnetic heterostructures) .....	10
1. BiFeO <sub>3</sub> /La <sub>0.7</sub> Sr <sub>0.3</sub> MnO <sub>3</sub> (BFO/LSMO) .....	10
2. BTO/LSMO .....	14

3. Cr <sub>2</sub> O <sub>3</sub> .....	18
C. Magnetic layers .....	19
1. Permalloy (Py).....	20
2. CoFe <sub>2</sub> O <sub>4</sub> (CFO).....	21
3. La <sub>0.7</sub> Sr <sub>0.3</sub> MnO <sub>3</sub> /SrRuO <sub>3</sub> (LSMO/SRO).....	22
D. Emerging topological insulators .....	24
1. Sr <sub>3</sub> SnO (SSO).....	24
E. New transparent conductors.....	25
1. ZnO .....	25
F. Smart materials .....	28
1. VO <sub>2</sub> .....	28
2. NiO .....	29
V. DME-GROWN EPITAXIAL LAYERS—LASER INDUCED PHYSICAL PROPERTIES.....	30
A. BTO .....	30
B. VO <sub>2</sub> .....	31
C. TiO <sub>2</sub> .....	32
VI. CONCLUSIONS AND OUTLOOK.....	33
A. Mastering 2-D layer growth .....	34
B. Buffer layer reduction and interface optimization .....	34
C. Defect control and reliability issues.....	34
D. Innovative heterostructures .....	35

## I. INTRODUCTION: OPPORTUNITIES AND CHALLENGES IN FUNCTIONAL HETEROSTRUCTURES INTEGRATION WITH SILICON

There has been a tremendous increase in research related to the deposition of multifunctional thin film heterostructures for solid-state device technology.<sup>1–3</sup> Thin-layered materials offer a large range of tunability due to the interaction of the constituent components. In such layered heterostructures, defects and interfaces play a dominant role in determining the overall physical properties, and the material behavior may vary drastically from the bulk properties. Structural distortions, chemical diffusion, proximity effects, and magnetic or electronic exchange coupling at the material interfaces generate new degrees of freedom. Next-generation solid-state devices will require integration of various multifunctional materials on substrates of practical interest, particularly integration with existing complementary metal oxide semiconductor (CMOS) integrated circuits. This integration will necessitate epitaxial growth of different materials where total lattice misfit could range from 1% to 25% and higher.<sup>4–8</sup> The total strain that develops in multilayer thin-film heterostructures has three primary components: (a) lattice misfit arising from the differences in lattice constants between the film and the substrate; (b) thermal misfit arising from differences in coefficients of thermal expansion; and (c) microstructural strains arising from defects and alloying elements (dopants). The fundamental materials challenge in the synthesis and application of lattice-mismatched heterostructures is the enormous stresses and strains generated by the lattice parameter mismatch. Simple isotropic elasticity theory<sup>9</sup> gives the in-plane (IP) stress,  $\sigma_o$ , generated by lattice mismatch strain,  $\varepsilon$ , as

$$\sigma_o = 2G(1 + \nu) \varepsilon / ((1 - \nu)) \quad (1)$$

where G is the epilayer shear modulus (typically of order 50–100 GPa),  $\nu$  is the epilayer Poisson ratio (typically  $\sim 0.33$ ), and  $\varepsilon = (d_f - d_s)/d_s$  is the lattice mismatch strain ( $d_f$  and  $d_s$  are the film and substrate lattice planes, respectively). Accordingly, a lattice mismatch parameter difference of 1% between substrate and epi-layer generates a stress of  $\sim 2$  GPa in the epitaxial layer. This review primarily addresses the minimization of the lattice misfit, which is the dominant component of the strain in multifunctional heterostructures deposited on Si substrates.

According to the conventional wisdom of lattice matching epitaxy (LME), thin films grow as epitaxial single crystals with increasing difficulty as lattice misfit approaches 7%.<sup>10–13</sup> Many previous studies have focused on LME, where lattice relaxation occurs as a result of dislocation insertion at the interface.<sup>14,15</sup> Since these misfit dislocations (MDs) represent either a missing plane or an extra plane, the LME paradigm reduces to a matching of lattice planes and periodic insertion of misfit dislocations.<sup>4–8,16–18</sup> Extensive advanced electron microscopy studies have clearly established that under low mismatch conditions, film relaxation occurs only after growing beyond a critical thickness where mismatch stress build-up finally exceeds that associated with misfit dislocation introduction. At that point, dislocations nucleate at the free surface and propagate to the interface.<sup>16,18</sup> This relaxation process requires the propagation of dislocations with a critical resolved shear stress (the component of shear stress, resolved in the direction of slip), sufficient to realize slip in the film along an allowed slip systems.<sup>7</sup> The critical resolved shear stress is:  $(\sigma_{CRSS}) = (\sigma_{XX} = \sigma_{YY}) \cos \varphi \cos \lambda$ , where  $\varphi$  is the angle between stress direction and plane normal, and  $\lambda$  is the angle between stress direction and slip direction. If  $\sigma_{CRSS}$  is zero, dislocation will not glide, and thin film relaxation by dislocation insertion will not occur. The dislocations largely represent either missing planes under compressive stress (when the planar spacing of the film is larger than that of the substrate) or extra planes under tensile stress. In either case, thin film relaxation involves matching of lattice planes across the interface. Unfortunately, in the thin film heterostructures of interest, e.g., heterostructures with complex oxide layers on silicon, lattice misfit can range from being very small to very large, up to 25% and higher. Under conventional LME once the total misfit exceeds  $\sim 7\%$ , it has always been assumed that thin films will turn polycrystalline, with large-angle grain boundaries.<sup>10–13,19–28</sup> However, this has been found to be incorrect. Unlike the conventional thin film epitaxy framework, an alternative model, domain matching epitaxy (DME),<sup>4–8</sup> is able to handle both large and small misfits systems.

Of particular interest in this review are the perovskite oxides. These systems have been extensively studied for use in multifunctional devices due to the wide range of functional properties that they can afford, including ferromagnetism (FM) and superconductivity.<sup>1–3,29–31</sup> Most of the previous work on these materials has investigated thin films deposited on lattice-matched insulating *non-silicon* substrates such as SrTiO<sub>3</sub> (STO), MgO, and DyScO<sub>3</sub> (DSO), which are expensive and not used in semiconductor technology. To achieve optimal device characteristics, single

crystalline films of high crystalline quality will have to be prepared on large mismatched substrates. To expand chip function beyond current capabilities, a much better understanding of strain management across the misfit scale will be needed.

The incorporation of layers (both single composition and graded layers) and compliant interfaces, as discussed in the previous articles,<sup>32,33</sup> have commonly been utilized to manage lattice mismatches. Here, it is noted that prior to the advent of the original DME paper,<sup>4</sup> only one viable Si platform existed for oxide growth on Si substrates. Motivated by the search for new gate dielectrics to replace  $\text{SiO}_2$ , McKee and co-authors originally reported<sup>34</sup> on the molecular beam epitaxy (MBE) growth of epitaxial strontium titanate (STO) ( $d_0 = 3.905 \text{ \AA}$ ) on Si ( $d_0 = 5.431 \text{ \AA}$ ), at half monolayer (ML) coverage. This is notable because for the first time it provided a viable template (virtual substrate) for incorporating other epitaxial oxide films onto Si. In this growth, the STO unit cell is rotated by  $45^\circ$  about the  $\langle 001 \rangle$  axis (surface normal) with the silicon substrate, leading to a matching of  $\{220\}$  planes of the film with  $\{200\}$  planes of Si. The resulting lattice mismatch is 1.7% at room temperature. The use of MBE grown STO has now become ubiquitous. For instance, a group from IBM has reported<sup>35</sup> on the deposition of ferroelectric (FE)  $\text{BaTiO}_3$  (BTO) thin film on Si (100) using a STO buffer layer. Similarly, Eom and colleagues have reported<sup>36,37</sup> on the integration of giant piezoelectric lead magnesium niobate-lead titanate (PMN-PT) and  $\text{LaAlO}_3$  (LAO)/STO on Si (100). The former is of interest because of its potential application in advanced microelectromechanical systems (MEMS), while the latter has attracted a great deal of research interest due to the coexistence of ferromagnetism and superconductivity and the formation of a 2-dimensional (2D) electron gas at the interface. Finally, Chu *et al.* have demonstrated<sup>38</sup> the successful growth of ferroelectric  $\text{La}_x\text{Bi}_{1-x}\text{FeO}_3$  (where  $x = 0, 10, 15$ , and 20) with a conducting bottom electrode  $\text{SrRuO}_3$  (SRO) on the STO/Si (100) template.

Although STO buffer layers offer a viable platform for oxide growth, they do come with certain problems. For example, MBE growth of STO is performed at relatively high temperatures and in the presence of oxygen, which leads to the formation of a significant amorphous  $\text{SiO}_x$  layer at the interface due to oxygen diffusion through the film during growth. This layer is generally undesirable. Among other things, it can interfere with establishing epitaxial registry and the formation of electrical contacts. Depending on the growth conditions and STO thickness, the as-grown strain state of epitaxial STO on Si (100) can vary from compressive to tensile.<sup>31,39</sup> Also, the STO is usually very thin, well below the critical thickness ( $\sim 4 \text{ nm}$ ) required for dislocation insertion. Thus, the buffer layer has residual unrelaxed strain, which can become the source of defects during device operation that can adversely affect the physical properties of the heterostructures. In addition, the thermal expansion of Si is  $3.6 \times 10^{-6} \text{ K}^{-1}$  and is  $8.8 \times 10^{-6} \text{ K}^{-1}$  for STO. As a result, thermal stresses on the order of 0.5% are generated in the film upon cooling from  $1000^\circ\text{C}$ . This can lead to an additional biaxial tensile strain which in ferroelectric films can

produce a tensile strain in the film plane that favors the polar axis lying in-plane (IP) rather than out-of-plane (OOP).<sup>31</sup> Finally, the Si substrate imposes certain mechanical boundary conditions that differ from oxides, and it critically affects the piezoelectric response in electromechanical devices.<sup>36,37</sup> These effects will vary from system to system. Thus, it is important to develop alternative buffer systems that can expand the parameter space available for optimizing film morphologies and addressing long-term device reliability issues.

The Pt/Ti contact technology has been extensively used by many research groups.<sup>40-43</sup> However, this poses additional integration issues. Recent work<sup>40</sup> suggests that the Pt/Ti technology may not produce reliable non-volatile ferroelectric random access memory (RAM) capacitors due to the unwanted generation of pyroelectric currents and in-diffusion of Ti along grain boundaries in polycrystalline films. The diffusion of Ti can adversely affect the composition, microstructure, and properties of ferroelectric layer during the heating process and in the presence of oxygen. This may be aggravated by the choice of deposition technique. For example, ion beam sputter deposition (IBSD) is known to produce damage at the electrode/ferroelectric interface that leads to significant fatigue and unacceptable device life times. Interestingly, the fatigue is practically absent in pulsed laser deposition (PLD) grown epitaxial films.<sup>40</sup> For lead-based ferroelectric-silicon heterostructures, an additional difficulty is derived from Pb cation diffusion into the silicon substrate during high-temperature growth. Such diffusion results in a lead-deficient oxide layer and the formation of non-ferroelectric pyrochlore and fluorite phases that degrade the performance of the final devices.<sup>31</sup>

To address these challenges, two novel buffer layers (one conductive TiN based and one insulating yttria-stabilized zirconia (YSZ) based) have recently been developed that can perform the dual role of epitaxial template and diffusion barrier.<sup>4-8</sup> In this review, a comprehensive overview of epitaxial integration of various model oxide/non-oxide systems on silicon substrates is presented that offers a new paradigm for growing nearly fully relaxed epitaxial layers on Si. It should be noted that none of the heterostructures presented here has been subjected to an actual industry-CMOS process flow with representative thermal annealing and contact metallization steps. However, previous works by Ramesh and co-authors<sup>44-46</sup> have done so with different polycrystalline and monocrystalline ferroelectric layers deposited on STO buffered Si (100) substrates. They have shown that the prototype devices could sustain industry standard CMOS processing cycles with no adverse effects. Similarly, we expect that the systems being proposed here should be able to survive standard CMOS processing cycles.

## II. DOMAIN MATCHING EPITAXY (DME)

As discussed above, most of the previous works on complex oxide films and heterostructures have been grown by either MBE or PLD on near lattice-matched substrates such as STO and STO-buffered Si substrates where conventional LME principles apply. The resulting films tend to be un-relaxed and contain trapped threading dislocations. The

advent of DME<sup>4–8</sup> by Narayan and coworkers has expanded our understanding on this important issue. Using this approach, it has been shown that epitaxial layers can be grown over a much wider range of lattice misfit conditions than previously believed not possible. An important feature of the domain epitaxy concept is that under large misfit conditions, most of the strain can be relieved during the nucleation step (first couple of monolayers of growth), thereby mitigating the need for separate dislocation nucleation and slip processes and facilitating the formation of misfit dislocation arrays that are well confined to the interface. This makes it possible for the rest of the film to be grown free of defects and lattice strains. This is particularly important for ferroelectrics, where large numbers of defects will result in depolarization fields that weaken the stability of the bistable polarization states, thereby degrading the device performance.

### A. General DME framework

DME<sup>4–8</sup> provides a generalized model for treating strain relief by matching integral multiples of lattice planes across the film-substrate interface. Under this scheme, lattice misfit values can range from quite small to very large. In the small misfit regime (typically less than 7%–8%) where the crystal structures of the film and substrate are similar, DME reduces to LME, i.e., matching of the same planes or lattice constants. In conventional LME, the initial or un-relaxed misfit strain ( $\epsilon_c$ ) is given by  $\epsilon_c = a_f/a_s - 1$ , where  $a_f$  and  $a_s$  are lattice constants of the film and the substrate, respectively. In LME, the  $\epsilon_c$  is usually taken to be less than 3%, (although it may extend up to 7%–8%), and the film and the substrate are assumed to be of the same or closely related crystal symmetry. For this case, direct dislocation nucleation at the interface would require extremely high activation energy and thus does not occur. Instead, the films are assumed to grow pseudomorphically up to a critical thickness, where it becomes energetically favorable for the film to contain dislocations.<sup>7,16–18</sup> As growth proceeds beyond the critical thickness, film relaxation commences gradually as dislocations first nucleate at the film surface (e.g., surface steps) and then glide down to the interface as half loops. This process provides the genesis for two threading dislocations per misfit dislocation that potentially end up being trapped in the film if the misfit dislocation fails to propagate across the entire width of the grain. Both surface roughness and compressive stress can help to promote dislocation nucleation. However, propagation is controlled by the lattice frictional stress and bonding characteristics of the film.

For LME, comprehensive analysis of the respective dislocations and their Burgers vectors do suggest that the predominant mechanism for stress relaxation in thin films will involve the nucleation of dislocation at the surface<sup>16,18</sup> and subsequent propagation down to the interface. *In-situ* TEM observations on growing islands appear to confirm that dislocation nucleation and propagation occur at the top of the islands once the critical thickness is exceeded.<sup>7</sup> However, several other related dislocation injection mechanisms have been reported in the literature. For instance, Dong and co-

authors<sup>47</sup> have analyzed various misfit dislocation nucleation and stress relaxation mechanisms using molecular dynamics. Their results suggest that the formation of voids within the film can produce regions of stress concentrations near the void surface parallel to the substrate. Again, once a critical film thickness is reached, dislocations will form that relax most of the misfit strain. They demonstrate that the dislocation nucleation mechanism is intimately associated with the surface roughness and the resulting stress concentration. Similarly, Freund<sup>48</sup> has identified various sources of heterogeneous nucleation for dislocation formation, such as foreign matter on the growth surface of the substrate in the form of chemical contamination or handling debris, crystallographic ledges or steps on the growth surface of the substrate, stacking fault loops within the film, or the coalescence of vacancies and compositional gradients of alloying elements. In a related review article,<sup>49</sup> Vdovin discussed that, for low misfit (<1%) systems, the formation of three dimensional misfit dislocation (3D-MD) networks is an indication that MD multiplication and other dislocation interactions are occurring, consistent with the dislocation half-loops spreading downwards toward the substrate interface. It was concluded that inhomogeneity at the nanometer scale and intrinsic point defects formed in the epilayer and substrate markedly affect dislocation generation, propagation, and multiplication. Finally, using *in situ* ultra-high vacuum transmission electron microscopy, LeGoues and co-workers have investigated<sup>50</sup> the growth of Ge islands on Si (001) substrate. They argued that the nucleation of dislocations and strain relief originated at the edges of the island. This seems likely only in systems where dislocation glide is possible along the plane parallel to the interface.

In domain matching epitaxy (DME), the initial lattice misfit strain ( $\epsilon = d_f/d_s - 1$ ) can be very large. Here, the strain is accommodated by matching of  $m$  planes of the film with  $n$  planes of the substrate (hereafter referred to as a domain), where  $m$  and  $n$  are simple integers. The film and the substrate crystal structures and matching lattice planes can be quite different, as long as they share similar crystal symmetry. In cases where the misfit does not perfectly correspond to a single matched domain, then the size of the domain spacing of matched planes between misfit dislocations can be varied in a systematic way to accommodate the additional misfit. This matching of integral multiples of lattice planes leaves a residual strain of  $\epsilon_r$  given by

$$\epsilon_r = (md_f/nd_s - 1). \quad (2)$$

In the case of a perfect matching,  $md_f = nd_s$ , and the residual strain  $\epsilon_r$  is zero. If  $\epsilon_r$  is finite, then two domains of differing size may alternate with a certain frequency to provide for a perfect matching and a complete lattice relaxation according to

$$(m + \alpha)d_f = (n + \alpha)d_s, \quad (3)$$

where  $\alpha$  is the frequency factor. For example, if  $\alpha = 0.5$ , then  $m/n$  and  $(m+1)/(n+1)$  domains alternate with an equal frequency.

Assuming  $d_f > d_s$ , we have  $n > m$ . Therefore,

$$n - m = 1. \quad (4)$$

From Equations (2) through (4), we can derive

$$(m + \alpha) = 1. \quad (5)$$

Equation (5), plotted in Fig. 1, basically governs the domain epitaxy. At large strains, >8%, a critical thickness calculation predicts that dislocation formation is possible after the deposition of just a few monolayers. In this case, film relaxation is predicted to occur during the initial stages of film growth resulting in a complete relaxation of the strain with no dislocation nucleation barrier. This has been borne out by *in situ* XRD measurements (discussed in Section II B). Figure 1 shows a general plot of misfit percent strain as a function of the ratio of film/substrate major planes matching across the interface. It should be noted that a 45° rotation in some cubic systems, such as STO/Si (100), can involve matching of {200} and {220} planes of the film and the substrate, respectively. The plot in Fig. 1 provides a unified framework for LME and DME with misfit strain ranging from 2% to 50% (50% corresponding to 1:2 matching). If the domain matching is not perfect, then epitaxy is achieved by accommodating the additional misfit by periodically changing the domain size, controlled by the parameter  $\alpha$ .

Consistent with the DME paradigm, complete strain relaxation of large lattice misfits has been demonstrated. Using high-resolution transmission electron microscopy (HRTEM) and X-ray diffraction (XRD), Pant and co-authors<sup>51</sup> have investigated the strain relaxation mechanisms for nonpolar (1 1 -2 0) *a*-plane ZnO epitaxy on (1 -1 0 2) *r*-plane sapphire, where the in-plane misfit in the two orthogonal directions is -1.5% for [0 0 0 1] ZnO || [1 -1 0 -1] sapphire and -18.3% for [-1 1 0 0] ZnO || [-1 -1 2 0] sapphire, respectively. In the large misfit [-1 1 0 0] ZnO direction, the misfit strains are fully relaxed at the growth temperature, and only thermal misfit and defect strains,

which cannot be relaxed fully by dislocation slip, remain upon cooling. Interestingly, in the small misfit direction, the lattice misfit strain is barely relaxed at the growth temperature. As a result, additive unrelaxed lattice and thermal misfit and defect strains all contribute to the measured strain. The XRD measurements of lattice parameters show that this observed anisotropic in-plane biaxial strain leads to a distortion of the hexagonal symmetry of the ZnO basal plane. HRTEM investigations of the interface confirm the presence of the anisotropic strain relaxation process and reveal that the kinetics related to strain relaxation differs substantially between large and small misfit conditions. This leads to the finding that misfit relaxation can be more easily realized in large (not small) misfit systems. This may not be surprising, since the driving force for relaxation is greater in higher mismatch systems. In large misfit systems with critical thickness 1–2 monolayers, dislocations nucleate at the surface steps and are immediately incorporated into the interface; dislocation glide is not required. However, in small misfit systems, dislocation nucleation and propagation are dictated by critical resolved shear stress along the active slip planes. If the critical resolved shear stress is very small or zero along the active slip planes, which is the case for ⟨0001⟩ZnO/⟨0001⟩sapphire, for example, then film relaxation becomes problematic.

## B. *In-situ* X-ray diffraction measurements: Demonstration of DME paradigm

The concept of DME has been most clearly illustrated for the ZnO/aAl<sub>2</sub>O<sub>3</sub> system using *in-situ* x-ray diffraction measurements.<sup>8</sup> The details of the lattice relaxation process during initial stages of ZnO growth on sapphire ( $\alpha$ -Al<sub>2</sub>O<sub>3</sub>) (0001) substrates were studied by *in-situ* XRD study using the UNI-CAT undulator beam line at the Advanced Photon Source. In these experiments, a pulsed laser-ablation growth chamber was mounted on the 212 x-ray diffractometer to enable surface scattering measurements in both specular and off-specular directions during initial stages of thin film growth. Time-slice x-ray crystal truncation rod (CTR) measurements made after each excimer laser ablation pulse revealed that the surface structure transients associated with ZnO clustering and crystallization continue for about 2 s following the short  $\sim 5\ \mu\text{s}$  laser burst. Specular CTR anti-Bragg measurements at the sapphire (0 0 5/2) position showed only one well-defined growth oscillation, indicating three-dimensional (3D) growth rather than layer by layer growth. Off-specular CTR measurements along the (H, 0, -H, 0.3) direction showed thermally activated relaxation of the 15.44% lattice mismatch associated with the matching of the (2110) planes of ZnO align with (0110) planes of sapphire (representing a 30° in-plane rotation of the ZnO about the *c* axis). As shown in Fig. 2(a), a broad, nearly relaxed ZnO IP diffraction peak appears after the deposition of 3 monolayers at 400 °C ( $\sim 25$  pulses/monolayer), while a sharper and more fully relaxed ZnO peak appears after only 2 monolayers at 585 °C as illustrated in Fig. 2(b). Here, the x-axis represents reciprocal lattice units (rlu). After 150 pulses at 585 °C, the peak occurs at H = 0.845 corresponding to the fully relaxed

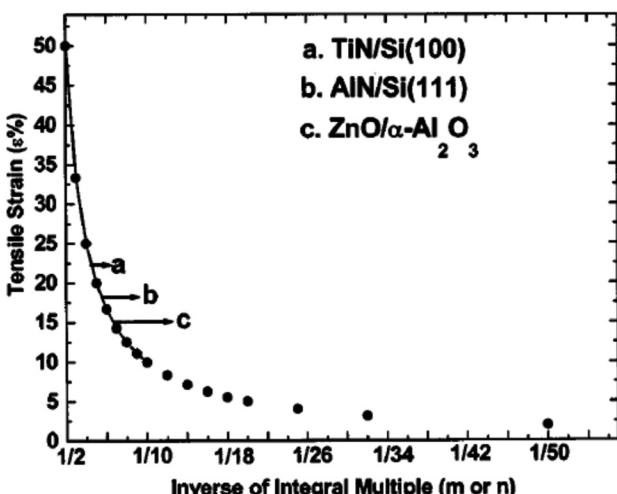


FIG. 1. Unified plot of strain versus film-substrate planar spacing ratio. Reprinted with permission from J. Narayan, Acta Mater. 61, 2703–2724 (2013). Copyright 2013 Elsevier.

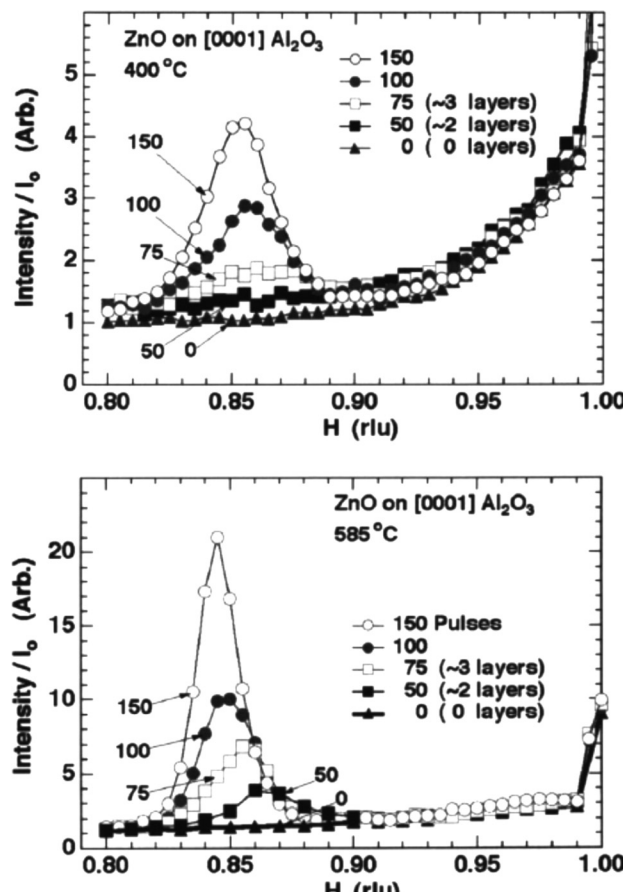


FIG. 2. *In-situ* X-ray surface diffraction measurements along the  $(H, 0, 2H, 0.3)$  direction showing the growth of ZnO films on sapphire with sapphire in-plane lattice parameter approaching  $H50.845$  corresponding to a fully relaxed position after a few monolayers. Here, the x-axis represents reciprocal lattice units (rlu). Reprinted with permission from J. Appl. Phys. **93**, 278–283 (2003). Copyright 2003 AIP Publishing LLC.

ZnO film. Subsequent measurements (not presented here) showed that incommensuration occurs within the first layer of the deposition, and the nature of the strain is compressive as expected for matching of “*a*” planes of ZnO ( $d = 3.2536 \text{ \AA}$ ) with underlying sapphire planes ( $d = 2.7512 \text{ \AA}$ ). These results clearly established that a rapid relaxation occurs for ZnO film grown on sapphire. The relaxation process was determined to be thermally activated since the ZnO thickness corresponding to full relaxation decreased as the deposition temperature increased. The relaxation process is consistent with the creation of dislocations that involves a single thermally activated nucleation and placement step. The nucleation barrier can be partially overcome by the presence of surface steps that form during the film growth process, while propagation to the interface occurs quite readily due to the proximity of the interface and the dynamic nature of the film at this stage of formation. On the other hand, if the critical thickness is large, as is the case for small-misfit systems, then film relaxation is delayed until the dislocations are energetically able to overcome the larger dislocation nucleation and propagation barriers. This results in misfit strain that is not fully relaxed. In addition, threading segments find it hard to fully expand to the edges due to blocking by other

dislocations and obstacles. As a result, a high-density of threading dislocations is retained and trapped within the film.

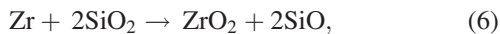
Both XRD and high resolution transmission electron microscopy (HRTEM) studies strongly suggest that the large lattice misfit is fully relaxed during the early stages of growth by incorporating a network of misfit dislocations, located at the interface with a spacing and distribution consistent with the large lattice misfit along the ZnO [01-10]//[2-1-10]  $\text{Al}_2\text{O}_3$  direction. The highly defective area was confined to dislocation cores located within 3–4 monolayers of the interface. In addition, the misfit dislocations extended across the width of the individual subgrains. This left very few threading dislocations within the sub-grains themselves. TEM images indicated that the density of threading dislocations with Burgers vector  $b = 1/3[11-20]$  was approximately  $10^7 \text{ cm}^{-2}$ , which is 3 orders of magnitude lower than normally observed for the misfit of this magnitude (15.44%). The density of stacking faults (planar defects) was estimated to be  $10^5 \text{ cm}^{-1}$ . It is interesting to note that most of the dislocations were confined to the ZnO/sapphire interface as expected for DME.<sup>4–8</sup> These findings have been confirmed in a number of recent reports<sup>52–56</sup> focused on similar heterostructures. This was consistently seen over the entire interface on different samples.<sup>57</sup> In comparison, Nagarajan *et al.*<sup>58</sup> reported a dislocation density of  $10^{12} \text{ cm}^{-2}$  for the case of nanoscale ferroelectric heterostructures grown on a lattice matched substrate STO. They also identified degradation of the ferroelectric properties in the vicinity of dislocations.

It should be commented that there are several other aspects of the film growth process that can affect final film quality. For example, film growth initiates at multiple sites across the substrate surface. These regions grow epitaxially on the substrate, but with slight misorientations (rotations and tilts), possibly due to small grain-to-grain variations in the strain relaxation processes, defect populations, and interactions between the different dislocation types. These misorientations remain after film coalescence leading to a mosaic-type microstructure composed of columnar subgrains separated by low-angle grain boundaries. In this context, layer-by-layer growth should favor larger subgrain sizes and generally improve film quality. Thus, good wetting between the film and the substrate, which is intimately related to chemical bonding at the interface, is critical. Likewise, the choice of the substrate can affect film quality. For example, problems can arise when one attempts to grow an epitaxial layer over a step edge, as the surface step height of the substrate is not necessarily matched by the out-of-plane inter-planar distance of the film. In addition, the symmetry difference between the diamond lattice of Si and the simple cubic lattice of a perovskite may result in the formation of twins and other domains, which could be detrimental for physical properties of film. The remainder of this review is organized as follows. In Section III, we will introduce two key epitaxial buffer layer platforms: TiN on Si (100) and YSZ on Si(100). These represent the first step in the integration of functional materials with silicon substrates. The use of these templates layers to grow ferroelectric, ferromagnetic materials, topological insulators (TIs),

transparent conductors, and semiconducting oxides will then be presented. These offer a wide range of properties, such as piezoelectricity, ferroelectricity, magnetism, and magnetoelectricity, as well as specific optical and electrical properties. Specifically, in Section IV A, recent results on the integration of multiferroic/ferroelectric materials such as  $\text{Pb}(\text{Zr},\text{Ti})\text{O}_3$  (PZT),  $\text{BiFeO}_3/\text{La}_{0.7}\text{Sr}_{0.3}\text{MnO}_3$  (BFO/LSMO), BTO/LSMO, and  $\text{Cr}_2\text{O}_3$  thin films will be presented. Section IV B will discuss the physical properties of ferromagnetic heterostructures such as Py,  $\text{CoFe}_2\text{O}_4$  (CFO), and  $\text{LSMO/SrRuO}_3$  (SRO), grown on silicon substrates. In Section IV C, we discuss the integration and resulting physical properties of  $\text{Sr}_3\text{SnO}$  (SSO), a candidate topological material. Section IV D presents the recent efforts in integration and physical property studies on epitaxial ZnO thin films with silicon substrate. Section IV E is devoted to smart semiconductors such as (i)  $\text{VO}_2$  and (ii)  $\text{NiO}$ . Finally, Section V will present options for laser processing of various films as an alternative means of introducing new properties, particularly ferromagnetism. We will then close with a conclusion and future outlook in Section VI.

### III. INTEGRATION OF KEY BUFFER LAYER PLATFORMS

Multifunctional thin film heterostructures grown directly on silicon substrates tend to form amorphous  $\text{SiO}_x$ , and other interfacial phases which inhibit epitaxial growth, and lead to reduced carrier mobility and reliability and enhanced aging. Platinum (Pt) has long been proposed<sup>40–43</sup> as an interfacial barrier between the ferroelectric and the underlying silicon. Although platinum is a relatively noble material, it has been found<sup>59</sup> to be a poor barrier for oxygen migration from the ferroelectric to the underlying silicon. Some have tried alloying Pt<sup>60</sup> ( $\text{Pt}_{1-x}\text{Ir}_x$  alloy and its oxides). This provides a superior diffusion barrier for species like oxygen and Si. But, alternative diffusion barriers are needed. A second aspect related to film growth on Si is the presence of the native amorphous oxide layer, which can directly interfere with epi growth. This can be solved by introducing a highly reactive cation (e.g., Ti or Zr) during the initial growth stage, which can chemically react with and remove the native oxide on the Si. Once the native oxide is removed, the epitaxial growth of film can take place. For example, in the case of  $\text{ZrO}_2$  barriers, the  $\text{SiO}_2$  amorphous layer is removed and destroyed by the following reaction:



where SiO is lost by evaporation. With these issues in mind, two new buffer layers have been emerged. Both cubic yttria stabilized zirconia (c-ysz) and tetragonal ysz provide suitable templates for oxides, despite their inferior diffusion barrier properties compared to TiN.

#### A. MgO/TiN

TiN is an ideal choice of material both as a template layer and a diffusion barrier. TiN buffer layers have proven to be mechanically robust, metallic, Si-compatible, and cost effective and have been widely employed as top and bottom

electrodes for dynamic RAM (DRAM) capacitors. More importantly, it can work as a barrier<sup>61</sup> to prevent hydrogen incorporation during the forming-gas anneal used in CMOS processing.

Details on the epitaxial growth and properties of epitaxial TiN films deposited on Si substrates by pulsed laser deposition are reported elsewhere.<sup>4</sup> Therein, it has been confirmed experimentally that the lattice misfit of 22.0% can be successfully accommodated. This is well above the critical strain (7%–8%) treated by conventional lattice matching.<sup>4–8</sup> Figure 3 shows a detailed HRTEM micrograph taken along the  $\langle 110 \rangle$  zone axis, clearly showing the atomic structure of the Si/TiN interface and the misfit dislocations associated with the alternating 3/4 and 4/5 domains. The corresponding diffraction pattern (shown in the inset) confirms cube-on-cube domain epitaxy for this system. It is interesting to note the matching of {111} extra half planes across the interface. From Fig. 2, the lattice misfit of 22% lies in the middle 3/4 and 4/5 matching, which explains the alternating widths of the domains. In fact with  $\alpha=0.5$  [Eq. (2)],  $3.5 d_{\text{Si}} = 19.01$  matches quite well with  $4.5 d_{\text{TiN}} = 19.08$  and represents the average size of domain predicted for a completely relaxed system with virtually no residual lattice misfit strain. Likewise, an analysis of the relevant interfacial and strain energy terms reveal a significant reduction in the total free energy of the observed domain matched configuration compared with the un-relaxed, coherently strained state.<sup>4,5</sup> The observed variations in the epitaxial growth are consistent with the minimum energy configurations predicted by the domain matching model. In addition, the detailed structural and microstructural investigations show that the TiN/Si interface is free of macroscopic oxidation, removed during initial deposition of Ti. The TiN has an additional advantage of being highly conductive. Thus, it can directly serve as the bottom electrode for ferroelectric capacitors<sup>61</sup> and GaN based light emitting diodes

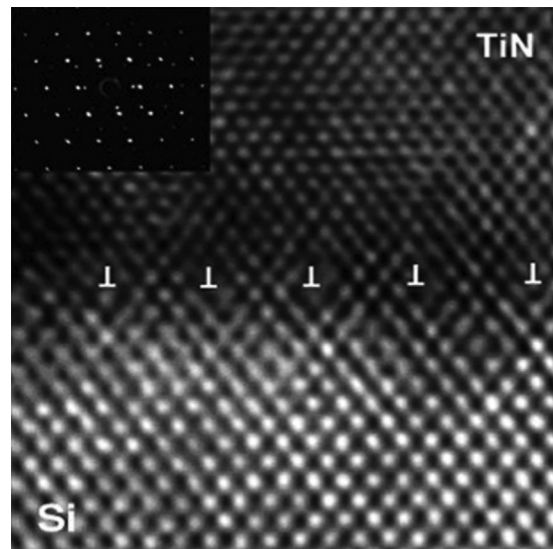


FIG. 3. HRTEM image of TiN/Si(100) interface with alternating 4/3 and 5/4 domains. Reprinted with permission from Appl. Phys. Lett. **61**, 1290–1292 (1992). Copyright 1992 AIP Publishing LLC.

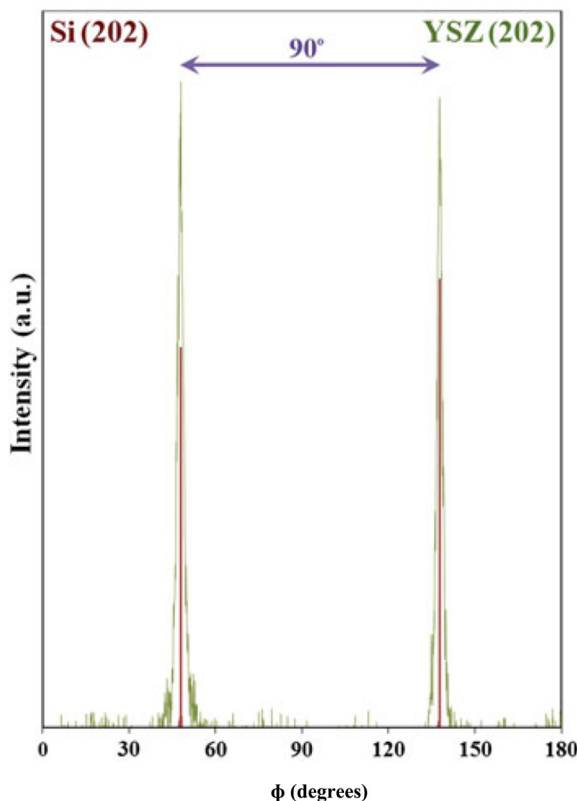


FIG. 4.  $\phi$ -scan XRD pattern acquired from YSZ (202). Reprinted with permission from Molaei *et al.*, J. Mater. Res. **27**, 3103–3109 (2012). Copyright 2012 Cambridge University Press.

(LEDs).<sup>62</sup> MgO ( $a = 4.216 \text{ \AA}$ ) has a near perfect lattice match with TiN ( $a = 4.240 \text{ \AA}$ ) and is among the most stable oxides. Thus, it provides an ideal cap for the TiN as one transitions over to other oxide growth. The MgO/TiN/Si system has proven to be a robust platform for subsequent growth of oxide-based heterostructures.

## B. c-YSZ

The epitaxial relationship between the YSZ film and the Si (001) substrate is established<sup>63</sup> as cube-on-cube growth:  $\{001\}_{\text{YSZ}} \parallel \{001\}_{\text{Si}}$  and  $\langle 100 \rangle_{\text{YSZ}} \parallel \langle 100 \rangle_{\text{Si}}$ . As seen in Fig. 4, the  $\phi$ -peaks from (202) reflections of YSZ and Si appear at the same azimuthal positions. This is consistent with the 4-fold symmetry present in both crystals and their similar lattice parameters ( $a_{\text{Si}} = 5.43$  and  $a_{\text{YSZ}} = 5.14 \text{ \AA}$ ).

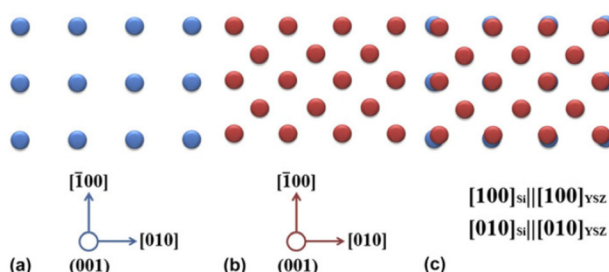


FIG. 5. Atomic arrangement at the (a) Si (001) surface, (b) YSZ (001) surface, and (c) YSZ/Si interface. Reprinted with permission from Molaei *et al.*, J. Mater. Res. **27**, 3103–3109 (2012). Copyright 2012 Cambridge University Press.

The atomic arrangement across the YSZ/Si interface is modeled in Fig. 5. The misfit strain across the YSZ/Si interface was calculated as  $\sim 5.3\%$  and is relaxed via the alternation of 18/17 and 19/18 domains with a frequency factor of about 0.7. The reactivity of this oxide with silicon is limited. As a result, relatively abrupt interfaces are realized experimentally. It should be mentioned that there is some formation of  $\text{SiO}_2$  as a result of oxygen diffusion through YSZ layer during subsequent YSZ growth. However, this does not affect YSZ epitaxy as the template has already been set in place.

## IV. DME-GROWN EPITAXIAL LAYERS ON Si—GROWTH AND PHYSICAL PROPERTIES

### A. Ferroelectrics

#### 1. $\text{Pb}(\text{Zr}_{0.2}\text{Ti}_{0.8})\text{O}_3$ (PZT)

Ferroelectric materials can be electrically switched between two stable electrical polarization states that will persist in the absence of a switching field. Their most widespread application is as a non-volatile memory<sup>64,65</sup> in which the ferroelectric fills the gap of a thin film capacitor. Depending on the polarity of the writing pulse, the capacitor is charged in one of two voltage states of opposite polarity. Unlike semiconductor capacitive memories (such as DRAMs, used in mobile and embedded applications), the ferroelectric capacitive memory is non-volatile and maintains its stored information even if depowered. Because of the very high effective dielectric constants of ferroelectrics, ferroelectric memories can be made very small. For instance, recently,  $30 \text{ Gbit cm}^2$  data storage densities have been demonstrated<sup>66,67</sup> for PZT films on a metallic oxide electrode. In addition, it has recently been proposed<sup>68</sup> that the incorporation of a ferroelectric as a gate oxide could decrease the sub-threshold slope below the intrinsic room temperature (RT) thermodynamic limit of  $60 \text{ mV dec}^{-1}$  of metal-oxide-semiconductor field effect transistors, enabling even lower voltage operation of CMOS devices.

PZT is the prototypical ferroelectric material with broad potential applications in nonvolatile memory devices, infrared sensors, and microelectromechanical systems.<sup>66,67</sup> In addition, strong and robust magneto-electric coupling has been reported when PZT is in contact with ferromagnetic layers. Extensive studies have been made on PZT films deposited on lattice matching oxide substrates such as STO.<sup>69–71</sup> For example, Wang and co-authors have grown r.f. sputtered epitaxial PZT(20/80) and PZT(53/47) thin films with a Pt bottom electrode onto Si(001) single crystal substrates by incorporating a Ag buffer layer.<sup>72</sup> In their work, Ag was easily grown epitaxially on hydrogen fluoride (HF)-etched Si(001) with cube-on-cube orientation relationship, even though the lattice mismatch between Ag (fcc,  $a = 4.09 \text{ \AA}$ ) and Si (diamond cubic,  $a = 5.43 \text{ \AA}$ ) is about 24.7%. The authors reported that both PZT(20/80) and PZT(53/47) thin films structures were single perovskite phase with a (001) orientation. They determined the orientation relationship to be  $\text{PZT}(001)[110] \parallel \text{Pt}(001)[110]$  and  $\parallel \text{Ag}(001)[110] \parallel \text{Si}(001)[110]$ . This observation can be explained by the DME epitaxial model in which four planes

of Ag match very well with the three planes of Si. The lattice mismatch between Pt (fcc,  $a = 3.92 \text{ \AA}$ ) and Ag is about 4.15%, while PZT(53/47) (rhombohedral,  $a = 4.07 \text{ \AA}$  and  $c = 4.15 \text{ \AA}$ ) has mismatch of 3.8% with respect to Pt.

Figures 6(a) and 6(b) show a plane-view TEM image and selected area diffraction (SAD) pattern of the PZT (53/47) thin film samples. The plane-view TEM image shows that low angle grain boundaries exist in the PZT (53/47) films with a large distribution of grain sizes varying from 300 to 700 nm. The SAD pattern confirms that the PZT film is a (001)-oriented single crystal. Figures 6(c)–6(e) show a cross-sectional TEM image and SAD patterns of the PZT (20/80)/Pt/Ag/Si film. No oxide layer is observed between Ag and Si. Figures 6(d) and 6(e) display the SAD pattern of

the Pt/Ag/Si structure and the SAD pattern of the PZT layer, respectively. The alignment of diffraction spots in three directions confirms the epitaxial relation between various layers. The ferroelectric data collected from these two samples are shown in Figs. 7(a) and 7(b). The PZT (20/80) samples show a remanent polarization of  $26 \mu\text{C}/\text{cm}^2$  and a coercive field of  $110 \text{ kV}/\text{cm}$ . The PZT (53/47) films show similar electrical properties with a remanent polarization of  $10 \mu\text{C}/\text{cm}^2$  and a coercive field of  $80 \text{ kV}/\text{cm}$ .

Subsequently, they successfully deposited low fatigue (001)-oriented epitaxial PZT on Si substrates with  $\text{LaNiO}_3$  (LNO) electrodes by rf sputtering using STO/TiN as buffer layers.<sup>73</sup> In-plane XRD pattern displayed in Fig. 8 indicates that the PZT layer grows cube-on-cube on the LNO layer.

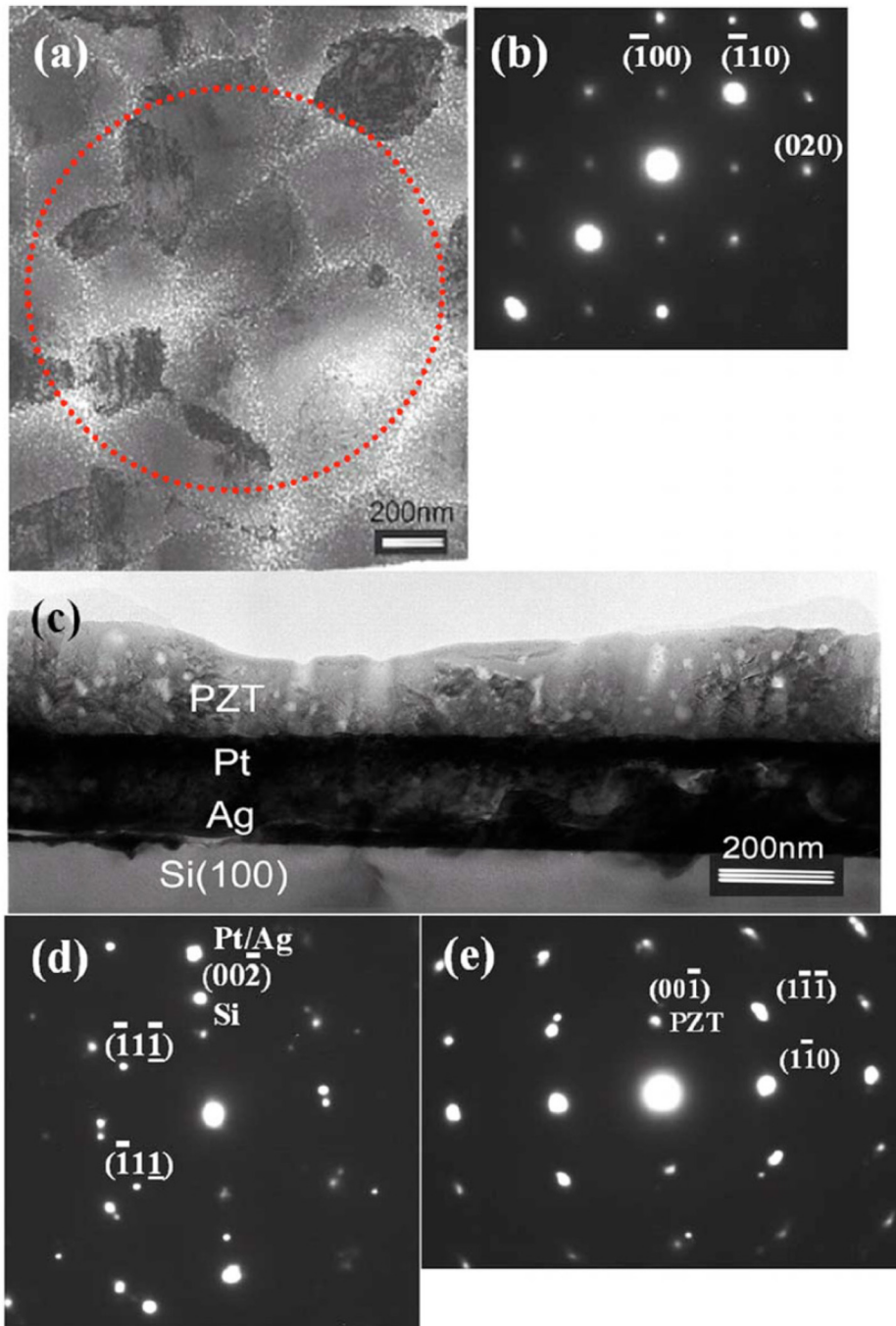


FIG. 6. (a) Plane-view TEM image of the sample PZT(53/47)/Pt/Ag/Si. The circle shows the grains in PZT film. (b) Selected area electron diffraction (SAED) pattern of the PZT(53/47) film along the [001] zone axis. (c) Cross-sectional TEM image of the PZT(20/80)/Pt/Ag/Si sample. (d) Selected area electron diffraction pattern of the Pt/Ag/Si structure along the Si[110] zone axis. (e) Selected area electron diffraction pattern of the PZT(20/80) layer along the PZT [110] zone axis. Reprinted with permission from Appl. Phys. Lett. **90**, 172903 (2007). Copyright 2007 AIP Publishing LLC.

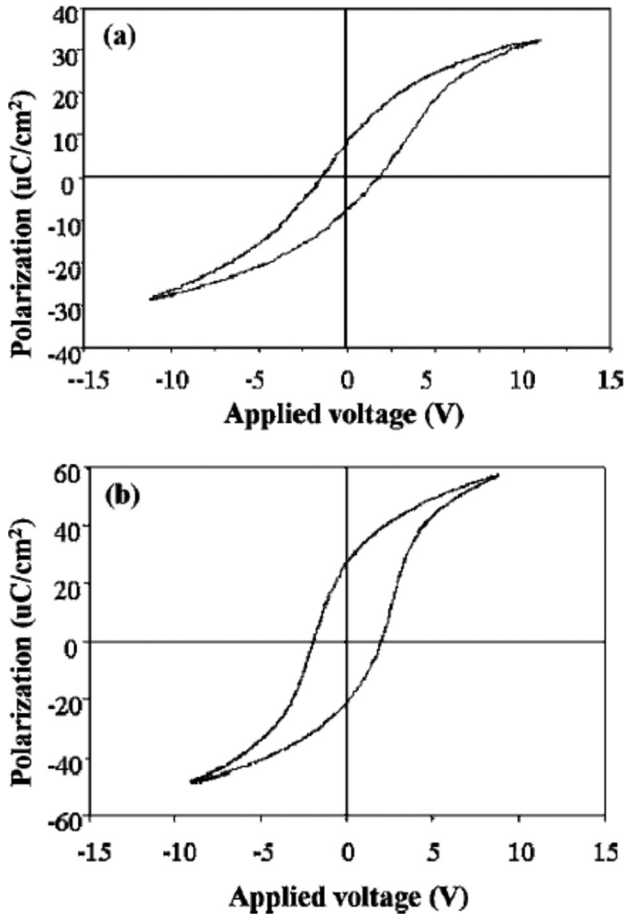


FIG. 7. P-E hysteresis loops of PZT capacitors using Pt top electrodes: (a) PZT(53/47) and (b) PZT(20/80). Reprinted with permission from Appl. Phys. Lett. **90**, 172903 (2007). Copyright 2007 AIP Publishing LLC.

Most interestingly, as shown in Fig. 9, no obvious fatigue was observed even after  $10^{10}$  switching cycles indicating the outstanding electrical endurance of the PZT films using LNO top electrodes. This should be compared with the PZT film with Pt top electrodes, which showed a significant polarization loss after  $10^8$  cycles.

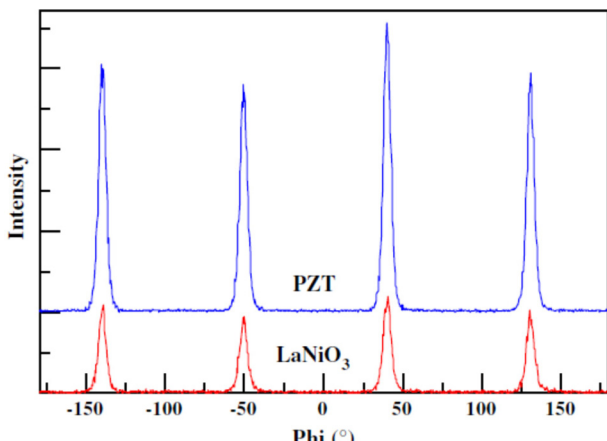


FIG. 8. XRD  $\phi$  scans of (110) planes of PZT and LaNiO<sub>3</sub> layers. Reprinted with permission from C. Wang and M. H. Kryder, J. Electron. Mater. **38**, 1921 (2009). Copyright 2009 Springer Publishing.

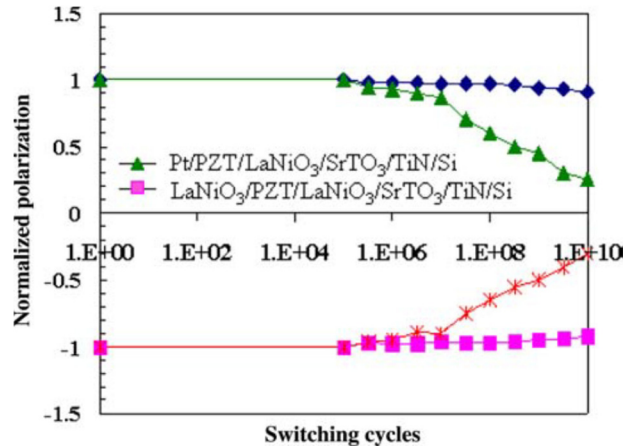


FIG. 9. Fatigue measurements of PZT/LaNiO<sub>3</sub>/SrTiO<sub>3</sub>/TiN/Si using Pt top electrodes and LaNiO<sub>3</sub> top electrodes. Reprinted with permission from C. Wang and M. H. Kryder, J. Electron. Mater. **38**, 1921 (2009). Copyright 2009 Springer Publishing.

## B. Multiferroelectrics (ferroelectric and ferromagnetic heterostructures)

The combination of ferroelectric and ferromagnetic compounds has been making headlines for the past decade,<sup>74–76</sup> motivated by the promise of non-volatile and low power spintronics applications. Similarly, there has been widespread<sup>77–79</sup> interest in utilizing FE/FM combinations to achieve electric-bias induced magnetic moment switching.

### 1. BiFeO<sub>3</sub>/La<sub>0.7</sub>Sr<sub>0.3</sub>MnO<sub>3</sub> (BFO/LSMO)

The coupling of the ferroelectric-antiferromagnetic fields in the BFO in combination with the ferromagnetic (external)-antiferromagnetic exchange interaction linking the BFO and adjacent ferromagnetic layers enables the transduction of an electrical voltage into an orientation change in the magnetic moment of the overlayer. Chu *et al.*<sup>77</sup> have demonstrated electric field (E-field) control of the local ferromagnetism (FM) when BFO is in intimate contact with Co<sub>0.9</sub>Fe<sub>0.1</sub>, and Lebeugle *et al.*<sup>78</sup> have reported the demonstration of E-field switching of magnetic anisotropy in perm-alloy (Py) when it is in contact with BFO. Finally, Wu *et al.*<sup>79</sup> have reported on reversible E-field control of exchange bias (H<sub>EB</sub>) when BFO was deposited on LSMO.

A combination of TiN, MgO, and STO buffer layers was used to deposit multilayer oxide-heterostructures on Si (100).<sup>80,81</sup> TiN (4.240 Å) has an excellent lattice match with MgO (4.216 Å), which has a misfit of about 8% with STO (3.905 Å). STO on MgO/TiN/Si is particularly interesting since it was grown strain-free ( $c_{\text{film}} = 3.907$  Å and  $c_{\text{bulk}} = 3.905$  Å) through DME. STO matches very well with most of the relevant epitaxial oxides such as BFO, PZT, BTO, and LAO by providing not only a compatible perovskite structure but also a closer match of both lattice constant and thermal expansion coefficient (TEC). The samples investigated in detail include: BFO/LSMO/STO/MgO/TiN/Si(100), LSMO/STO/MgO/TiN/Si(100), and BFO/STO/MgO/TiN/Si(100).

Fig. 10(a) presents a  $\theta$ -2 $\theta$  XRD pattern of the 5-layer heterostructure of sample BFO/LSMO/STO/MgO/TiN/Si(100). No evidence of additional phases or interfacial reaction

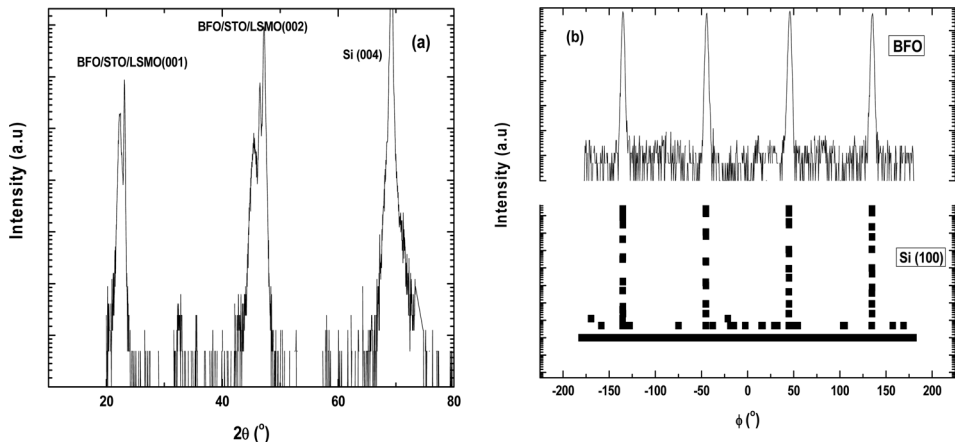


FIG. 10. (a) Typical  $\theta$ - $2\theta$  (out of plane) XRD pattern (in log axis) of sample BFO/LSMO/STO/MgO/TiN/Si(100) showing high quality, single phase and (00l) films of BFO. (b)  $\phi$ -scan patterns of BFO and Si of (111) reflection collected from sample A at  $2\theta = 39.46^\circ$ ,  $\omega = 19.73^\circ$ , and  $\chi = 55.00^\circ$  for BFO and  $2\theta = 28.46^\circ$ ,  $\omega = 14.23^\circ$ , and  $\chi = 54.74^\circ$  for Si (100). This pattern shows 4 peaks separated by  $\sim 90^\circ$  indicating its pseudo cubic/rhombohedral symmetry, establishing the cube-on-cube relationship with the underlying substrate Si (100). Reprinted with permission from Rao *et al.*, Nano Lett. **13**, 5814 (2013). Copyright 2013 American Chemical Society.

products was observed in the XRD pattern. It is evident from this pattern that all the layers grew with a preferential (00l) orientation (textured growth). The epitaxial growth and IP orientation of all the five layers were studied in detail by means of  $\varphi$ -scan x-ray diffraction, see Fig. 10(b). This pattern shows 4 peaks separated by  $\sim 90^\circ$  indicating its pseudo cubic symmetry and establishing the cube-on-cube relationship of the BFO with the underlying substrate Si (100). This stands in

contrast to BFO growth on MBE-grown STO buffered Si substrates. For example, in the work of Wang and co-authors,<sup>82</sup> the BFO film and STO buffer layer were rotated about  $45^\circ$  with respect to Si substrate resulting in a strain of 1.7% between STO and Si. This strain proved to be very difficult to relax leading to unwanted strain in the BFO. On the other hand, when STO layer was grown on MgO/TiN buffered Si using DME paradigm, STO thin films were grown strain-free

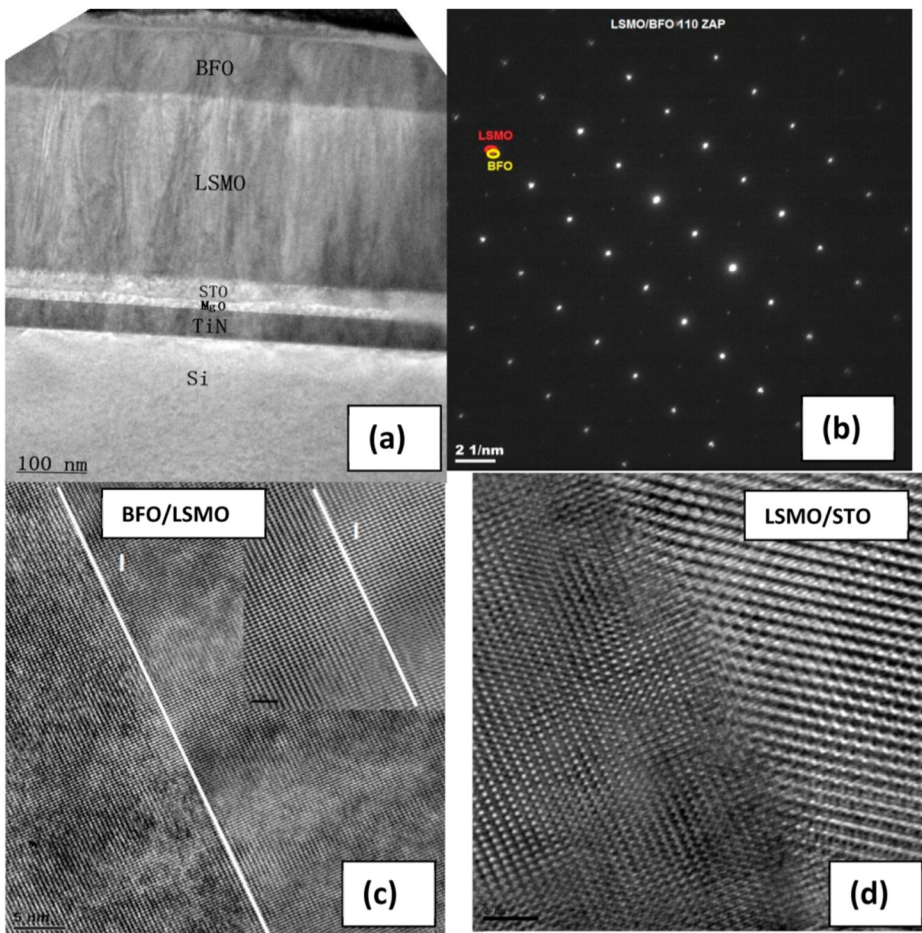


FIG. 11. (a) Bright field cross-section TEM image taken from sample e BFO/LSMO/STO/MgO/TiN/Si(100), where BFO ( $\sim 100$  nm) film was grown at  $650^\circ\text{C}$ . All 5-layers are marked. The top unmarked layer is of Pt sputtered during FIB sample preparation process. The scale bar is 100 nm. (b)  $(110)$  zone-axis pattern (ZAP) for BFO/LSMO interface. (c) HRTEM image of BFO (100 nm)/LSMO (250 nm) interface. The inset presents the magnified image, where "I" denotes interface. (d) HRTEM image of LSMO/STO interface. Reprinted with permission from Rao *et al.*, Nano Lett. **13**, 5814 (2013). Copyright 2013 American Chemical Society.

( $c_{\text{film}} = 3.907 \text{ \AA}$  and  $c_{\text{bulk}} = 3.905 \text{ \AA}$ ) with a cube-on-cube orientation, i.e., no rotation. As a result, the BFO layer was near strain free. From the  $2\theta$  XRD data for the (002) peak, the out-of-plane (OOP) lattice parameter of BFO was determined to be  $3.966 \text{ \AA}$ , close to the bulk lattice parameter of  $3.965 \text{ \AA}$ .<sup>77–79</sup> Figure 11(a) shows a typical bright-field cross-section TEM image of sample BFO/LSMO/STO/MgO/TiN/Si (100), in which all the layers are labeled. The thicknesses of BFO and LSMO were estimated to be  $\sim 100$  and  $250 \text{ nm}$ , respectively. The unmarked top layer was Pt, which was sputtered during the FIB-sample preparation process. The  $\langle 110 \rangle$  zone axis electron diffraction pattern of the BFO/LSMO interface is shown in Fig. 11(b). Due to the close match between the lattice constants of BFO and LSMO, their diffraction spots for low-index planes overlap with each other. However, the splitting of diffraction points for higher-index planes could be discerned. For example, the diffraction points corresponding to BFO (2 – 2 6) and LSMO (2 – 2 6) planes are distinguishable and labeled in Fig. 7(b). The alignment of two sets of diffraction spots proves the cube-on-cube epitaxial relationship between the top two layers. Figures 11(c) and 11(d) show typical HRTEM images taken at the BFO/LSMO and LSOM/STO interfaces, respectively. The inset of Fig. 11(c) shows the magnified image across the interface (I) for better clarity.

The electrical and ferroelectric properties of the BFO layer were measured using LSMO as the bottom electrode and Pt as the top electrode.<sup>81</sup> As presented in Fig. 12, I-V curves shift upward with increasing temperature (particularly, the curve recorded at 350 K) and exhibit non-leaky behavior up to at least 50 cycles (not shown). The curves are asymmetric as a consequence of the different work functions of Pt and LSMO electrodes and exhibit rectifying behavior. It was noticed that the temperature dependence did not follow the expected straight line behavior that is characteristic of space charge limited conduction (SCLC) which occurs when free charge carriers are injected into the dielectric sample under relatively

large electric fields. However, they did generally fit the linear behavior predicted for either Schottky barrier formation at the material electrode interface or Poole-Frenkel leakage mechanisms. More interestingly, bipolar resistive switching (RS) (toggling between opposite polarity states under the application of an alternating electrical bias) of BFO is revealed by the strong I-V hysteresis under positive and negative biases, which is prominent at low temperatures (200 K) and disappears at 350 K. This resistive switching was attributed to the ferroelectric switching of BFO that occurs around 5 V, although possible effects associated with oxygen vacancy migration under an applied electric field cannot be ruled out.

The ferroelectric local switching behavior of these films measured by switching spectroscopy based on piezo force microscopy (PFM) is shown in Fig. 13. The applied dc sweep voltage was a triangular pattern increasing from 0 to +6 V then down to -6 V and finally back to 0 V; the measurements were repeated 5 times to improve the signal to noise ratio. As illustrated in Fig. 13, characteristic butterfly loops were observed in OOP PFM amplitude (in black) signals of all the BFO films. In addition, the phase signal (in blue) indicated a clear switching behavior at a voltage of 4–5 V, providing clear evidence for the occurrence of ferroelectricity in the BFO films. The ferroelectric polarization remained constant over the measurement grid and over multiple cycles of the applied voltage. The ferroelectric polarization is found to lie along the film normal.

Isothermal (at 4 K) magnetic hysteresis (M-H) data were collected using superconducting quantum interface device (SQUID) magnetometer on all three samples under zero field cooled (ZFC) conditions. The M-H curves of samples BFO/LSMO/STO/MgO/TiN/Si(100) and LSMO/STO/MgO/TiN/Si(100) overlap. In comparison, the isothermal M-H curve for BFO/STO/MgO/TiN/Si(100) (where no LSMO layer is present) exhibits typical characteristic features of an antiferromagnetic phase and is consistent with the expectations for BFO deposited on a diamagnetic buffered substrate STO/

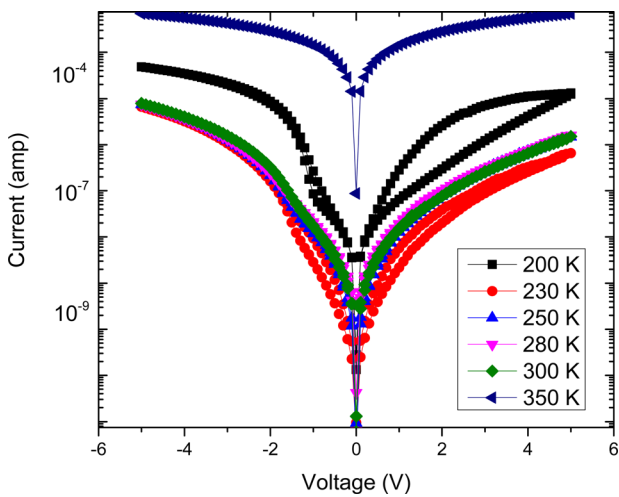


FIG. 12. Rectifying and hysteretic I-V curves of Pt/BFO/LSMO/STO/MgO/TiN/Si (100) measured as a function of temperature (200–350 K). The bias voltage was swept from 0 V → 5 V → 0 V → -5 V → 0 V. Note that the strong hysteresis in I-V curves confirms the resistive switching characteristics of BFO. Reprinted with permission from J. Appl. Phys. 117, 17D908 (2015). Copyright 2015 AIP Publishing LLC.

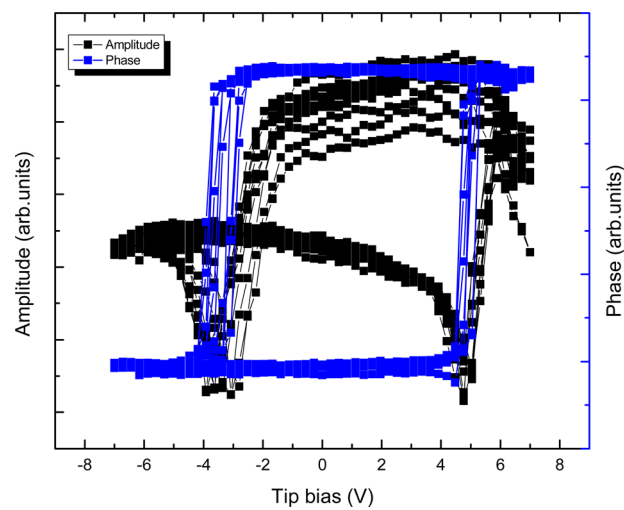


FIG. 13. Switching behavior of BFO/LSMO/STO/MgO/TiN/Si (100) revealed through SS-PFM: amplitude (black) and phase (blue) signals as a function of tip bias. The switching voltage is about 4–5 V. Reprinted with permission from J. Appl. Phys. 117, 17D908 (2015). Copyright 2015 AIP Publishing LLC.

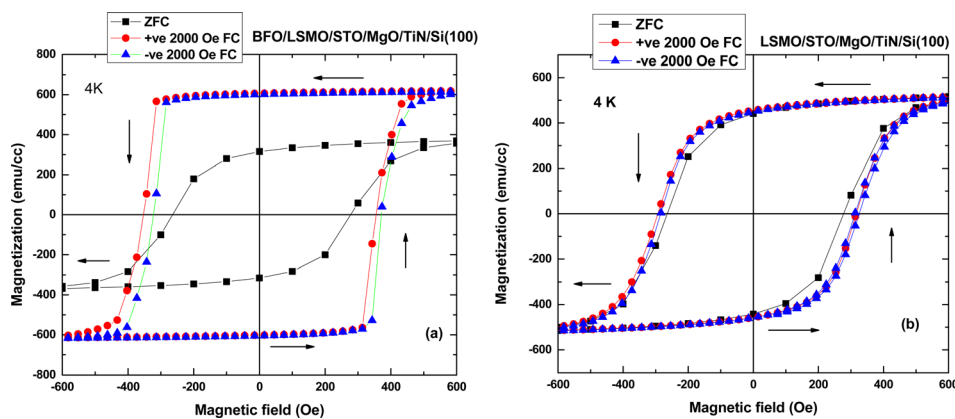


FIG. 14. (a) Comparison of isothermal (4 K) M-H curves measured on sample BFO/LSMO/STO/MgO/TiN/Si(100) under ZFC and after cooling the sample under +2000 Oe and -2000 Oe magnetic fields. The magnetic moment in FC case is much greater than that of the ZFC sample. Also, there is a shift in FC-MH loop. (b) Comparison of isothermal M-H curves measured on sample LSMO/STO/MgO/TiN/Si(100) under ZFC and after cooling the sample under magnetic fields of +2000 Oe and -2000 Oe. Both experiments were conducted under the same conditions as mentioned above. As can be immediately seen, the magnetic moment of latter sample remains practically the same, suggesting the existence of a strong interface contribution for BFO deposited on LSMO. No significant FC-MH loop shift and no change in magnetic moment are observed in latter sample. The arrows indicate the direction of magnetic field excursion. Reprinted with permission from Rao *et al.*, Nano Lett. **13**, 5814 (2013). Copyright 2013 American Chemical Society.

MgO/TiN/Si(100). However, under field cooling, it can be seen in Fig. 14 that the combination of multiferroic BFO and LSMO (sample in which both BFO and LSMO layers are present) experiences a large enhancement in magnetic moment and magnetic hysteresis squareness. This was interpreted to be indicative of the formation of a “ferromagnetic layer” in the BFO sublattice at the interface, as previously reported<sup>83</sup> for similar composite films. ZFC isothermal (4 K) M-H measurements did not reveal the presence of an interfacial magnetic moment. Only when the BFO/LSMO sample was cooled in the presence of a magnetic field did we observe evidence for the development of an interfacial magnetic moment. Interestingly, it was found that the polarity of magnetic field cooling had an effect on the interfacial magnetic moment.

To fully investigate this phenomenon, BFO/LSMO/STO/MgO/TiN/Si(100) and LSMO/STO/MgO/TiN/Si(100) heterostructures were cooled down to the measurement temperature under a magnetic field of +2 kOe and -2 kOe. M vs H data were then collected at several temperatures of

4, 25, 50, 100, 150, 200, 250, and 300 K as they were warmed up to  $\sim$ 370 K (at the end of each run), the onset of the paramagnetic (PM) phase in LSMO. The excursion to temperatures above  $T_C$  at the end of each M-H measurement was executed to exclude any extrinsic memory effects due to magnetic field- and temperature-excursions. The effects of positive and negative field cooling on magnetic moment, coercive field ( $H_C$ ), and exchange bias ( $H_{EB}$ ) (field produced in a ferromagnetic film that is coupled to an antiferromagnetic layer) for both samples are presented in Figs. 14(a) and 14(b), respectively. As it can be immediately observed in the field cooled (FC) experiments, the magnetic moment is much greater and the magnetic hysteresis loop is much squarer than that of the ZFC measurement. In addition, there is a clear (though small) horizontal shift (causing  $H_{EB}$ ) in the FC M-H loop. These differences are not observed for sample with no BFO layer present, as shown in Fig. 14(b). In fact, the magnetic moment of this sample remained nearly identical under all three experimental protocols.

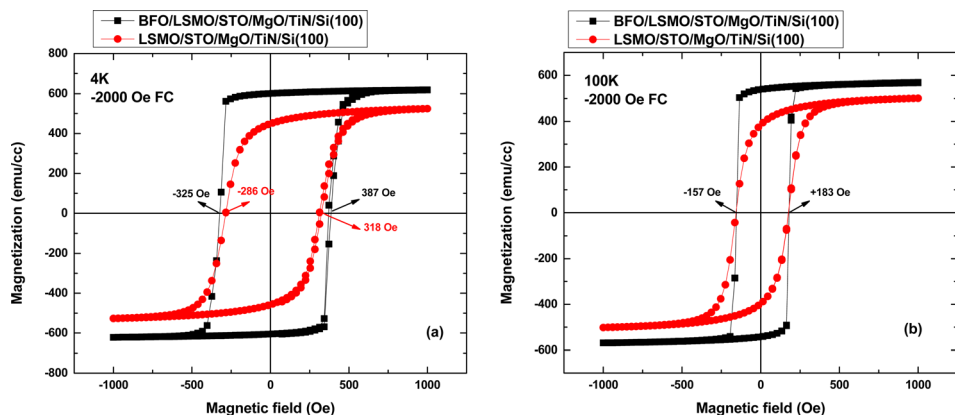


FIG. 15. Comparison of negative (-ve) FC (2000 Oe) isothermal (4 K) M-H curves collected on BFO/LSMO/STO/MgO/TiN/Si(100) and LSMO/STO/MgO/TiN/Si(100) at (a) 4 K and (b) 100 K. As we can notice immediately, there is a large enhancement in magnetic moment and exchange bias ( $H_{EB}$ ) of the former sample when compared with the latter. As shown in Fig. 5(b), the curves merge when the data are measured at a temperature of 100 K. The increase in saturation magnetization for sample BFO/LSMO/STO/MgO/TiN/Si(100) (with BFO) compared with sample LSMO/STO/MgO/TiN/Si(100) (without BFO) is  $\sim$ 17% (at 4 K) and 13% (at 100 K). Reprinted with permission from Rao *et al.*, Nano Lett. **13**, 5814 (2013). Copyright 2013 American Chemical Society.

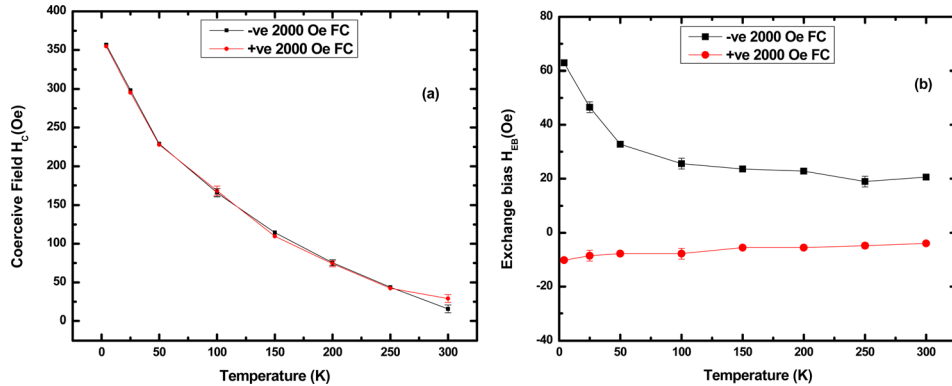


FIG. 16. The temperature dependences of (a)  $H_c$  and (b)  $H_{EB}$  obtained when the sample BFO/LSMO/STO/MgO/TiN/Si(100) was positive (in red) and negative (in black) field cooled under 2000 Oe from 370 K (PM phase). Lines guide the eye. The temperature dependences of  $H_c$  are the same in both the cases, i.e., decreases with the increase in temperature. Interestingly, the temperature dependence of  $H_{EB}$  is much stronger in negative field cooled case when compared with the positive field cooling. The error bars are estimated from the multiple measurements. Reprinted with permission from Rao *et al.*, Nano Lett. **13**, 5814 (2013). Copyright 2013 American Chemical Society.

Next, the effect of negative field cooling between samples BFO/LSMO/STO/MgO/TiN/Si(100) and LSMO/STO/MgO/TiN/Si(100) recorded at two distinct temperatures 4 K and 100 K is shown in Fig. 15, below and above the blocking temperature ( $T_b$ ), respectively.  $T_b$  is the temperature at which the time that it takes for the material's magnetization to randomly flip as a result of thermal fluctuations is equal to or greater than the measurement time. Figures 15(a) and 15(b) compare the negative FC (2000 Oe) M-H data collected from BFO/LSMO/STO/MgO/TiN/Si(100) (in black) and LSMO/STO/MgO/TiN/Si(100) (in red). As it can be noticed immediately, there is a large enhancement in magnetic moment and  $H_{EB}$  for the former BFO containing sample in comparison with the latter. As shown in Fig. 15(b), the curves for positive and negative field-cooled samples merge below 53 K, the blocking temperature. In addition, the squareness of magnetic hysteresis loop measured both above and below  $T_b$  increased when the LSMO layer is in intimate contact with the BFO layer. A similar behavior

was noticed when both samples were cooled in +2000 Oe (not shown). As displayed in Fig. 16(a), the temperature dependences of coercive fields under the both field cooled directions overlap. Interestingly, as shown in Fig. 16(b), when the former sample (in which both BFO and LSMO layers are present) is negatively field cooled, a stronger temperature dependence on  $H_{EB}$  was observed and diverges markedly as the sample is cooled below  $T_b$ . It was believed that such an enhancement in magnetic moment and magnetic coupling is likely related to an electronic orbital reconstruction at the interface and complex interplay between orbital and spin degrees of freedom, similar to what has previously been reported in the literature.<sup>83</sup>

## 2. BTO/LSMO

BTO is the prototypical lead-free ferroelectric perovskite, most studied<sup>84–89</sup> perovskite-type ferroelectric because of its important electrical and optical properties. In BTO, the

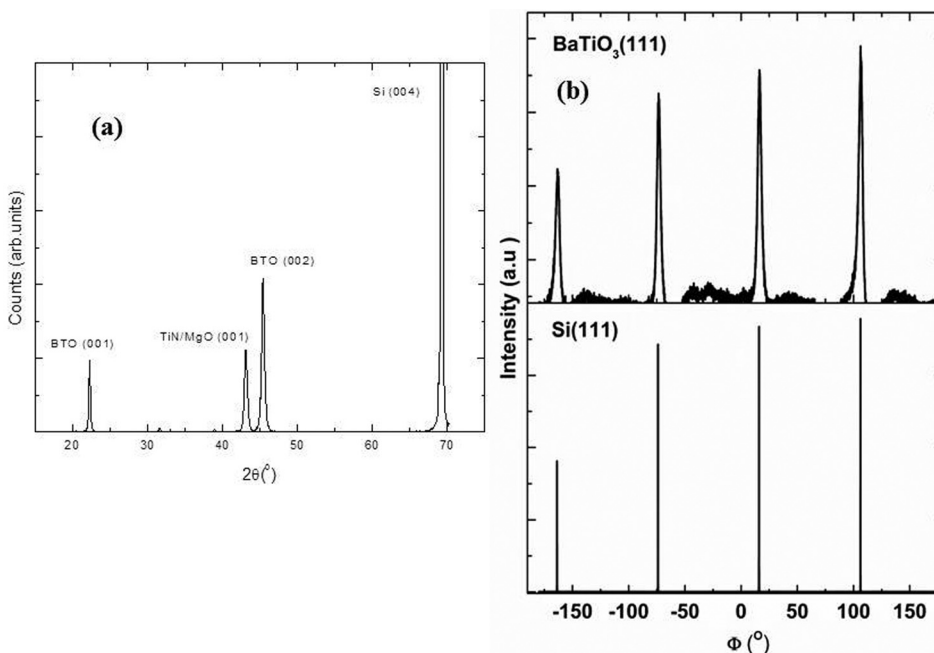


FIG. 17. (a) Typical  $\theta$ - $2\theta$  (out of plane) XRD pattern of BTO sample showing high quality, single phase and (00l) films of BTO. (b)  $\varphi$ -scan patterns of BTO and Si of (111) reflection collected from sample A at  $2\theta = 39.46^\circ$ ,  $\omega = 19.73^\circ$ , and  $\chi = 55.00^\circ$  for BFO and  $2\theta = 28.46^\circ$ ,  $\omega = 14.23^\circ$ , and  $\chi = 54.74^\circ$  for Si (100). This pattern shows 4 peaks separated by  $\sim 90^\circ$  indicating its pseudo cubic/rhombohedral symmetry, establishing the cube-on-cube relationship with the underlying substrate Si (100). Reprinted with permission from J. Appl. Phys. **116**, 094103 (2014). Copyright 2014 AIP Publishing LLC.

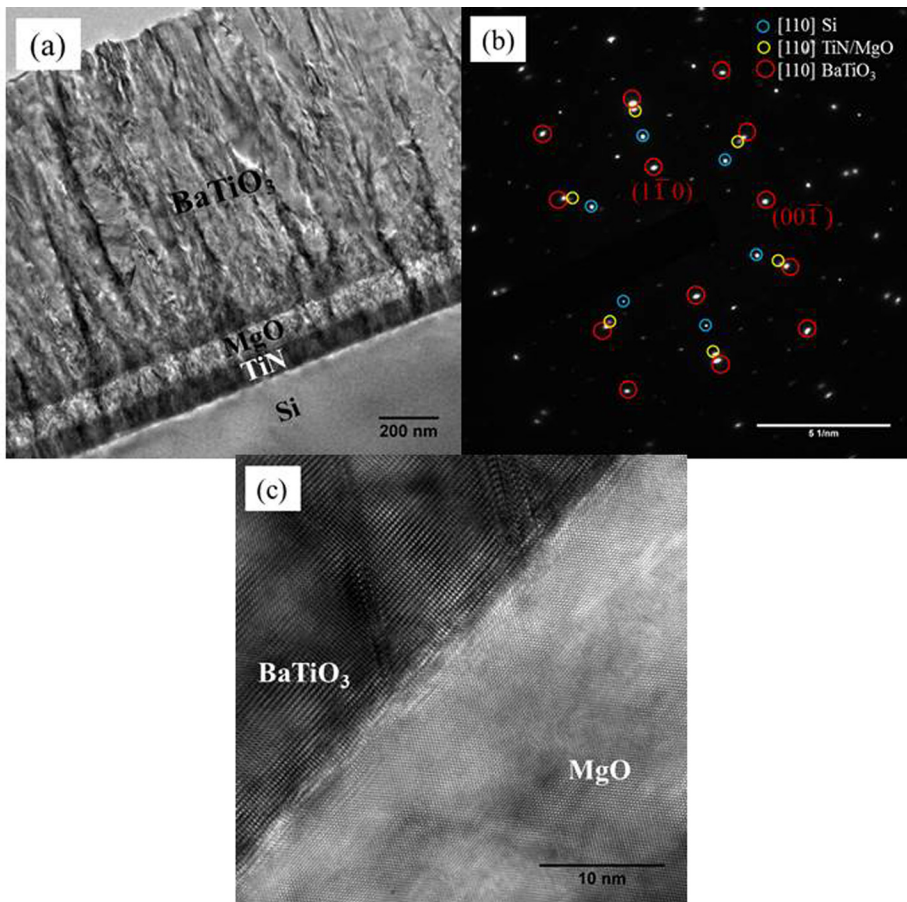


FIG. 18. (a) Bright field cross-section TEM image taken from BTO sample, where BTO ( $\sim 1050$  nm) film was grown at  $700^{\circ}\text{C}$ . All 3-layers are marked. The scale bar is 200 nm. (b)  $\langle 110 \rangle$  zone-axis pattern (ZAP) for BTO/MgO interface. (c) HRTEM image of BTO (1050 nm)/MgO (95 nm) interface. Reprinted with permission from J. Appl. Phys. **116**, 094103 (2014). Copyright 2014 AIP Publishing LLC.

TiO<sub>6</sub> octahedra are linked in a regular cubic array forming a high-symmetry  $Pm\bar{3}m$  phase in the paraelectric state. Below the Curie temperature  $T_C \sim 110^{\circ}\text{C}$ , a spontaneous polarization arises due to the noncentrosymmetric displacement of Ti<sup>+4</sup> and O<sup>-2</sup> ions relative to Ba<sup>+2</sup> ions ( $P4mm$ ) leading to the ferroelectric state. It was demonstrated<sup>90–92</sup> that the ferroelectric BTO thin films can be epitaxially deposited onto a silicon platform using the MgO/TiN buffer layers.<sup>4–8</sup> In order to establish structure-property correlations, the BTO/SRO/MgO/TiN/Si (100) heterostructures were characterized using high temperature XRD, cross sectional TEM, Raman spectroscopy, and polarization hysteresis measurements. Fig. 17(a) presents a  $\theta$ - $2\theta$  XRD pattern of the BTO/MgO/TiN/Si (100) heterostructure at room temperature. No evidence of additional phases or interfacial reaction products was observed in the XRD pattern. It was evident from this pattern that all the layers showed preferential (00l) orientation. From the  $2\theta$  XRD data for the (002) peak, the OOP lattice parameter of BTO was determined to be 3.996 Å, comparable to the bulk value of 4.005 Å,<sup>84–89</sup> suggesting near complete relaxation of the film. The epitaxial growth and the IP orientation of all three layers were studied in detail by means of  $\varphi$ -scan XRD of (111) reflection for BTO and Si. This pattern, see Fig. 17(b), shows 4 peaks separated by  $\sim 90^{\circ}$  indicating its cubic symmetry and establishing the cube-on-cube relationship of the BTO with the underlying substrate Si (100).

Figure 18(a) is a typical bright-field cross-section TEM micrograph of the sample, in which the BTO/MgO/TiN/Si

(100) layers are labeled. The thicknesses of BTO, MgO, and TiN are determined as  $\sim 1050$ , 95, and 85 nm, respectively. The  $\langle 110 \rangle$  zone axis electron diffraction pattern of the BTO/MgO/TiN/Si region is shown in Fig. 18(b). Due to the close lattice match between MgO and TiN, the low order diffraction spots in Fig. 18(b) are indistinguishable. The alignment of the two sets of diffraction spots confirms the cube-on-cube epitaxial relationship between the layers. Figure 18(c) presents typical HREM images taken at the BTO/MgO interface, showing the presence of misfit dislocations concentrated at the interface.

Polarization hysteresis measurements were made on 250- $\mu\text{m}$ -diameter capacitors of relaxed BTO thin films sandwiched between a Pt top electrode and a SRO conducting perovskite oxide bottom electrode. Figure 19 shows the representative ferroelectric hysteresis loops from these BTO devices. These measurements have been reproduced on several devices fabricated on two identical Si (100) substrates as a function of frequency (2–20 kHz) and voltage (ranging from  $-10$  to  $+10$  V). The polarization reversal exhibits a clear memory effect that is approaching saturation. A coercive voltage ( $V_c$ ) of  $\sim 0.9$  V is measured on the negative voltage axis, which is significantly lower than the values of 5–10 V reported for 40 nm-thick BTO thin films deposited on Si (100) by other groups.<sup>93</sup> Also, the observed remanent polarization ( $4\text{--}5 \mu\text{C}/\mu\text{cm}^2$ ) is in good agreement with the values ( $1\text{--}8 \mu\text{C}/\mu\text{cm}^2$ ) previously reported<sup>94,95</sup> for BTO thin films but well below the value of  $24 \mu\text{C}/\mu\text{cm}^2$  reported for

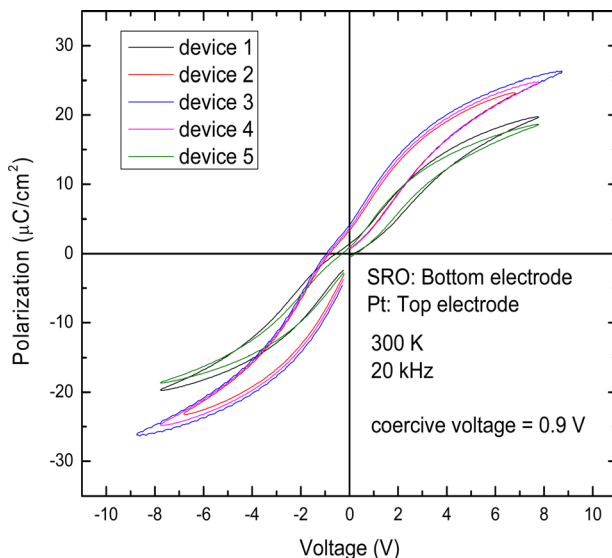


FIG. 19. P-V hysteresis measurements collected for several BTO devices. Reprinted with permission from J. Appl. Phys. **116**, 094103 (2014). Copyright 2014 AIP Publishing LLC.

BTO single crystals.<sup>96</sup> This could be due to substrate clamping, microscopic structural variations, and oxygen off stoichiometry.<sup>97</sup> As can be seen, the hysteresis loops are shifted in the negative voltage direction. This imprint (offset along the voltage axis) effect is probably due to the asymmetric interfacial properties introduced by having different top and bottom electrodes in contact with the BTO films. The observed pinching of ferroelectric loops near the origin may be due to a distribution of switchable dipolar defects in the film.<sup>98</sup> The ferroelectric loops were measured for about 50 cycles with no observed degradation of the polarization characteristics. The BTO films are under tensile strain because of the lower thermal expansion coefficient (TEC) of the Si substrate compared with the BTO. Hence, these films have more rounded and slanted hysteresis characteristics.<sup>39</sup> The piezoelectric response is influenced by the mechanical boundary conditions, in particular, by clamping associated with the thick substrate.

To study the influence of the ferroelectric layer on the magnetic properties of magnetic layer, a multiferroic bilayer (BL) of BTO-LSMO layers was epitaxially grown on a silicon substrate using MgO/TiN buffer layers.<sup>91</sup> It was found that both BTO and LSMO layers grew epitaxially as cube-on-cube with Si (100). Here, we compare two samples, in which the thicknesses of BTO layer were 100 and 50 nm, and the thickness of LSMO layer was kept constant at 217 nm. For comparison, the magnetization data of the sample without BTO are also included. No post growth oxygen annealing (OA) was performed on any of the structures discussed here. All the magnetization measurements were preformed parallel to the plane of the film. The temperature dependence of the IP magnetization, ( $M$  vs  $T$ ), was measured in small magnetic fields of 20 and 100 Oe after cooling the samples from  $T = 400$  K to  $T = 4$  K under zero magnetic field. The M(T) curves measured both at 20 and 100 Oe show similar behavior. Figure 20 presents the data measured in a 100 Oe magnetic field. The results showed a clear saturation at low temperature, though

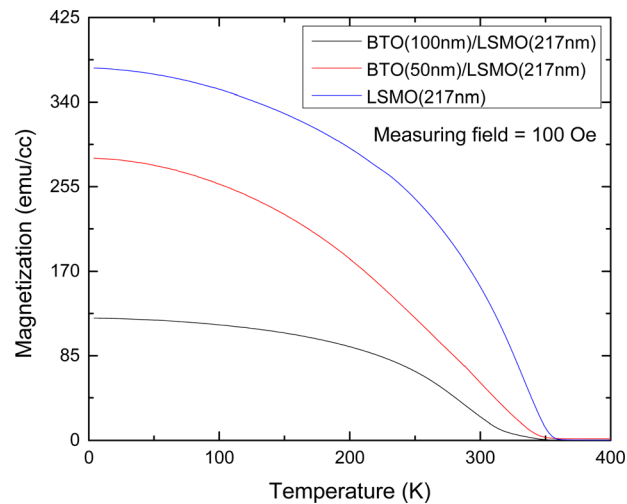


FIG. 20. Magnetization vs. temperature ( $M$ - $T$ ) curves of samples with BTO layer thickness of 100 nm (in black), BTO layer thickness of 50 nm (in red), and without BTO layer (in blue) for all the structures. The data were collected during the cooling cycle with the measuring field of 100 Oe. As it can be noticed, the  $T_C$  of all the samples is found to be the same at  $\sim 350$  K. The magnetic field is applied along  $\langle 100 \rangle$  direction of the sample. Reprinted with permission from J. Appl. Phys. **116**, 224104 (2014). Copyright 2014 AIP Publishing LLC.

with varying saturation magnetization (discussed later). The saturation magnetization ( $\sim 380$  emu/cc) of LSMO without BTO was in close agreement with the previously reported values (370–385 emu/cc).<sup>99</sup> There were two notable observations: (a) the ferromagnetic  $T_C$ , the temperature where the magnetization drops to zero, was found to be nearly independent of BTO layer thickness, consistent with the earlier reports,<sup>99</sup> and (b) surprisingly, large, sharp, and discontinuous jumps in the temperature dependent magnetization data associated with BTO structural transitions were absent in both samples, containing BTO. It is noted that such behavior was retained when the data were collected both during the heating and cooling cycles. Such an absence of low temperature structural phase transitions in epitaxial BTO thin films grown has been observed previously<sup>99</sup> and can be explained by the presence of mechanical clamping of the film to the substrate. These results are consistent with the findings of a recent spin wave resonance study<sup>100</sup> reported on LSMO (330 nm)/BTO (270 nm) epitaxial heterostructure deposited on LAO which concluded that the BTO layer itself induces IP surface pinning at the BTO/LSMO interface that modifies the IP bulk magnetic anisotropy of the LSMO film. Due to a strong IP pinning between BTO and LSMO induced by ferroelectric BTO layer, a strong reduction in saturation magnetization ( $M_S$ ) and an enhancement in  $H_c$  were observed and appeared to vary as a function of the stress state of the BTO. The stress state of the BTO layer was believed to directly influence the reordering of the atoms at the BTO-LSMO interface and thus affects the extent of magnetic pinning in the LSMO layer. To support the hypothesis and to prove that the ferroelectricity in BTO is causing the changes in LSMO magnetic properties, a thin ( $\sim 10$ –15 nm) insulating, non-magnetic, and non-ferroelectric STO layer was inserted between BTO and LSMO. The corresponding M-H and M-T curves closely replicated the magnetization,  $T_C$  and  $H_c$  characteristics of the lone LSMO layer,

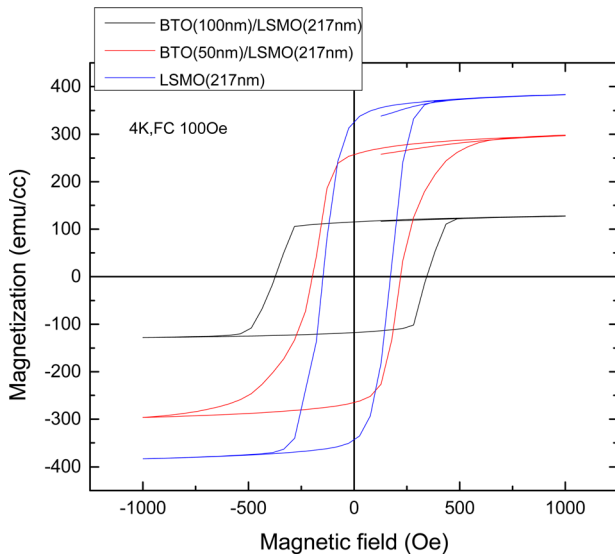


FIG. 21. Comparison of isothermal (4 K) M-H curves measured on all the samples cooled from 400 K under 100 Oe. As one can notice, sample with BTO layer thickness of 100 nm shows 2-times higher  $H_c$ , much improved squareness ( $M_s/M_r$ ), and 3-times lesser saturation magnetization ( $M_s$ ) in comparison with sample without BTO layer. All the experiments were conducted under the same conditions as mentioned above. The magnetic field is applied along  $\langle 100 \rangle$  direction of the sample. Reprinted with permission from J. Appl. Phys. **116**, 224104 (2014). Copyright 2014 AIP Publishing LLC.

thus confirming that it is the presence of the BTO in direct contact with the LSMO that is causing the changes in the magnetic properties of LSMO. This is believed to be caused by a chemical or ferroelectric polarization induced reordering at the interface.

In Fig. 21, isothermal M-H data are presented for three samples at 4 K, which had been cooled under a field of 100 Oe. Three interesting characteristics of M-H curves are noted: (i) the squareness (ratio of saturation to remnant magnetization) of M-H loop was improved with increasing BTO film thickness (varying from 0 to 100 nm), (ii) the  $H_c$

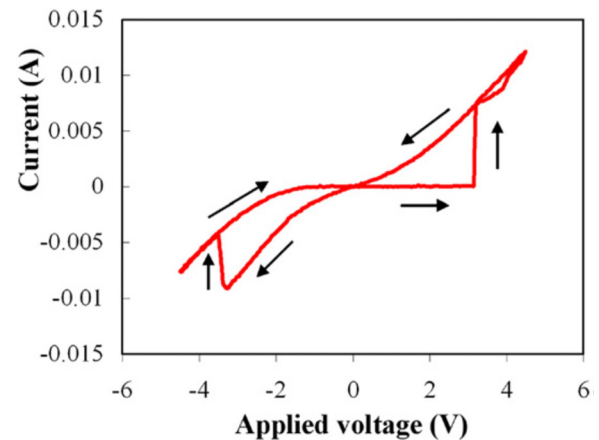


FIG. 22. Current–voltage characteristics of a 62 nm thick epitaxial  $\text{BaTiO}_3$  film on TiN/Si substrates. The top TiN electrode has a diameter of 250  $\mu\text{m}$ . Reprinted with permission from C. Wang and M. H. Kryder, J. Phys. D: Appl. Phys. **41**, 245301 (2008). Copyright 2008 IOP Publishing.

( $\sim 365$  Oe) of BTO/LSMO sample (100 nm thick BTO layer) is almost twice that of the sample ( $\sim 163$  Oe) with no BTO layer, and (iii) the saturation magnetization of BTO(100 nm)/LSMO was reduced to about 1/3 that of sample with no BTO layer. Similar results were observed when the measurements were performed under higher cooling fields (up to  $\pm 2000$  Oe) for temperatures below the  $T_C$  of ( $\sim 350$  K) LSMO. The observed trend is found to be independent of the polarity of the field cooling.

In related experiments, epitaxial BTO thin films were deposited onto TiN-buffered  $\text{Si}(0\ 0\ 1)$  single crystal substrates using rf sputtering by Wang and Kryder.<sup>101</sup> The deposited BTO films showed a very smooth surface with a roughness of 0.75 nm. Again, the orientation relationship was determined to be  $\text{BTO}(0\ 0\ 1)[1\ 1\ 0] \parallel \text{TiN}(0\ 0\ 1)[1\ 1\ 0] \parallel \text{Si}(0\ 0\ 1)[1\ 1\ 0]$ , which was explained using the DME model. The microstructure and the interface of the heterostructure were studied using

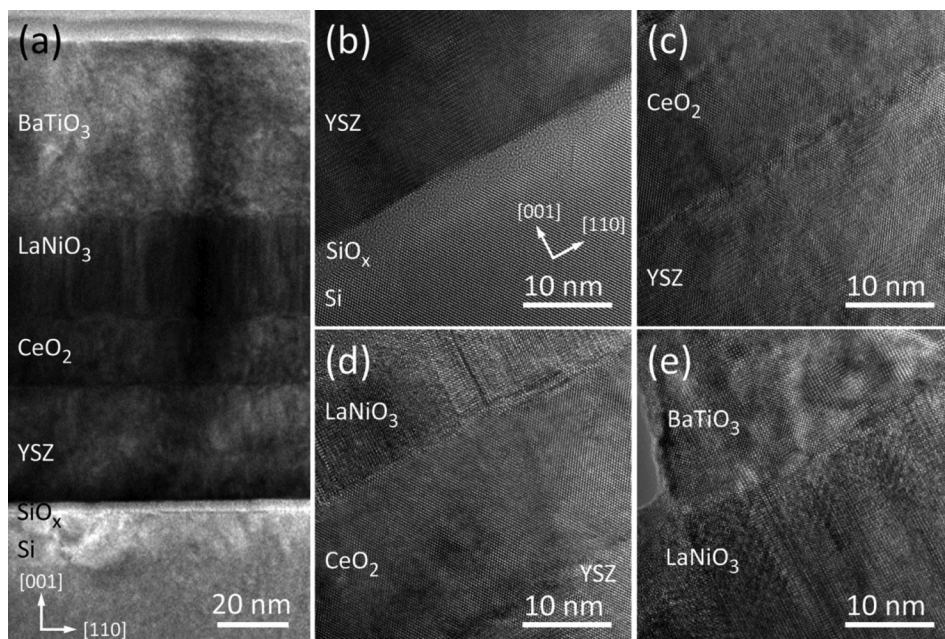
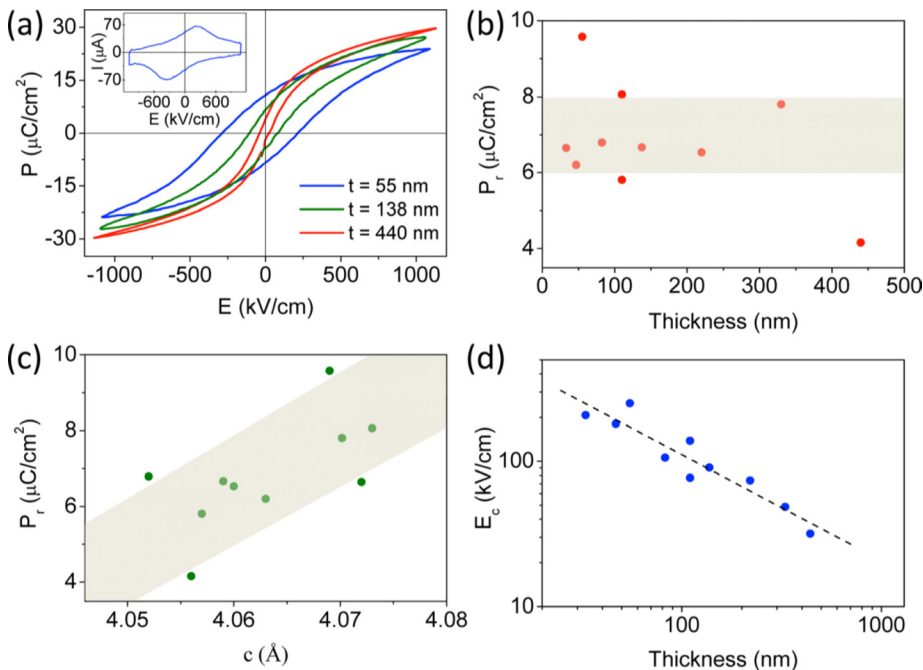


FIG. 23. TEM cross-section characterization of a sample with  $t$  (BTO)  $\sim 50$  nm: (a) low resolution image showing the whole multilayer. High-resolution images around YSZ/Si (note the presence of the  $\text{SiO}_x$  interfacial layer) (b),  $\text{CeO}_2/\text{YSZ}$  (c), LNO/ $\text{CeO}_2$ /YSZ (d), and BTO/LNO (e) interfaces. Reprinted with permission from Appl. Phys. Lett. **102**, 112905 (2013). Copyright 2013 AIP Publishing LLC.

HRTEM. The electron diffraction pattern confirmed the epitaxial relationship between each layer. The current–voltage ( $I$ – $V$ ) characteristics of the TiN/BTO/TiN/Si sample are presented in Fig. 22 and show clear resistive switching. The ratio of the high resistance state to the low resistance state is 150 with an input switching voltage of  $\pm 4.5$  V.

Similarly, Scigaj and co-authors have reported on the epitaxial integration of ultra-flat epitaxial BTO thin films onto Si (001) substrates using LaNiO<sub>3</sub> (LNO)/CeO<sub>2</sub>/YSZ buffer layers.<sup>102</sup> YSZ and CeO<sub>2</sub> layers grew cube on-cube on Si, while LNO and BTO are rotated in-plane by 45°, as expected from lattice matching considerations. The CeO<sub>2</sub> and LNO layers provided for the gradual accommodation of the large lattice mismatch (~9%) between BTO and YSZ. The low magnification bright field cross-section TEM image for the entire heterostructure is shown in Fig. 23(a). All interfaces can be clearly resolved in the HREM images presented in Figs. 23(b)–23(e). The YSZ/Si interface (see Fig. 23(b)) shows an interfacial SiO<sub>x</sub> layer with thickness of 3 nm.

Polarization measurements<sup>102</sup> indicated that the BTO was ferroelectric with a large out-of-plane polarization. The corresponding polarization hysteresis loop is shown in Fig. 24(a) (main panel). The saturation polarization  $P_s$  and remnant polarization  $P_r$  were 20  $\mu\text{C}/\text{cm}^2$  and 10  $\mu\text{C}/\text{cm}^2$ , respectively. Polarization loops of two thicker films ( $t = 138$  and 440 nm) are also plotted in Fig. 24(a). The corresponding remnant polarization  $P_r$  was around 7 and 4  $\mu\text{C}/\text{cm}^2$ , respectively. All fabricated BTO films (thickness in the 33–440 nm range) had  $P_r$  values between 4 and 10  $\mu\text{C}/\text{cm}^2$ , with no clear thickness dependence (Fig. 24(b)). It was observed that  $P_r$  scaled with the  $c$  parameter (Fig. 24(c)). Figure 24(a) also shows a notable variation in the coercive field ( $E_c$ ) between the films.  $E_c$  decreases from above 250 to less than 35 kV/cm as the thickness  $t$  increases and shows power law dependence with thickness (see Fig. 24(d)).



### 3. $\text{Cr}_2\text{O}_3$

Bulk single crystal Cr<sub>2</sub>O<sub>3</sub> (corundum structure) is an antiferromagnetic insulator below its Neel temperature ( $T_N$ ) of 307 K and is the first RT magnetoelectric (ME) material ever reported.<sup>103–106</sup> The high insulating nature of Cr<sub>2</sub>O<sub>3</sub> makes it a suitable candidate to be employed as a tunnel barrier in magnetic tunnel junctions (MTJs). Room temperature ferromagnetism (RTFM) and ferroelectricity have been observed<sup>107</sup> in bulk Cr<sub>2</sub>O<sub>3</sub> single crystal. There are many reports<sup>108–110</sup> in the literature on the thin film deposition of Cr<sub>2</sub>O<sub>3</sub>, but most of them are related to the use of sapphire as a substrate because of the similarity in the crystal structure. A handful of attempts have been made at depositing Cr<sub>2</sub>O<sub>3</sub> films onto Si (111) substrates,<sup>111–113</sup> but to our knowledge no prior work on Si(100) substrates has been attempted until recently when epitaxial Cr<sub>2</sub>O<sub>3</sub> thin films were successfully deposited on Si (001) using epitaxial c-YSZ buffer layer by PLD.<sup>114</sup> The X-ray diffraction ( $2\theta$  and  $\varphi$ ) and TEM characterizations confirm that the films were grown epitaxially. An epitaxial relation between the layers is given as [001]Si || [001]YSZ || [0001]Cr<sub>2</sub>O<sub>3</sub> and [100]Si || [100]YSZ || [10–10] Cr<sub>2</sub>O<sub>3</sub> or [11–20] Cr<sub>2</sub>O<sub>3</sub>. The epitaxial nature of Cr<sub>2</sub>O<sub>3</sub> is evident from the 12 equi-spaced sharp peaks appearing in the  $\varphi$ -scan. The presence of 12 peaks, instead of three corresponding to 3-fold symmetry of the C-axis, indicates that there are four different IP domain variants associated with a single OOP orientation. This is expected due to the growth of 3-fold symmetric Cr<sub>2</sub>O<sub>3</sub> (0001) on 4-fold symmetric YSZ (002). The low magnification bright field cross sectional TEM image for Cr<sub>2</sub>O<sub>3</sub>/YSZ/Si heterostructure is shown in Fig. 25(a), and the HRTEM image is shown in Fig. 25(b). To further confirm the epitaxial relations, SADPs were acquired for the heterostructure. The [110] SADP acquired at the Si/YSZ interface is shown in the inset of Fig. 25(a), which is in agreement with the  $\varphi$ -scan data.

FIG. 24. (a) Polarization loops for BTO films with thicknesses  $t = 55$ , 138, and 440 nm. The current ( $I$ ) versus applied electric field ( $E$ ) curve corresponding to the  $t = 55$  nm film is in the inset. Remnant polarization plotted against thickness  $t$  (b) and  $c$ -parameter (c) of the films. (d) Coercive field plotted against BTO thickness in a log-log scale. The dashed line is a linear fit with slope  $-0.73(9)$ , compatible with  $E_c \cdot t^{-2/3}$  scaling. Reprinted with permission from Appl. Phys. Lett. 102, 112905 (2013). Copyright 2013 AIP Publishing LLC.

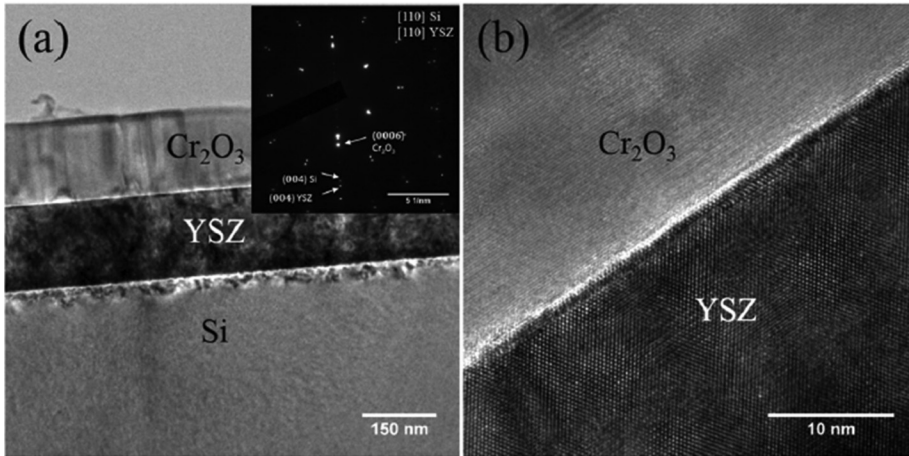


FIG. 25. (a) Low magnification cross sectional TEM image of  $\text{Cr}_2\text{O}_3$ /YSZ/Si(001) heterostructure. (b) HRTEM image of  $\text{Cr}_2\text{O}_3$ /YSZ interface. Inset of (a) shows the [110] zone axis SAED pattern acquired across the Si/YSZ interface. Reprinted with permission from Appl. Phys. Lett. **105**, 132401 (2014). Copyright 2014 AIP Publishing LLC.

Magnetic measurements were performed with an applied magnetic field parallel to the (0001) plane of  $\text{Cr}_2\text{O}_3$ . The data for a 40 nm thick  $\text{Cr}_2\text{O}_3$  sample are displayed in Fig. 26(a). It shows the isothermal M-H loops measured in the  $-10$  kOe to  $+10$  kOe field range at temperature ranging from 5 K to 400 K. The diamagnetic contribution from the substrate and the buffer layer has been subtracted. It can be seen that the loops exhibit saturation and finite  $H_c$  at all of the measured temperatures, indicating a typical ferromagnetic-like behavior up to 400 K. To identify whether the origin of FM in  $\text{Cr}_2\text{O}_3$  thin film is due to strain, films of various thicknesses ranging from 20 nm to 160 nm were grown. The IP M-H loops acquired at 5 K from the samples are plotted in Fig. 26(b). Enlarged plots are shown in the inset. All of the above samples show typical FM nature up to 400 K. It can be clearly seen that the  $M_S$  decreases with increasing thickness, indicating a strong effect of thickness on  $M_S$ . The thickness dependent  $M_S$  has been correlated with the strain present in the film

by taking high resolution XRD 2 $\theta$ -scans around the  $\text{Cr}_2\text{O}_3$  (006) reflections. The peak position shifts towards lower  $2\theta$  values with increasing film thickness, i.e., the OOP lattice parameter increases with increasing thickness, approaching the bulk value ( $13.594 \text{ \AA}$ ) for thicker films. The strain  $\varepsilon_{zz}$  present along this direction can be determined by the relation:  $\varepsilon_{zz} = (c_{\text{OOP}} - c_{\text{bulk}})/c_{\text{bulk}}$ , where  $c_{\text{bulk}}$  is the  $c$ -lattice constant for bulk  $\text{Cr}_2\text{O}_3$ . The variation of  $\varepsilon_{zz}$  and  $M_S$  with thickness is presented in Fig. 26(c). It is evident from this plot that  $M_S$  varies as a function of strain. The  $-ve$  sign for  $\varepsilon_{zz}$  indicates a compressive strain. Oxygen annealing studies revealed that FM in  $\text{Cr}_2\text{O}_3$  is also influenced by oxygen stoichiometry (see Fig. 26(d)).

### C. Magnetic layers

Motivated by the proposed racetrack memory patented by Parkin *et al.*,<sup>115</sup> a great deal of research activity has been

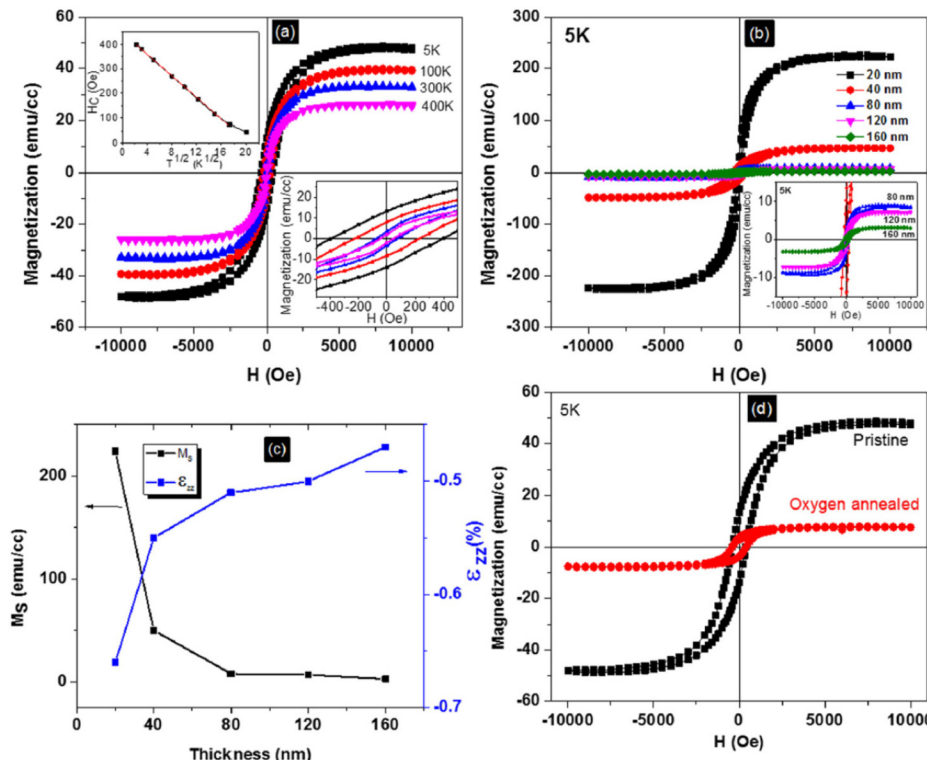


FIG. 26. (a) Isothermal field dependent magnetization plots of 40 nm thick  $\text{Cr}_2\text{O}_3$  film ranging from 5 K to 400 K. Lower inset: Enlarged view of the same in the  $-500$  Oe to  $+500$  Oe field range. Upper inset: Plot of  $H_C$  vs  $T^{1/2}$  showing linear fit in the range of 5 K to 300 K. (b) M-H loops acquired at 5 K for  $\text{Cr}_2\text{O}_3$  films with thickness ranging from 20 to 160 nm. Inset shows the enlarged version of the same. (c) Thickness dependent saturation magnetization  $M_S$  and out-of-plane strain  $\varepsilon_{zz}$  measured from XRD 2 $\theta$  scans. (d) M-H loops for 40 nm thick  $\text{Cr}_2\text{O}_3$  acquired at 5 K for pristine and oxygen annealed samples. For all the magnetic measurements, field was applied parallel to the (0001) surface of  $\text{Cr}_2\text{O}_3$ . Reprinted with permission from Appl. Phys. Lett. **105**, 132401 (2014). Copyright 2014 AIP Publishing LLC.

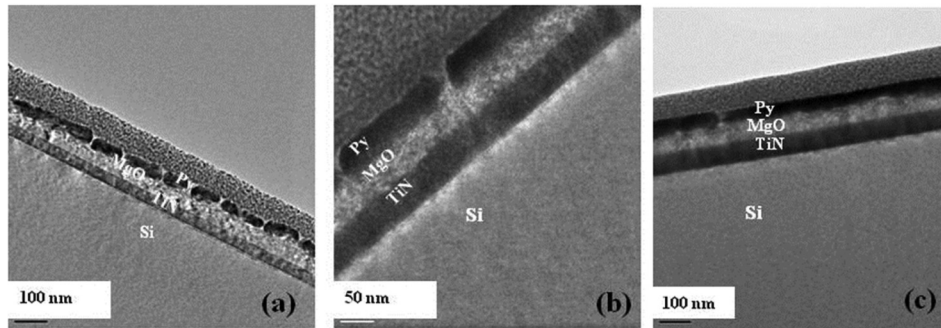


FIG. 27. Bright field cross-section TEM images collected from Py3 (a), Py6 (b), and Py12 (c). All the Py films were grown at 550 °C. All 3-layers TiN, MgO, and Py in each heterostructure are seen. The top layer is of Pt sputtered during FIB sample preparation process. The scale bar is 100 nm in (a) and (c); the scale bar is 50 nm in (b). The island structures in each Py layer are clearly visible. Reprinted with permission from Rao *et al.*, Curr. Opin. Solid State Mater. Sci. **18**, 140–146 (2014). Copyright 2014 Elsevier.

devoted to the deposition of permalloy (Py) magnetic nanostructures for high speed memory applications. Py usually refers to  $\text{Ni}_{1-x}\text{Fe}_x$  alloys that have a vanishingly small magnetocrystalline anisotropy and magnetostriction, but extremely large magnetic permeability. These unique properties make Py one of the most important soft magnets for a variety of applications, including as free layers in spin-valve magnetic-reading heads and in MTJs devices.<sup>116,117</sup> More recently, Py is being extensively used<sup>78,118</sup> to demonstrate E-field control of ferromagnetic moment in multiferroic heterostructure-based devices. Hence, exploring and understanding the magnetic properties of Py when interfaced with magnetic/non-magnetic oxide materials are of great importance.

To date, epitaxial Py layers have been deposited on MgO bulk substrates using MBE, e-beam evaporation, and magnetron sputtering deposition techniques. Related studies have also been reported on the Ni/MgO system. For instance, Raatz and Woltersdorf reported the effect of Ni film thickness on film orientation.<sup>119</sup> McCaffrey, Svedberg, Reniers, and Qiu *et al.* studied the effect of growth temperature on the orientation of epitaxial Ni films on MgO(001).<sup>120–123</sup> Lukaszew *et al.*<sup>124</sup> studied the magneto-optic Kerr effect (the magnetization-induced change in polarization state and/or intensity of the light reflected from the surface of a magnetized medium) of Ni thin films deposited on MgO single crystal substrates. Unfortunately, all of the above investigations, particularly, the magnetic properties of Ni thin films hitherto have been focused on films grown on bulk MgO substrates

using MBE and sputtering techniques. Furthermore, MgO bulk substrates are unsuitable from the viewpoint of practical applications in the magnetic recording industry because of its high single-crystal cost, limited wafer size, hygroscopic nature, and inferior mechanical properties. Subsection IV C 1 focuses on the effect of film thickness and morphology on the magnetic properties of epitaxial Py thin films grown on MgO thin-film buffer layers prepared on Si (100) substrates.

### 1. Permalloy (Py)

This section discusses recent developments<sup>125,126</sup> related to epitaxial Py integration onto Si (100) substrates. The Py films were grown on Si (100) using MgO/TiN buffer layers. From the OOP and IP XRD measurements, it was found that Py films had grown epitaxially. TEM bright field cross section images (see Fig. 27) indicated that the Py layer thicknesses gradually increased from 30 nm (3000 pulses) to 45 nm (6000–12 000 pulses), and island sizes increased from discretely separated islands roughly 60–90 nm in diameter to more densely packed films composed of irregularly shaped islands (recently coalesced islands) in the range of 150–600 nm (6000 pulses). These gradually develop into fairly equiaxed grains roughly 300–700 nm in diameter after longer deposition times (12 000 pulses).

The temperature-dependent (4–400 K) magnetization measurements for three samples labeled Py3, Py6, and Py12 (3000, 6000, and 12 000 pulses, respectively) are shown in Figs. 28(a)–28(c). The first measurement was taken after

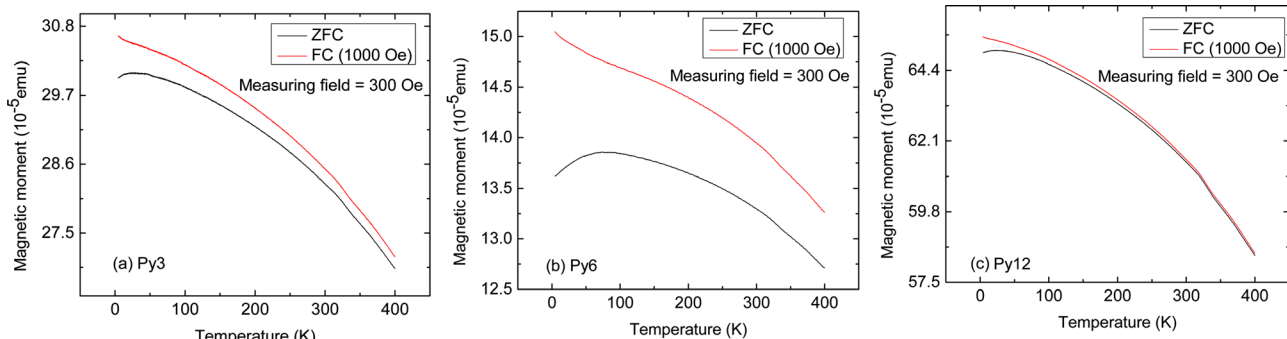
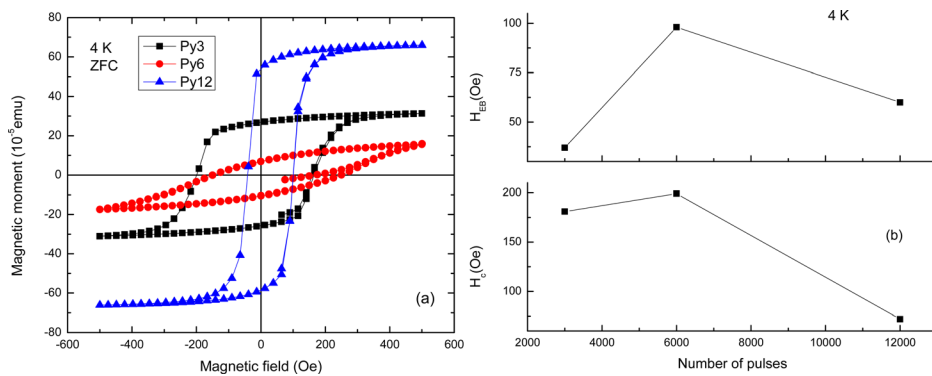


FIG. 28. Temperature (4–400 K) dependence of magnetization under zero field cooled (ZFC) and field cooled (FC, 1000 Oe) conditions for Py3 (a), Py6 (b), and Py12 (c). Reprinted with permission from Rao *et al.*, Curr. Opin. Solid State Mater. Sci. **18**, 140–146 (2014). Copyright 2014 Elsevier.



zero field cooling (ZFC) of the sample to 4 K and then recording the magnetic moment as a function of increasing temperature up to above RT in an applied field of 300 Oe. In the second run, the measurements were repeated for samples field cooled (FC) at 1000 Oe. An apparent  $T_b$ , at which ZFC and FC curves split, is observed  $\geq 400$  K for all three samples. However, it should be noted that the width of splitting between the ZFC and FC curves for the Py6 sample is greater than that of the other two samples. Also, this value of  $T_b$  is much higher than the value ( $\sim 78$  K) previously reported<sup>127</sup> for interacting spherical Py nano particles prepared by magnetron sputtering on  $\text{SiO}_2$  substrates. In the present case, the high  $T_b$  may be ascribed to the existence of large single-domain non-spherical islands that are physically isolated but magnetically coupled.

Figure 29(a) compares the isothermal (4 K) M-H data taken for all three Py3, Py6, and Py12 samples under ZFC conditions. As it can be seen, the three samples exhibit distinctly different M-H loops. Py3 plot (shown in black) shows saturated hysteresis with a RT  $H_c$  of about 200 Oe, Py6 (shown in red) reveals unsaturated loops with much larger hysteresis, and Py12 (shown in blue symbols) presents a narrow ( $H_c \sim 100$  Oe) and saturated hysteresis loop. This final value of  $H_c$  compares well with the values ( $\sim 120$  Oe) previously reported<sup>128</sup> for Py films deposited on MgO substrates. The latter was epitaxial thin films that were prepared by MBE and e-beam evaporation techniques at the substrate temperature of 500 °C. The distinct features observed in the current study reflect the strong influence of island size and shape on the magnetic properties of Py. In addition, these results suggest that the magnetization reversal process and domain configurations in the three samples are not the same. It appears that in the Py6 sample, the domains are strongly pinned during the magnetization reversal process. Another noteworthy feature of the Py6 films is that they all have a positive exchange bias (PEB), i.e., the M-H loop is shifted toward positive magnetic field axis under ZFC conditions. This is unusual for a soft FM like Py interfaced with non-magnetic material like MgO, where one would normally expect to observe a symmetric M-H loop. The values of  $H_{EB}$  and  $H_c$  of Py6 are significantly larger than those of the other two samples as illustrated in Fig. 29(b). This anomaly can largely be attributed to the nature of the microstructure as the films transition from discrete to a coalesced grain structure and a possible accompanying transition in domain dynamics. Trunk and co-authors<sup>129</sup> have shown that a

transition from Bloch domain walls (characterized by out of plane rotation of the magnetization) to Neel domain wall (rotation occurs within the plane of the domain wall) structures takes place with decreasing Py film thickness. Neel wall dynamics were found to govern under conditions where demagnetization effects dominated, and Bloch wall switching begins to emerge as inter domain exchange coupling interactions become more prevalent. This transition has been confirmed by Chen *et al.*<sup>130</sup> in ferromagnetic resonance measurements performed on Py as a function of film thickness. A similar scenario is likely to be occurring in the present system as a function of island morphology and coalescence. Accordingly, the magnetic properties of Py6 are believed to be dominated by a competition between demagnetization and exchange interactions of nearly equal magnitude which leads to observed positive exchange bias (PEB) and appearance of unsaturated and broad M-H loops. Very similar results have been observed for Ni/MgO/TiN films grown on Si (100) substrates.<sup>131</sup>

## 2. $\text{CoFe}_2\text{O}_4$ (CFO)

Spinel oxides, which promise a rich variety of functional properties, are receiving increased interest for potential applications in electronics and communications.<sup>132,133</sup> For instance, the combination of high electrical resistance and room temperature ferromagnetism in  $\text{CoFe}_2\text{O}_4$  (CFO) can be exploited to build active tunnel barriers in spin filter devices.<sup>134</sup> But the future incorporation of spinel oxides as active materials in electronics will critically depend on its epitaxial integration with silicon, which requires a buffer layer to minimize chemical interactions with the silicon substrate and allows for lattice matching. Sánchez *et al.* have epitaxially integrated ferrimagnetic spinel CFO films with Si(111) using  $\text{Sc}_2\text{O}_3$  buffer layers.<sup>135</sup> The large lattice mismatch (17%) between CFO and  $\text{Sc}_2\text{O}_3$  is accommodated through a 7/6 domain matching, where the CFO grows epitaxially with (111) out-of-plane orientation and two in-plane crystal variants (A- and B-type) coexist.

The XRD symmetrical  $\theta$ -2 $\theta$  scan in Fig. 30(a) shows (111) reflections from the Si substrate,  $\text{Sc}_2\text{O}_3$  buffer, and CFO film (36 nm thick), with an absence of peaks corresponding to other reflections or phases. The  $\varphi$ -scans around asymmetrical Si (311),  $\text{Sc}_2\text{O}_3$  (622), and CFO (400) reflections are presented in Fig. 30(b). The three  $\text{Sc}_2\text{O}_3$  (622) peaks are rotated by 60° from the three Si (311) ones,

FIG. 29. Comparison of isothermal (4 K) M-H loops of various Py films (a) variation of exchange bias field ( $H_{EB}$ ) and coercive field ( $H_c$ ) (b) as a function of pulse number. Lines are provided to guide the eye. Reprinted with permission from Rao *et al.*, Curr. Opin. Solid State Mater. Sci. **18**, 140–146 (2014). Copyright 2014 Elsevier.

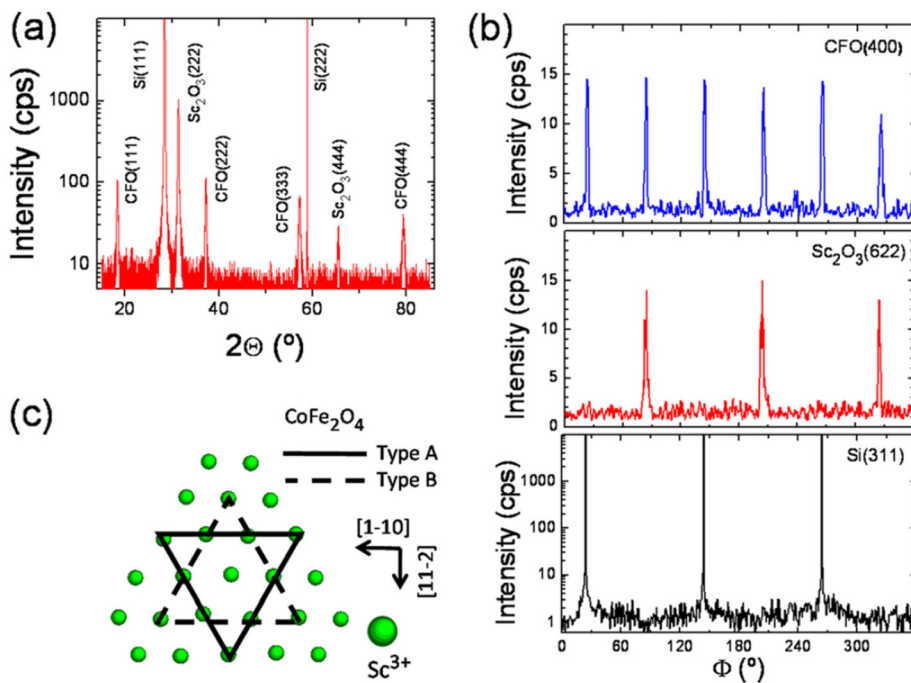


FIG. 30. High resolution XRD  $\theta$ - $2\theta$  symmetrical scan (a) and  $\varphi$ -scans around CFO(400), Sc<sub>2</sub>O<sub>3</sub>(622), and Si(311) reflections (b) measured in a  $t_{\text{CFO}} = 36$  nm sample. The sketch in (c) represents the matching of A and B-type CFO(111) crystal variants on Sc<sub>2</sub>O<sub>3</sub>(111). Reprinted with permission from Appl. Phys. Lett. **99**, 211910 (2011). Copyright 2011 AIP Publishing LLC.

indicating that Sc<sub>2</sub>O<sub>3</sub> presents a single B-type crystal variant. The  $\varphi$ -scan around CFO (400) reflections confirms epitaxial growth, with six peaks indicating the coexistence of both A- and B-type in-plane crystal variants, in appropriately equal concentration. A top view schematic illustration of the matching of CFO (111) with A- and B-type variants on Sc<sub>2</sub>O<sub>3</sub> (111) is presented in Fig. 30(c). In contrast, only a single variant appears when CFO is grown on STO (111) substrates; the B-type variant is not favored.

Figure 31(a) shows a low-magnification cross-section HRTEM view along the [11-2] zone axis. Between the Sc<sub>2</sub>O<sub>3</sub> buffer and the Si (111) substrate the presence of a SiO<sub>x</sub> interfacial layer is evident. It is 2.7 nm thick and probably was formed by oxygen diffusion through the Sc<sub>2</sub>O<sub>3</sub> buffer during subsequent CFO deposition. The region imaged in Fig. 31(b) shows the interface (marked by two arrows) between CFO and Sc<sub>2</sub>O<sub>3</sub>. Individual columns of cations are clearly resolved in both the CFO and Sc<sub>2</sub>O<sub>3</sub> layers. An expanded region is provided in Fig. 31(c), with the sketch in Fig. 31(d) showing the atomic positions (including oxygen atoms) for CFO and Sc<sub>2</sub>O<sub>3</sub> in the (11-2) plane. In Fig. 31(c), the bright spots in Sc<sub>2</sub>O<sub>3</sub> correspond to Sc columns (see the marked rectangle at the lower right side of the HRTEM image and the corresponding marked rectangle in the lower right side of the sketch). In the case of CFO, the brighter spots correspond to mixed Co and Fe columns (see the corresponding rectangles in the upper right sides), with spots of lower intensity corresponding to Fe-rich columns.

### 3. La<sub>0.7</sub>Sr<sub>0.3</sub>MnO<sub>3</sub>/SrRuO<sub>3</sub> (LSMO/SRO)

Of particular interest here is the character of magnetic interfaces which are highly relevant for applications such as magnetic field memories (magnetic tunnel junctions (MTJs); magnetic random accessory memory (MRAM)), read heads, and spin-caloric devices. One of the more frequently studied

systems has been LSMO/SRO bilayers (BLs) and superlattices (SLs). LSMO is a conducting double exchange ferromagnetic metal at RT that is frequently used in conjunction with a biasing layer due to its weak anisotropy and small H<sub>c</sub>. It has a T<sub>C</sub> of about 360 K. SRO is an itinerant ferromagnet, which makes for a good biasing layer due to its large anisotropy and large H<sub>c</sub>. The T<sub>C</sub> of SRO is 160 K. Also, SRO is a commonly used electrode material for ferroelectric oxides. Both LSMO and SRO have high chemical stability, good thermal properties, and a shared perovskite crystal structure that makes for easy integration with related oxide materials. For instance, almost a decade ago, Ke and co-workers reported<sup>136,137</sup> on the magnetic properties of this bilayer. Since then, spin structure and magnetic interactions across the interface have been explored extensively.<sup>138–143</sup> Although LSMO/SRO has been envisaged to have tremendous utility in MTJs and MRAM devices, all these studies were performed on LSMO/SRO deposited on the insulating oxide substrate STO, raising concerns that the results may not accurately reflect films integrated into current CMOS technology. In addition, a comprehensive investigation of magnetic properties of this bilayer as a function of layer thicknesses is missing, which is important to arrive at a complete picture of magnetic exchange coupling across the BL interface.

Epitaxial ferromagnetic metallic oxide LSMO/SRO and La<sub>0.7</sub>Ca<sub>0.3</sub>MnO<sub>3</sub> (LCMO)/SRO BLs were grown<sup>144–147</sup> on Si (100) by PLD technique. Two samples were then characterized in detail: LSMO (100 nm)/SRO (180 nm)/STO/MgO/TiN/Si and LSMO (100 nm)/SRO (45 nm)/STO/MgO/TiN/Si. Except for the SRO layer thickness, the thicknesses of the remaining layers were kept constant. It was evident from the XRD pattern that all the layers showed preferential (00l) orientation. From the 2θ XRD data for the (002) peak, the OOP lattice parameter of LSMO was determined to be 3.844 Å, close to the bulk value<sup>148</sup> of 3.850 Å. The  $\varphi$ -scan pattern showed 4

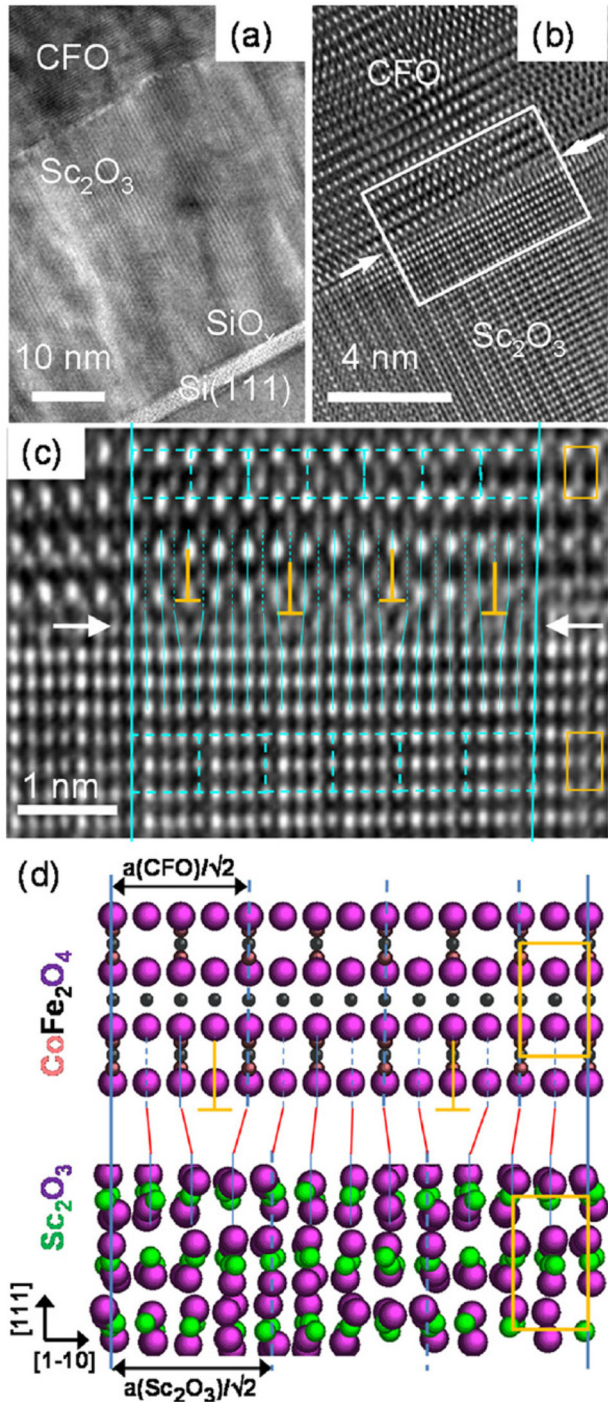


FIG. 31. HRTEM cross-sectional view along the Si[11-2] zone axis. (a) Low magnification view showing the CFO and  $\text{Sc}_2\text{O}_3$  layers, with presence of  $\text{SiO}_x$  interfacial layer between  $\text{Si}(111)$  and  $\text{Sc}_2\text{O}_3$ . (b) High resolution image of the CFO/ $\text{Sc}_2\text{O}_3$  interface (marked by two arrows). (c) Zoom around the CFO/ $\text{Sc}_2\text{O}_3$  interface (the zoomed area is marked in panel (b)). Dashed lines mark horizontal (111) and vertical (110) planes of CFO and  $\text{Sc}_2\text{O}_3$ . The four dislocations present along the domain are marked. (d) Sketch of the atomic matching at the interface, including oxygen atoms. The rectangles at the right correspond to the equivalent rectangles marked in the right of panel (c). Reprinted with permission from Appl. Phys. Lett. **99**, 211910 (2011). Copyright 2011 AIP Publishing LLC.

peaks separated by  $\sim 90^\circ$  indicating its pseudo cubic/rhombohedral symmetry and establishing the cube-on-cube epitaxial relationship of the LSMO with the underlying substrate Si (100). Figure 32(a) shows a typical bright-field

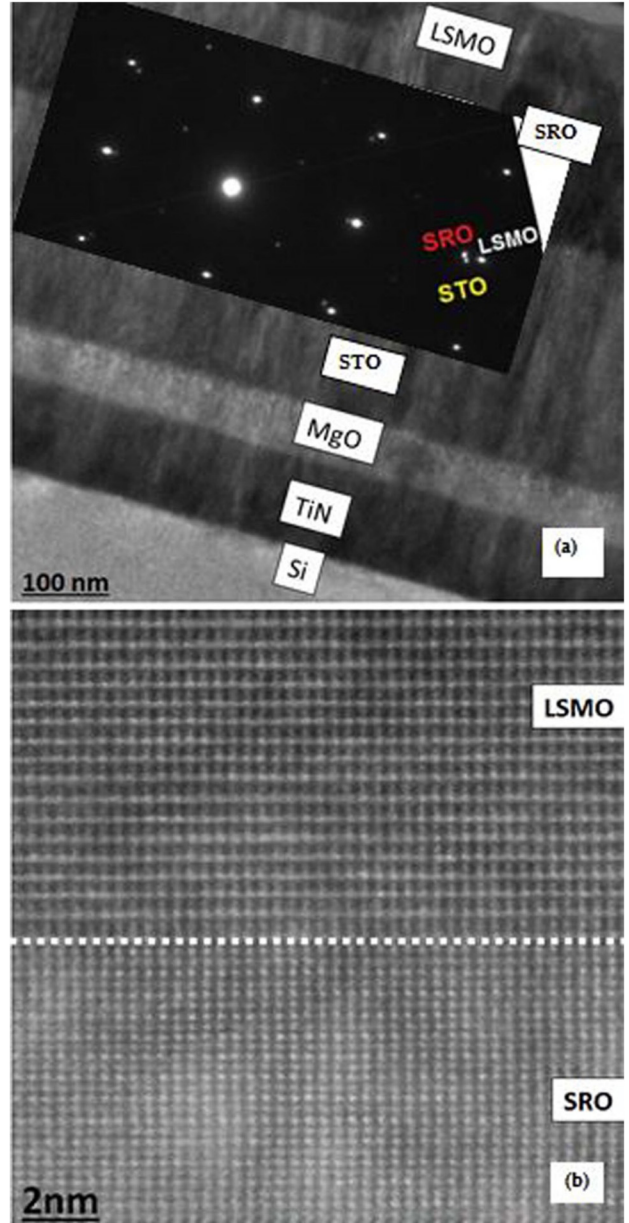
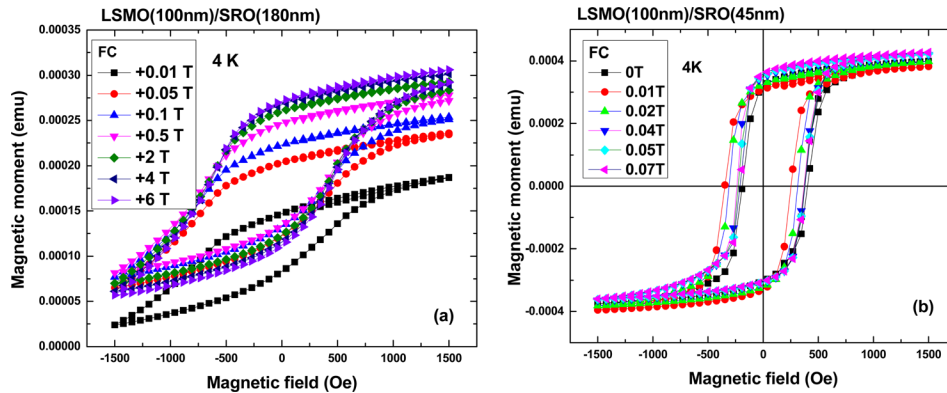


FIG. 32. (a) Bright field cross-section TEM image (main panel) taken from sample, where LSMO ( $\sim 100$  nm) and SRO ( $\sim 180$  nm) films were grown at  $650^\circ\text{C}$ . All 5-layers are marked. The scale bar is 100 nm. The inset shows  $\langle 110 \rangle$  zone-axis pattern (ZAP) for LSMO/SRO/STO heterostructure. (b) STEM-Z contrast image collected at LSMO/SRO (001) interface. Reprinted with permission from J. Appl. Phys. **117**, 17B711 (2015). Copyright 2015 AIP Publishing LLC.

cross-section TEM image of LSMO/SRO/STO/MgO/TiN/Si (100), in which all the layers have been labeled. The thicknesses of LSMO, SRO, STO, MgO, and TiN have been estimated to be  $\sim 100$ , 180, 260, 60, and 100 nm, respectively. All five layers are uniform and continuous. The  $\langle 100 \rangle$  zone axis SADP of the LSMO/SRO/STO heterostructure is shown in Fig. 32(b). Since the lattice constants of STO, SRO, and LSMO are very close to each other ( $a_{\text{STO}} = 3.905 \text{ \AA}$ ,  $a_{\text{SRO}} = 3.923 \text{ \AA}$ , and  $a_{\text{LSMO}} = 3.850 \text{ \AA}$ ), the diffraction points for their low-index planes overlap with each other and therefore cannot be distinguished. However, the splitting of diffraction points for higher-index planes can be observed. For example, the diffraction points corresponding to SRO (040),



STO (040), and LSMO (040) planes are distinguishable and labeled in Fig. 32(b). The alignment of three sets of diffraction spots from different layers confirms the cube-on-cube epitaxial relationship among the top three layers.

Figures 33(a) and 33(b) show the in-plane isothermal (4 K) M-H behavior of the two samples when cooled under various magnetic fields with the field sweep range of  $\pm 1500$  Oe. Of particular interest is the unusual vertical M-H loop shift along the magnetic axis ( $M_{\text{shift}}$ ) observed for the heterostructure with the 180 nm thick SRO layer (see Fig. 33(a)). Such  $M_{\text{shift}}$  is retained even up to the field range of  $\pm 6$  kOe. Above 6 kOe, the shift disappears and a symmetrical hysteresis loop centered at the origin is observed. In sharp contrast, at the same temperature and under the same field sweep range, a normal (very little vertical shift) M-H loop is observed for the sample with 45 nm SRO thickness, as shown in Fig. 33(b). In both samples, the LSMO thickness was kept constant at 100 nm. In the former case, as can be seen in Fig. 33(a), the  $M_{\text{shift}}$  was robust even under the cooling field as high as 6 T. When the LSMO (100 nm)/SRO (180 nm)/STO/MgO/TiN/Si (100) was cooled under the field with negative polarity, the M-H loop shifts vertically down. The  $M_{\text{shift}}$  was strongly dependent on the magnitude of the cooling field, and the biasing layer (SRO) thickness. It appeared that the SRO moment was frozen in place in the sample with 45 nm SRO thickness, and only the magnetization reversal of LSMO was observed. This was a clear demonstration of the effect that biasing layer (SRO) thickness can have on the magnetic characteristics of bilayer films. It was believed that the characteristic large uniaxial magnetocrystalline anisotropy (induced by the large spin orbit coupling (SOC) of Ru<sup>4+</sup>) observed in thicker SRO layers leads to the large  $M_{\text{shift}}$  that was absent in the sample with thinner SRO layer due to suppression of its magnetocrystalline anisotropy. However, it may also be that the easy magnetization axis was rotated<sup>149,150</sup> as the SRO layer thickness was changed, or that different domain variants were activated in the two SRO samples.

#### D. Emerging topological insulators

##### 1. Sr<sub>3</sub>SnO (SSO)

Topological insulators (TIs) are an exciting class of materials with unique properties making them potentially useful in high speed, low power digital devices, quantum

FIG. 33. Comparison of M-H loops of two samples: (a) LSMO(100 nm)/SRO(180 nm) and (b) LSMO(100 nm)/SRO(45 nm). Reprinted with permission from J. Appl. Phys. **117**, 17B711 (2015). Copyright 2015 AIP Publishing LLC.

computing, and spintronics. The primary defining characteristic of a TI is that while the bulk state is insulating, the surfaces are highly conductive, owing to the presence of a finite bulk energy band gap and gapless surface states

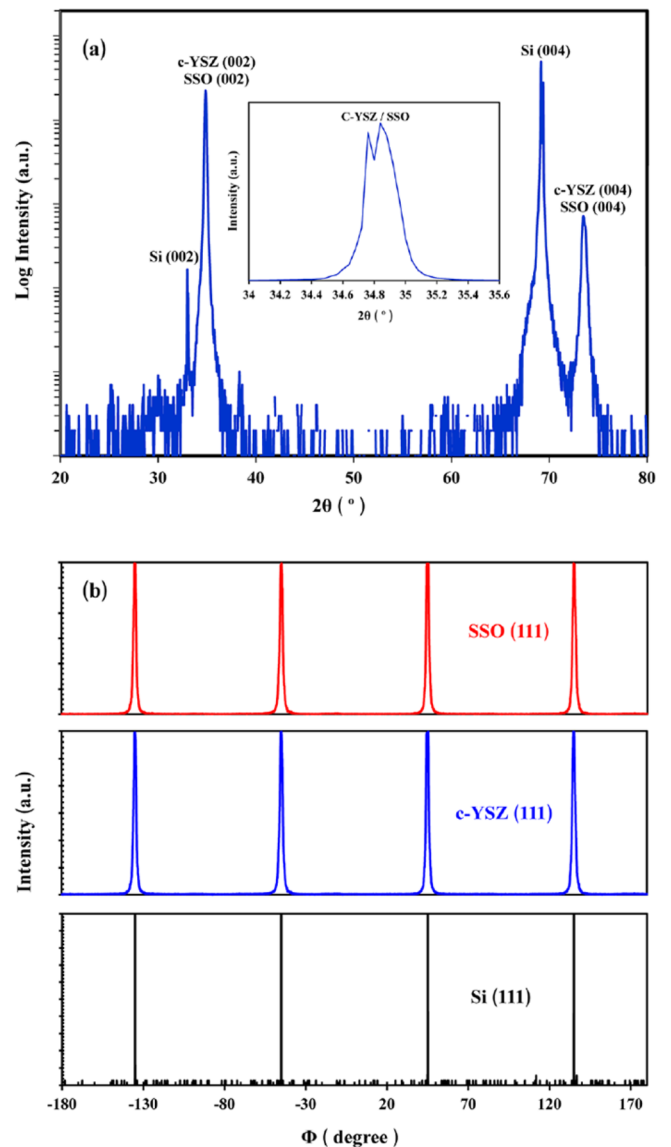


FIG. 34. (a)  $\theta$ - $2\theta$  XRD pattern of the SSO/c-YSZ/Si (001) heterostructure. (b) X-ray  $\phi$ -scan for (111), (111), and (111) reflections of SSO, c-YSZ, and Si, respectively. Reprinted with permission from Appl. Phys. Lett. **103**, 112101 (2013). Copyright 2013 AIP Publishing LLC.

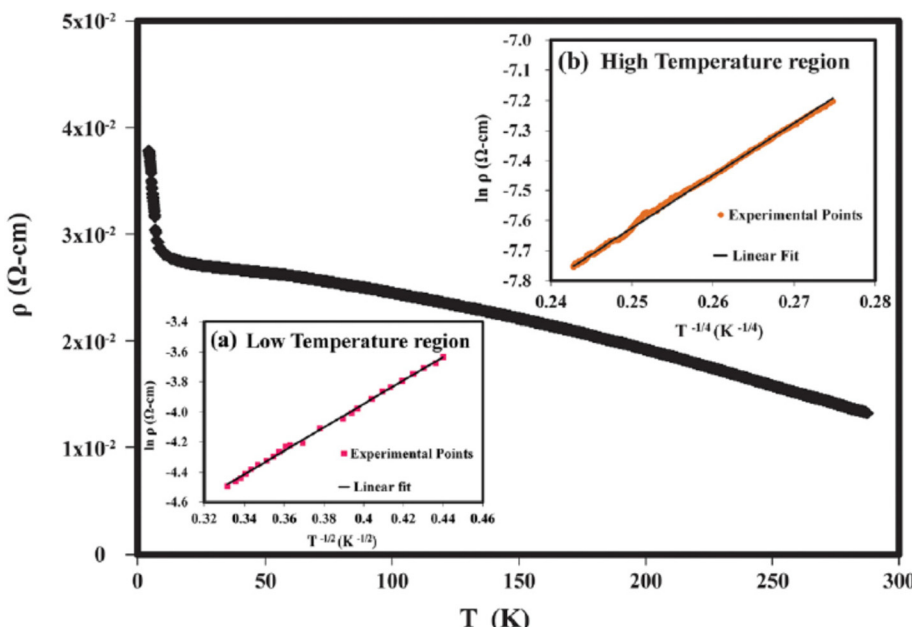


FIG. 35. Resistivity as a function of temperature (5 K–285 K). Bottom left inset (a):  $\ln \rho$  vs.  $T^{-1/2}$  at low temperature (5–10 K). Top right inset (b):  $\ln \rho$  vs.  $T^{-1/4}$  at high temperature (170–285 K) along with best fit results obtained by least-square fitting. Reprinted with permission from Appl. Phys. Lett. **103**, 112101 (2013). Copyright 2013 AIP Publishing LLC.

resulting from strong spin-orbit coupling (SOC).<sup>151–153</sup> As such, these systems can be the source of large spin currents which have been shown to be very efficient in driving spin torque switching of adjacent magnetic layers.<sup>154,155</sup>

$\text{Sr}_3\text{SnO}$  (SSO) crystallizes in the cubic system with a space group Pm3m and a theoretical unit cell of 5.12 Å. SSO has an indirect local density approximation (LDA) band gap of 0.1 eV throughout the Brillouin zone.<sup>156,157</sup> The first epitaxial integration of this TI candidate material on silicon substrate has recently been reported<sup>158–160</sup> and its physical properties were studied. X-ray (see Fig. 34) and electron diffraction patterns confirm the epitaxial nature of the layers with cube-on-cube orientation relationship: (001)[100]SSO || (001)[100]c-YSZ || (001)[100]Si.

The temperature dependent resistivity<sup>158</sup> in the temperature range of 5–285 K is shown in Fig. 35. This figure clearly reveals that the resistivity was constant at intermediate temperatures (15–100 K) followed by a sharp rise as the sample was cooled below (15 K), which is consistent with the extrinsic doping behavior. These results were analyzed using the variable range hopping (VRH) model, which describes low-temperature conduction in strongly disordered systems characterized by localized charge-carrier states. This model was found to best describe the conduction mechanism of the SSO thin films. The plot suggests that there are two linear transport regimes: one below 10 K (shown in lower left inset) and the other in the range of 170–285 K (shown in upper right inset).

As is the case for many oxide systems, oxygen vacancies act as intrinsic donors in SSO and have a profound influence on its physical and chemical properties.<sup>161</sup> In fact, SSO can be made ferromagnetic by tuning the oxide stoichiometry.<sup>158</sup> This ferromagnetic behavior was studied<sup>159</sup> by systematically changing the oxygen vacancy concentration in SSO samples through annealing. Both  $M_s$  and  $H_c$  were found to be sensitive to changes in the oxygen vacancy concentration, revealing that vacuum annealing (VA) enhances  $M_s$  and  $H_c$ , while oxygen annealing (OA) degrades both properties. The magnetic hysteresis has been measured from –10 to +10 kOe as a

function of temperature. The diamagnetic contributions of the substrate and buffer have been subtracted and the magnetization starts to saturate at about 3500 Oe. The room temperature values of saturated magnetic moment and  $H_c$  for SSO thin films were found to be  $\sim 7.3$  emu/cm<sup>3</sup> and 75 Oe, respectively. Both the coercive field and the saturation moment decrease with increasing temperature, consistent with the typical ferromagnetic behavior. To shed some light on the role of vacancies, ultraviolet photo spectroscopy (UPS) was carried out<sup>159</sup> to investigate the variation of work function ( $\Delta$ ) and identify the occupied electronic valence states present in the as-deposited (AD), OA, and VA samples. By definition,  $\Delta$  is the difference between the bulk chemical potential of the electrons and the electrostatic potential energy of the electrons in the vacuum just outside the surface. It should be mentioned that the work function ( $\Delta$ ) is not a material constant but rather can be adjusted through carrier doping or surface dipole modification. Many reports<sup>162,163</sup> have now shown that one can change  $\Delta$  substantially by manipulating the oxygen content during growth conditions. In this study, the  $\Delta$  of all the samples were determined by measuring the highest binding energy (BE) cutoff using a He I excitation photon source (21.2 eV). A comparison of the highest BE cutoff edge for as-deposited (AD), OA, and VA samples is shown in Figs. 36(a)–36(c). The enlarged UPS spectra are displayed in Fig. 36(b) for clarity. They reveal that the cutoff edge shifts such that VA > AD > OA. Subtracting three BE values from 21.2 eV, the  $\Delta$  are estimated to be 4.54, 4.38, and 4.02 eV for OA, AD, and VA samples, respectively. It is surmised that values reflect changes in the surface. Similar results have been reported<sup>163,164</sup> in  $\text{SnO}_2$  and  $\text{In}_2\text{O}_3$  and attributed to carrier doping by oxygen vacancies.

## E. New transparent conductors

### 1. ZnO

Zinc oxide (ZnO) has desirable electro-optical, acousto-optical, piezoelectric, and luminescence properties that make

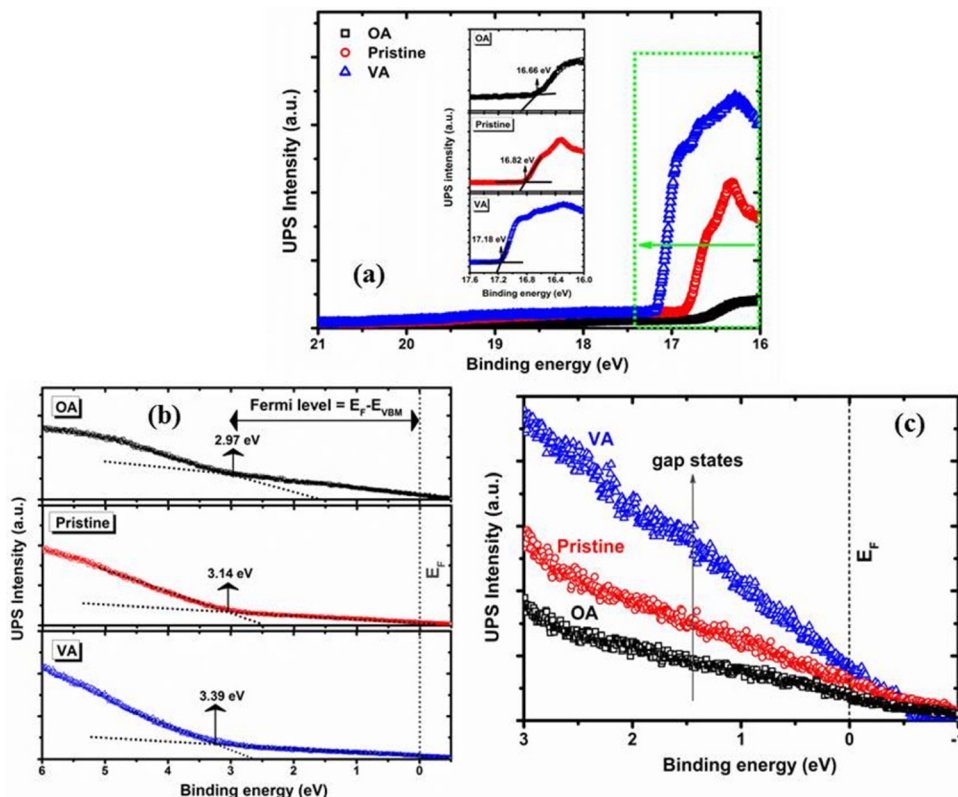


FIG. 36. UPS spectra for oxygen annealed (OA), as deposited (pristine), and vacuum annealed (VA) samples: (a) the highest binding energy cutoff edge (the inset shows the expanded view); (b) the difference between valence band maximum and Fermi energy ( $E_{VBM}-E_F$ ), and (c) gap states in the valence band region. Reprinted with permission from J. Appl. Phys. **116**, 164903 (2014). Copyright 2014 AIP Publishing LLC.

ZnO an attractive material for a variety of applications. In particular, its wide band gap ( $E_g = 3.37$  eV) and large exciton binding energy (60 meV) make it very attractive as a potential source for blue and ultraviolet light, e.g., as LEDs and laser diodes.<sup>165–170</sup> ZnO can be also doped with Ga and Al making it a promising alternative transparent conducting oxide (TCO) for indium tin oxide (ITO), which is currently the TCO of choice for solar cells, flat panel displays, heat mirrors, and LEDs. Finally, ZnO can be tuned between ferromagnetic and paramagnetic states<sup>171</sup> by controlling its stoichiometry (oxygen vacancy content).

Traditionally, high quality epitaxial ZnO films have been grown on c-sapphire, r-sapphire, STO, LAO, and MgO.<sup>172–174</sup> Next generation solid state devices will require integration of various functions on practical substrates, particularly on Si (100). To that end, ZnO(0001) single-crystalline thin films were grown<sup>175</sup> on Si(001) using a c-YSZ buffer and details on the epitaxy and interface structure studied. The IP epitaxial relationship between ZnO and c-YSZ showed an interesting dependence on growth temperature where it changed from (0001)[−2110]ZnO || (001)[110]c-YSZ to (0001)[−2110]ZnO || (001)[100]c-YSZ as the deposition temperature increased from 500 to 750 °C. At intermediate temperatures, a mixture of these two orientations was observed. It was found that the epitaxial relationships are determined by the surface termination characteristics of c-YSZ across the ZnO/c-YSZ interface. The appearance of ZnO(0002) peak at  $2\theta \sim 34.44^\circ$  demonstrates that a completely relaxed ZnO film has grown on the c-YSZ buffer layer.

Figure 37(a) shows a low magnification bright field cross-section image of the ZnO/c-YSZ/Si heterostructure grown at 650 °C. Based on this image, the thickness of the c-YSZ and ZnO films is estimated to be about 100 and 1400 nm, respectively; no interfacial reaction is evident in high resolution images. SADPs taken from the ZnO/c-YSZ interface in the samples grown at 500, 650, and 750 °C are depicted in Figs. 37(b) and 37(c). Spots as well as the indices from the c-YSZ [110] zone are highlighted in red in all patterns. In Fig. 37(b), the spots from the ZnO film corresponding to the [2-1-1 0] zone are shown in green. Two different domains are present in the sample grown at 650 °C. This is further evidenced by the SADP presented in Fig. 37(c) where spots from both [2-1-10] zone and [10-10] zone (highlighted in violet) of ZnO are observed.

The optical and electrical properties of these ZnO thin films have been previously reported in detail.<sup>176</sup> Figure 38 shows the Raman spectrum from the ZnO grown at  $\sim 350$  °C. Prominent Raman peaks corresponding to the E2 (high) and the A1 (LO) phonon modes are observed. The E2 (high) phonon vibration is most sensitive to any IP strain in this orientation. It was observed that the E2 (high) mode frequency at  $\sim 437.84$  cm<sup>−1</sup> matched well with the relaxed bulk ZnO value from the literature.<sup>177</sup> This further corroborates the X-ray measurements,<sup>176</sup> which indicated that the ZnO film grew nearly fully relaxed on the buffered Si (100) substrate.

The RT PL spectra for r-plane ZnO/YSZ/Si(100) and c-plane ZnO/YSZ/Si(100) samples grown<sup>178</sup> under similar

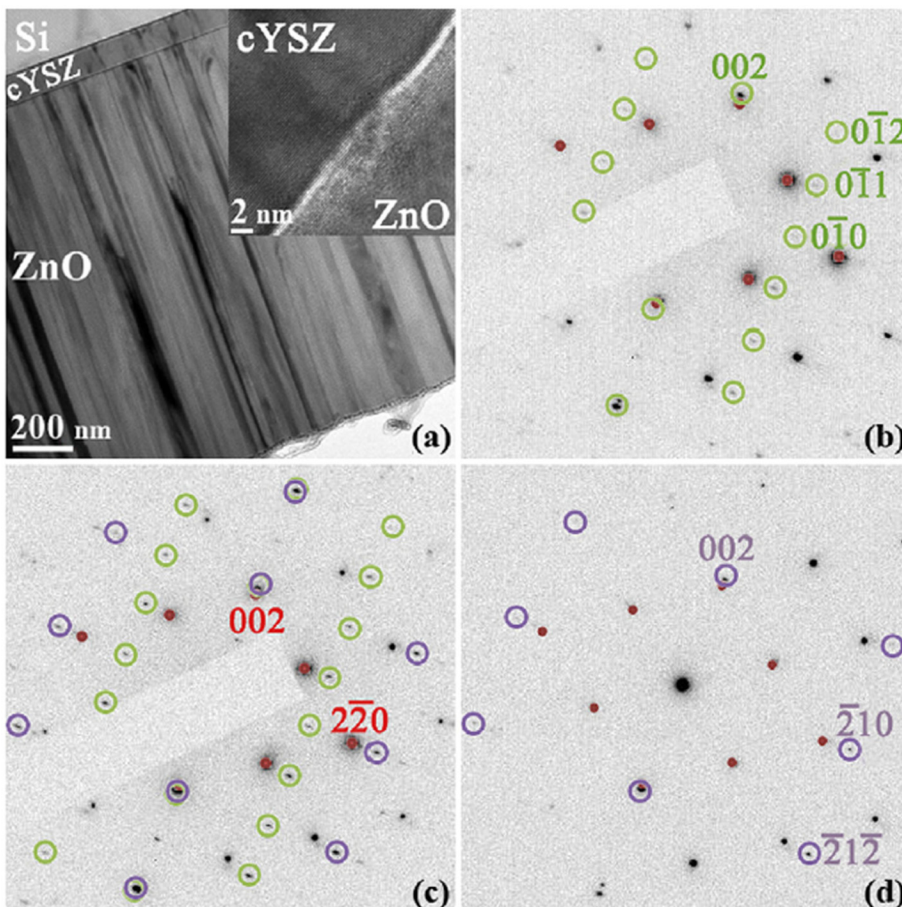


FIG. 37. (a) Bright field cross section image taken from the ZnO/c-YSZ/Si(100) heterostructure where the ZnO film was grown at 650°C. Other images depict the SAED pattern from the ZnO/c-YSZ interface where ZnO was deposited at (b) 500, (c) 650, and (d) 750°C. (Note: The spots from c-YSZ[110], ZnO[[2-1-1 0]], and ZnO[10-10] zones are highlighted in red, green, and violet, respectively.) Reprinted with permission from Appl. Phys. Lett. **102**, 101602 (2013). Copyright 2013 AIP Publishing LLC.

conditions are shown in Fig. 39. Both of these spectra exhibit near band emission at 3.3 eV, which is attributed to excitonic recombination.<sup>178</sup> The excitonic emission in r-plane ZnO is approximately five times stronger than that in c-plane ZnO. The stronger excitonic emission observed in r-ZnO can be attributed to the higher probability of radiative recombination due to reduced polarization effects. Another important feature in the spectra shown in Fig. 39 is the prominent broad emission band observed in c-ZnO, which peaks at 2.35 eV.

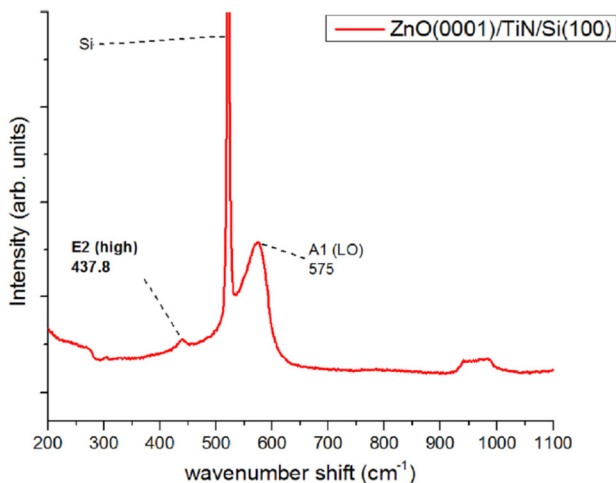


FIG. 38. Raman spectra of ZnO grown at ~350°C show the E2(high) ZnO mode. Reprinted with permission from J. Appl. Phys. **115**, 043513 (2014). Copyright 2014 AIP Publishing LLC.

This emission, termed as green band emission, is often attributed to mid-gap point defect levels such as charged oxygen vacancies or zinc interstitials.<sup>179,180</sup> It is interesting to note that green band emission is completely suppressed for r-plane ZnO, which indicates that the concentration of defects responsible for green band emission is vastly reduced in these films. The reduced green band in r-ZnO films may also

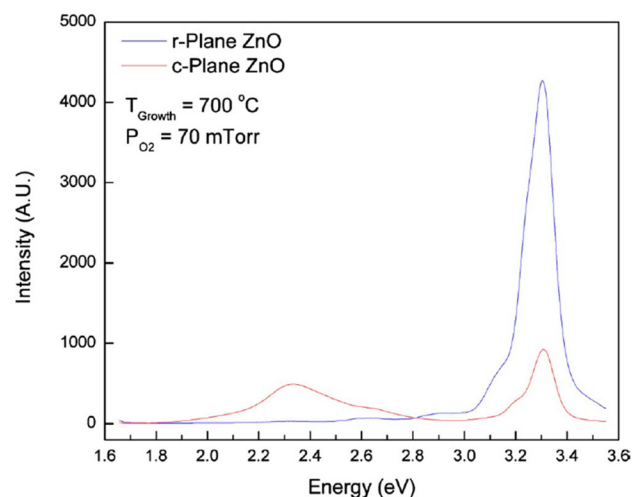


FIG. 39. PL spectra of r-plane ZnO/YSZ/Si(100) and c-plane samples deposited at similar conditions. The first 50 pulses of ZnO for c-ZnO were deposited at low oxygen pressure of 0.5 mTorr to nucleate the c-orientation of ZnO. Reprinted with permission from J. Appl. Phys. **107**, 113530 (2010). Copyright 2010 AIP Publishing LLC.

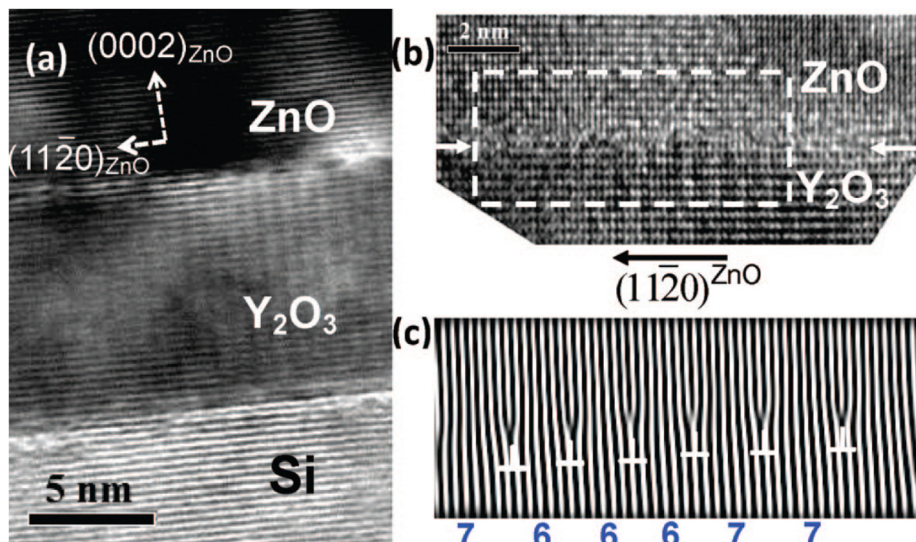


FIG. 40. Cross-sectional TEM micrograph recorded along [11-2]<sub>Si</sub> projection. The high resolution image of the ZnO/Y<sub>2</sub>O<sub>3</sub> interface is shown in (b). The Fourier filtered image of the area enclosed by the dashed rectangle in (b) is displayed in (c), on which the number of (4-40)<sub>Y2O3</sub> planes between adjacent extra (11-20)<sub>ZnO</sub> half-planes is marked below. Reprinted with permission from Liu *et al.*, Cryst. Growth Des. **9**, 239 (2009). Copyright 2009 American Chemical Society.

explain the stronger excitonic emission observed in r-ZnO films since the probability of excitonic recombination should increase as the loses to mid-gap states drop. The strong excitonic emission, with negligible emission in visible range, in r-plane ZnO indicates the good optical quality of these films.

The growth of ZnO on Si(111) substrates is pretty straightforward because of the substrate because of the similarity in the crystal structure. High-quality ZnO epitaxial films have been grown by PLD on Si (111) substrates using a 10 nm thick high-*k* Y<sub>2</sub>O<sub>3</sub> (YO) oxide buffer layer.<sup>181</sup> XRD and TEM determine that the epitaxial relationship between ZnO and YO follows (0001)(2-1-10)ZnO || (111)(10-1) YO. The ZnO lattice aligns with the hexagonal O sublattice in YO and the interfacial structure can be well described by DME with 7 or 8 ZnO {11-20} planes matching 6 or 7 {4-40} planes of YO. Fig. 40(a) is the TEM micrograph collected along [11-2]Si projection which shows atomically sharp ZnO/YO and YO/Si interfaces; no intermediate reaction layer is observed at either interfaces.<sup>181</sup> The periodic contrast variation along the ZnO/YO interface with an average spacing of ~1.2 nm is found in the high resolution TEM images, see Fig. 40(b), which is attributed to the induced strain field of the misfit dislocations. The nearly periodically arranged extra (11-20)ZnO half-planes with a spacing of 6 or 7 (4-40) YO planes are clearly seen in the Fourier filtered image shown in Fig. 40(c), confirming the DME of ZnO on YO (111). PL measurements on these samples indicate that superior optical properties were obtained.<sup>181</sup>

ZnO (0 0 0 2) epitaxial films have been successfully grown on Si (1 1 1) with CeO<sub>2</sub> as a buffer layer using pulsed laser deposition by Wong and co-authors.<sup>182</sup> Despite the large lattice mismatch (14.8%) between ZnO and CeO<sub>2</sub>, good film quality and reduced interface strain were achieved, as indicated in the Fourier filtered HRTEM image (not shown). The epitaxial relationship of ZnO and CeO<sub>2</sub> on the Si substrate was determined to be (0 0 2)[2 1 0]ZnO || (1 1 1)[1 1 2]CeO<sub>2</sub> || (1 1 1)[1 1 2]Si.

Finally, Wang *et al.* have reported high quality ZnO epitaxial layers that were deposited on Si (111) by incorporating a

MgO(111)/Mg(0001) template layer using a three-step, low temperature deposition approach.<sup>183</sup> Good epitaxy was confirmed with *in situ* reflection high-energy electron diffraction observation and *ex situ* characterization by TEM, XRD, and PL. DME of the ZnO is realized on MgO (111) via matching of 10-unit ZnO cells and 11-unit MgO cells along the [1-100]<sub>ZnO</sub> direction resulting in only -0.8% residual strain. The DME is confirmed in TEM studies by the presence of misfit dislocations at the sharp interface of MgO/ZnO. This study demonstrates the utility of the MgO layer as a well-behaved template for high crystal-quality ZnO epitaxial growth.

## F. Smart materials

### 1. VO<sub>2</sub>

Vanadium dioxide (VO<sub>2</sub>) belongs to a family of “smart materials” that exhibit a semiconductor-to-metal first-order phase transition (SMT) near 340 K (68 °C), which is accompanied by an abrupt change in resistivity and near-infrared transmission. VO<sub>2</sub> is a strongly correlated electron system with a small band gap (~0.7 eV at room temperature) that reacts strongly to temperature variations, electric or magnetic fields, and pressure variations in the vicinity of its semiconductor-to-metal transition (SMT). At the SMT, the material undergoes changes in the electronic band structure associated with atomic rearrangement from the more symmetric tetragonal (P42/mnm) phase to the less symmetric monoclinic (P21/c) phase.<sup>184–186</sup> VO<sub>2</sub> is attracting attention because the SMT is close to RT, thus making its implementation in devices straightforward. Of particular interest here, it has been reported that strain induced by SMT can be used to modulate the properties of adjacent magnetic layers (such as Ni).<sup>187</sup>

VO<sub>2</sub> epitaxial thin films have been deposited onto silicon substrates using NiO/c-YSZ buffer layers.<sup>188–191</sup> The IP alignment of the VO<sub>2</sub> film was studied via  $\varphi$ -scan XRD on the (011) reflection of VO<sub>2</sub> ( $2\theta = 27.80^\circ$  and  $\psi = 45.00^\circ$ ). In this case, six peaks with an azimuthal separation of 30°, aligned with the (200) reflection of NiO, were observed. The

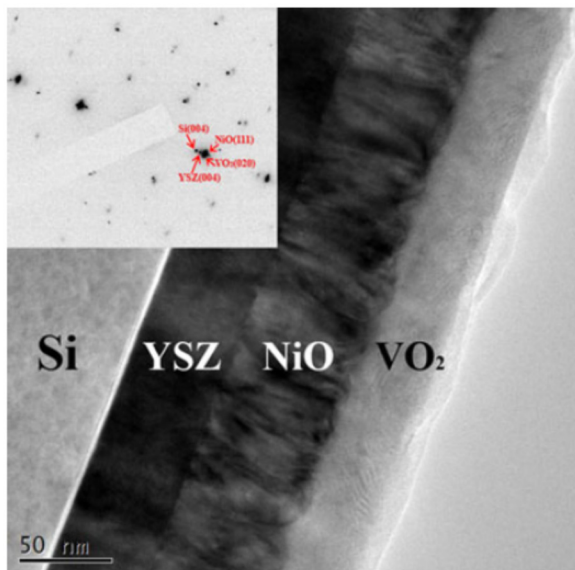


FIG. 41. TEM cross-sectional bright field image of the  $\text{VO}_2/\text{NiO}/\text{YSZ}/\text{Si}(001)$  heterostructure and the SAED pattern ( $\text{Si}[110]$ ,  $\text{YSZ}[110]$ ,  $\text{NiO}[1-10]$ ,  $\text{VO}_2[201]$ , and  $\text{VO}_2[307]$  zones). Reprinted with permission from Appl. Phys. Lett. **103**, 252109 (2013). Copyright 2013 AIP Publishing LLC.

six  $\varphi$ -peaks result from 2-fold symmetry of  $\text{VO}_2$  along its b-direction aligning with three equally probable variants of  $\text{NiO}$  (111), rotated by  $120^\circ$  from each other. Based on this information, the epitaxial relationship between the  $\text{VO}_2$  and  $\text{NiO}$  films was  $(010)\text{VO}_2 \parallel (111)\text{NiO}$  and  $[001]\text{VO}_2 \parallel [110]\text{NiO}$ .

Microstructural studies were completed by TEM imaging and diffraction. Figure 41 displays the bright field cross sectional image of the  $\text{VO}_2/\text{NiO}/\text{YSZ}/\text{Si}(001)$  heterostructure. The epitaxial growth and the proposed epitaxial relationships are confirmed by the indexed SADP, shown in the inset of Fig. 41. The columnar structure in the  $\text{NiO}$  film indicates the in-plane rotation of the grains, as discussed earlier.

The SMT transition has been found to be strongly affected by the strain state of the film. Fig. 42 summarizes the SMT parameters, namely, transition temperature, hysteresis, and amplitude, as a function of thickness. As depicted in Fig. 42, the SMT hysteresis monotonically decreases with the film thickness. XRD and AFM investigations clearly showed that the grain size increases, as the films get thicker. The transition amplitude approaches five orders of magnitude, and the

hysteresis decreased to about 3 K, as the thickness of  $\text{VO}_2$  layers increased from about 10 to 200 nm. This is believed to be a result of the unrelaxed stress that is present in the thinner films. A correlation between the SMT properties and the stress can be explained using a phenomenological model proposed by Narayan and Bhosle.<sup>192</sup> In unrelaxed samples, the a-axis of monoclinic (M1)  $\text{VO}_2$  (or c-axis of tetragonal  $\text{VO}_2$ ) is under tensile strain.<sup>193</sup> An extended  $\text{V}^{4+}\text{-}\text{V}^{4+}$  spacing along the c-axis results in a large activation barrier due to direct overlapping of d-orbitals. This in turn stabilizes the covalent monoclinic phase and hinders the phase transformation of low temperature monoclinic phase to the high temperature rutile phase. This is the reason why SMT was observed to above 341 K. In contrast, the SMT takes place at lower temperatures, if the  $\text{V}^{4+}\text{-}\text{V}^{4+}$  spacing decreases, as would be the case for a compressive residual strain applied along the c-axis of tetragonal  $\text{VO}_2$ . As the thickness increases, beyond the critical thickness, the misfit strain relaxes and approaches a fully relaxed film and the SMT temperature approaches the bulk value of 341 K. A very small deviation from the bulk SMT may still be present originating from thermal expansion and defect-related strains, which are on the order of 0.5% and very hard to relax. As depicted in Fig. 42, the SMT hysteresis monotonically decreases with the film thickness. XRD and AFM investigations clearly showed that the grain size increases, as the films get thicker. The transition amplitude increased by about five orders of magnitude, and the hysteresis decreased to about 3 K, as the thickness of  $\text{VO}_2$  layers increased from about 10 to 200 nm. These observations were explained based on strain characteristics and overall defect and grain boundary content using the proposed phenomenological thermodynamic model.<sup>194</sup>

## 2. NiO

Nickel oxide (NiO) is a p-type semiconducting material with a band gap<sup>195</sup> of 3.6–4.0 eV that could potentially serve a wide range of applications such as solar cells, spin-valve giant magnetoresistance sensors, transparent conducting electrodes, gas sensors, electrochemical display devices, and organic LEDs. Moreover, NiO has been used in the fabrication of oxide p-n junctions as the p-type layer. Potential applications of NiO as an epitaxial electrode or gate oxide layer opens up exciting possibilities (display technology, solid oxide fuel cells, transparent conductors and gas sensors) in devices where it is combined with the SMT properties of  $\text{VO}_2$  thin films.<sup>196–202</sup> Finally, p-NiO can be converted to n-type behavior by controlled high power pulsed laser irradiation which could be tapped to realize next-generation efficient p-n junctions and complementary oxide based transistor applications in oxide electronics.<sup>190</sup>

In that spirit, NiO was epitaxially integrated<sup>190,202</sup> with silicon substrate. The  $\varphi$ -scan XRD was conducted on the (200) reflection of NiO ( $2\theta = 43.31^\circ$  and  $\psi = 54.24^\circ$ ) to investigate the epitaxial relationship at the YSZ/NiO. The appearance of six sharp peaks confirms the epitaxial growth of NiO on the YSZ buffer layer. The presence of these strong peaks with a  $30^\circ$  angular separation is attributed to the 3-fold symmetry of the NiO structure along the [111] direction and

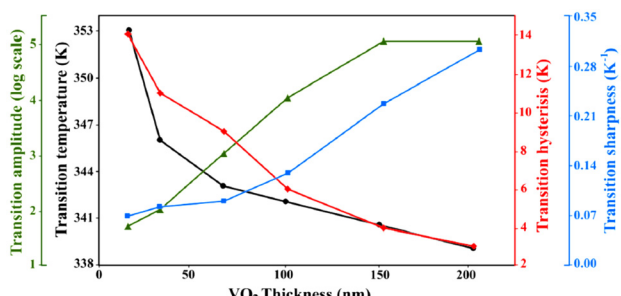


FIG. 42. A summary of SMT parameters of  $\text{VO}_2$  epitaxial thin films with several thicknesses. Reprinted with permission from J. Appl. Phys. **115**, 164311 (2014). Copyright 2014 AIP Publishing LLC.

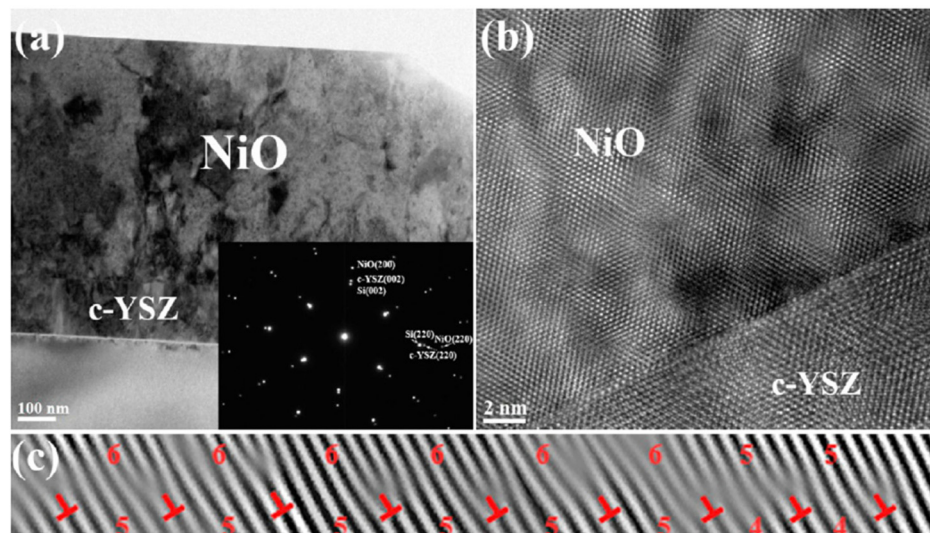


FIG. 43. (a) Cross-section low-magnification TEM image from the NiO{100}/c-YSZ{001}/Si{001} heterostructure where the inset depicts the indexed SAED pattern, (b) high-magnification TEM micrograph showing the NiO{100}/c-YSZ{100} interface, and (c) arrangement of misfit dislocation and alternation of 6/5 and 5/4 matching domains across the NiO/c-YSZ interface. Reprinted with permission from Molaei *et al.*, Cryst. Growth Des. **13**, 5459–5465 (2013). Copyright 2013 American Chemical Society.

four crystallographically equivalent directions on the cubic YSZ structure, which has a 4-fold symmetry.

It was possible<sup>202</sup> to systematically control crystallographic characteristics and electrical properties of nickel oxide epitaxial thin films integrated with c-YSZ-buffered silicon (001) substrates. The NiO epilayers were grown under several oxygen partial pressures by PLD. The OOP orientation of the NiO layers changed from  $\langle 111 \rangle$  at lower pressures ( $7 \times 10^{-6}$  Torr) to  $\langle 100 \rangle$  at higher pressures ( $5 \times 10^{-2}$  Torr). This observation was attributed to the nature of surface termination and templating effect of the c-YSZ {100} platform at different pressures. X-ray diffract scans showed the epitaxial alignment across the NiO/c-YSZ interface to be  $\{111\}\text{NiO} \parallel \{100\}\text{c-YSZ}$  and  $\langle 110 \rangle\text{NiO} \parallel \langle 100 \rangle\text{c-YSZ}$  for the heterostructure grown at a low pressure and  $\{100\}\text{NiO} \parallel \{100\}\text{c-YSZ}$  and  $\langle 100 \rangle\text{NiO} \parallel \langle 100 \rangle\text{c-YSZ}$  for the heterostructure grown under high oxygen pressure. As presented in Fig. 43, the

HRTEM studies revealed no evidence of interfacial reaction and confirmed the established epitaxial relationships. Figure 44 describes the electrical behavior of these films as a function of oxygen partial pressure. N-type electrical conductivity was observed in the NiO epilayers grown under lower pressures, which was turned into p-type in the films deposited under higher oxygen partial pressures. In addition, the electrical resistivity increased with the growth pressure. These observations were correlated to the nature of point defects in the NiO crystal. The formation of oxygen vacancies and metallic nickel at lower pressures, and excess oxygen and trivalent nickel at higher pressures was revealed by x-ray photo absorption spectroscopy (XPS).

## V. DME-GROWN EPITAXIAL LAYERS—LASER INDUCED PHYSICAL PROPERTIES

In recent studies,<sup>203,204</sup> laser irradiation has been reported to strongly alter the magnetic, optical, and electrical properties of a variety of solids. In particular, weak magnetism has been introduced in non-magnetic oxides by subjecting them to laser irradiation treatments. It has been suggested that the injection of vacancy and interstitial defects may explain the onset of these properties. Thus, laser processing of thin films represents an alternative approach for introducing new functionality into multifunctional heterostructures. Several recent results are reviewed below.

### A. BTO

As discussed<sup>90–92</sup> previously (Section IV B 2), BTO epitaxial thin films can be deposited on MgO/TiN/Si (100) using established DME concepts.<sup>4–8</sup> The question being probed here was whether it was possible to convert a simple ferroelectric materials into a single phase multiferroic (coupled ferroelectric and ferromagnetic behavior) by laser irradiation. BTO films were exposed to a series of laser

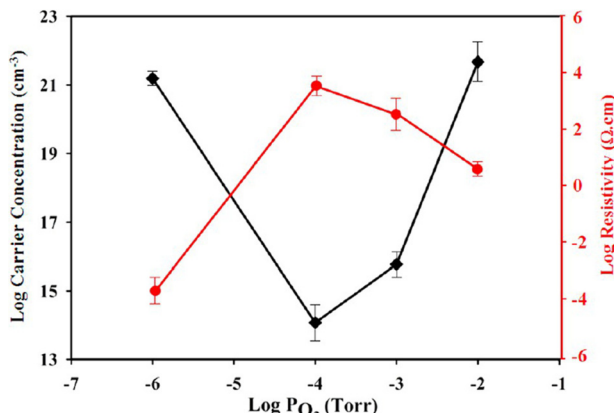


FIG. 44. Dependence of the NiO thin film electrical properties on the oxygen partial pressure. Reprinted with permission from Molaei *et al.*, Cryst. Growth Des. **13**, 5459–5465 (2013). Copyright 2013 American Chemical Society.

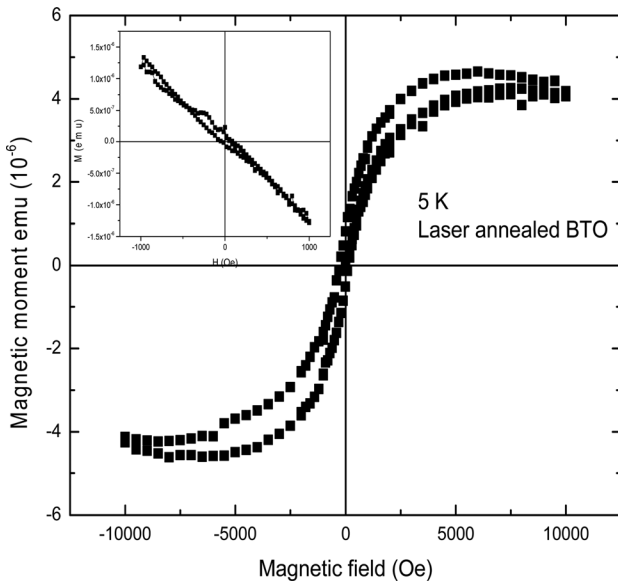


FIG. 45. In-plane isothermal (5 K) M-H measurements collected for laser annealed (20 pulses) BTO thin films showing ferromagnetic-like behavior. The inset shows the diamagnetic behavior of pristine BTO. The magnetic field is applied along  $\langle 100 \rangle$  direction of the sample. 10-pulse laser irradiated BTO shows no ferromagnetic behavior (not shown). Reprinted with permission from J. Appl. Phys. **116**, 094103 (2014). Copyright 2014 AIP Publishing LLC.

pulses from 1 to 20 pulses (intensity of  $0.236 \text{ J/cm}^2$ ). Isothermal (5 K) in-plane SQUID magnetometry measurements were then performed on as-deposited and laser annealed BTO films. The as-deposited BTO films showed diamagnetic behavior (see the inset of Fig. 45). However, the laser annealed films exposed to 20 pulses displayed weak ferromagnetic-like features, with clear saturation and a  $H_c$  of 200 Oe. In addition, it was found (data not shown) that the BTO films irradiated with 10 laser pulses did not show such ferromagnetic features. Concurrently, we tested the ferroelectric switching behavior of both laser annealed BTO films (irradiated with 10 and 20 laser pulses). Both showed high leakage currents and degraded ferroelectric characteristics compared with the as-deposited sample, high leakage current, almost certainly the introduction of oxygen vacancies upon laser irradiation. Survey scans of XPS spectra collected on as-deposited and laser annealed BTO films showed no indications of surface contamination. High resolution XPS spectra indicated that the Ti was in the +4 state. A clear shift (marked in red) of the oxygen peak upon laser irradiation (annealing) was observed. XRD patterns of BTO (002) reflection before and after laser irradiation revealed a slight peak broadening of the irradiated sample, on the order of 35% (from  $0.40^\circ$  to  $0.54^\circ$ ) with no peak shift. The MgO and TiN layers were found to be non-magnetic. The XRD and XPS data did not reveal any indication of secondary impurities before or after laser irradiation. All of this suggested that the injection of oxygen vacancies was the source of the magnetism and the cause of the enhanced leakage currents that adversely degraded the ferroelectric properties of the laser irradiated films. In addition, these findings suggest that the conversion of a ferroelectric material into a multiferroic with useful ferroelectric and ferromagnetic properties by

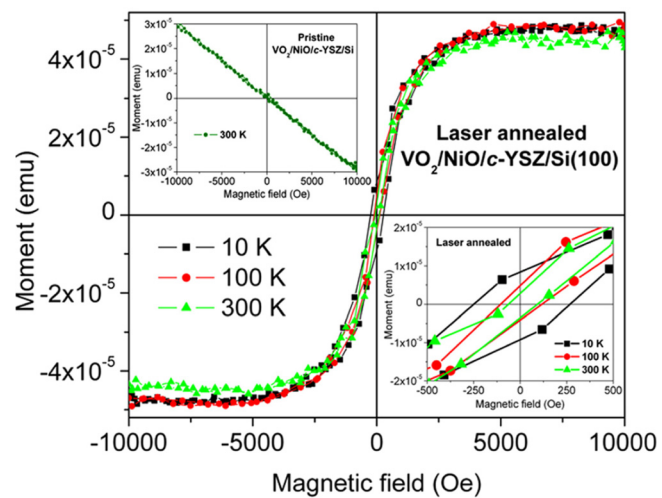


FIG. 46. The isothermal field dependence of magnetic moment curves of laser annealed  $\text{VO}_2/\text{NiO}/\text{c-YSZ}$  films deposited on Si(100) substrates measured at 10, 100, and 300 K. Plotted in the bottom inset are the low field M-H hysteresis loops between 6500 Oe deciphering clearly the coercivity. The diamagnetic contribution due to the Si substrate has been subtracted. The coercivity increases from  $\sim 60$  Oe at RT to 250 Oe at 10 K. The top inset plot shows the diamagnetic behavior of the pristine  $\text{VO}_2/\text{NiO}/\text{c-YSZ}/\text{Si}(100)$  sample. Reprinted with permission from Appl. Phys. Lett. **103**, 252109 (2013). Copyright 2013 AIP Publishing LLC.

laser irradiation will be very challenging and require the careful balancing of competing effects.

## B. $\text{VO}_2$

The physical properties of laser irradiated  $\text{VO}_2$  thin films have also been studied. Much like the BTO, it was found that the diamagnetic behavior of as-deposited sample changes to ferromagnetic behavior after laser irradiation<sup>188</sup> and that the concentration of charge carriers can be increased significantly. These findings might make  $\text{VO}_2$  an interesting candidate for spintronic applications where both semiconducting and ferromagnetic behavior are required. As is observed in Fig. 46, the as-deposited sample showed diamagnetic behavior which converted to ferromagnetic behavior after laser treatment. The inset displays the magnified M-H loops for the laser annealed sample, which clearly shows the presence of hysteresis that is characteristic of ferromagnetic behavior. It was shown that the crystalline structure, phase structure, and growth orientation of  $\text{VO}_2$  thin films remained unaltered after laser irradiation. In addition, the XPS survey scan showed similar elemental compositions and the absence of magnetic impurity elements in the as-deposited and laser irradiated samples. XPS was used to study the effect of laser irradiation on stoichiometry and defect structure of the samples. High resolution scans of the  $\text{V}(2\text{p}_{3/2})$  core level, for the as-deposited and annealed samples, are shown in Fig. 47. The results indicate that the concentration of the  $\text{V}^{4+}$  species decreased by  $>15\%$  and that of  $\text{V}^{3+}$  species increased after laser treatment. In fact, no  $\text{V}^{3+}$  cation was detected in the as-deposited sample. It is surmised that coupling of the high energy laser beam with the material drives oxygen out of  $\text{VO}_2$  thin films resulting in the formation of oxygen vacancies. The formation of oxygen vacancies is accompanied by

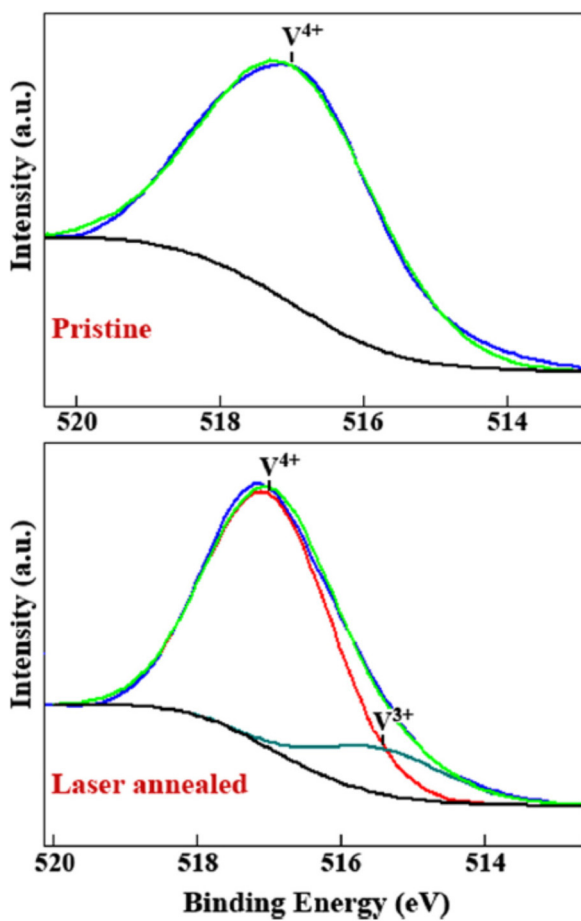


FIG. 47. V(2p<sub>3/2</sub>) core level binding energy in pristine and laser annealed samples. High resolution scans performed through V(2p<sub>3/2</sub>) core level, for the as-deposited and annealed samples. The results indicate that the concentration of the V<sup>4+</sup> species decreased by >15% and that of V<sup>3+</sup> species increased after laser treatment. In fact, no the V<sup>3+</sup> cation was detected in the pristine as-deposited sample. In the top Figure, the curve in blue represents the experimental spectrum, the curve in light green shows the simulated spectrum, and the difference is shown by the curve in black. In the bottom Figure, the curve in blue represents the experimental spectrum, the simulated V<sup>4+</sup> spectrum is shown in red, the simulated V<sup>3+</sup> spectrum is shown in thick green, the curve in light green shows the entire simulated spectrum, and the difference is shown by the curve in black. Reprinted with permission from Appl. Phys. Lett. **103**, 252109 (2013). Copyright 2013 AIP Publishing LLC.

the release of electrons to the lattice which is subsequently trapped by V<sup>4+</sup> cations resulting in the formation of V<sup>3+</sup> cations. Carrier concentration and resistance of the as-deposited and laser irradiated samples were measured by Hall technique. It was found that the carrier concentration increased from  $5 \times 10^{17}$  to  $7 \times 10^{19} \text{ cm}^{-3}$  and resistivity decreased from  $2.6 \times 10^1$  to  $1.8 \times 10^{-1} \Omega \text{ cm}$  after the laser treatment. All of this suggest that the change in magnetic behavior can be attributed to the formation of oxygen vacancies or V<sup>3+</sup> defects with unpaired electrons.

### C. TiO<sub>2</sub>

Among semiconducting materials, TiO<sub>2</sub> has attracted extensive interest due to its potential use in electronic and photonic devices. TiO<sub>2</sub> has been considered for use in photocatalysts,<sup>205</sup> solar cells,<sup>206</sup> gas sensors,<sup>207</sup> magnetic devices,<sup>208</sup>

UV detectors,<sup>209</sup> photoanodes,<sup>210</sup> and other applications. In addition, hydrophilic TiO<sub>2</sub> films have been considered for use as antifogging and self-cleaning surfaces.<sup>211</sup> C-YSZ buffer layer and rutile TiO<sub>2</sub> (100) epilayers were grown<sup>212</sup> on Si (001) substrates using PLD. Epitaxial growth of rutile TiO<sub>2</sub> with an a-axis texture was observed on the YSZ (001)/Si(001) platform. The 2-fold symmetry along the a-axis of rutile and existence of four energetically equivalent domains on the YSZ (001) plane resulted in the appearance of four strong  $\varphi$ -peaks for the rutile (110) reflection at angular intervals of 64.5° and angular separations of 32.25° from the YSZ (202) reflection. The presence of  $\varphi$ -peaks from Si (202) and YSZ (202) reflections at the same azimuthal angles confirms the epitaxial cube-on-cube growth of the cubic YSZ film on the silicon substrate.<sup>63,212</sup>

The wettability properties of the heterostructures were examined in ambient atmosphere by evaluating the behavior of deionized water droplets on the surfaces of the samples using optical photographs. Results<sup>212</sup> of the wettability test are displayed in the main panel of Fig. 48. Hydrophilic behavior was observed in the laser annealed samples, particularly in the sample irradiated at an energy density of  $0.32 \text{ J cm}^{-2}$ . In contrast, the as-deposited sample exhibits a hydrophobic surface, as shown in the inset of Fig. 48. It was found that the hydrophilicity of the samples increased with higher values of laser energy density. Based on the previous studies,<sup>171,195,213</sup> it is believed that laser irradiation leads to the formation of oxygen vacancies. Dissociative adsorption of water molecules at oxygen vacancies is the proposed mechanism for the observed hydrophilicity.<sup>213–215</sup> Because the concentration of oxygen vacancies increases with the laser

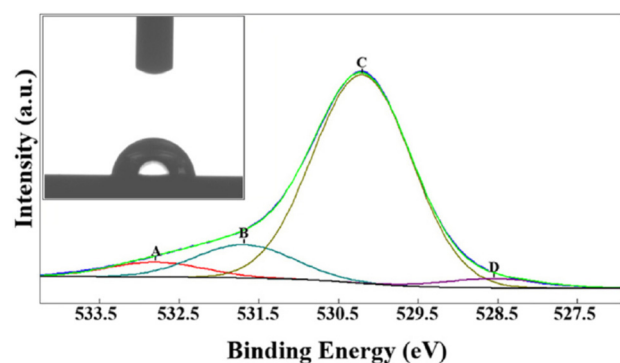


FIG. 48. XPS high resolution O(1s) core level binding energy for the as deposited sample. The wettability properties of the heterostructures were examined in ambient atmosphere by evaluating the behavior of deionized water droplets on the surfaces of the samples using optical photograph, as shown in the inset, the as-deposited sample exhibits a hydrophobic surface. The peaks A and B, which are located at binding energies of approximately 532.8 and 531.7 eV, are assigned to H<sub>2</sub>O and OH compounds that are attached to the surface defects. Peak C is located at the binding energy of about 530.2 eV; this peak is attributed to oxygen in the Ti-O-Ti bonding. Peak D with a binding energy of approximately 528.7 eV is indirectly assigned to titanium interstitials. In the main panel of this figure, the curve in blue represents the experimental spectrum. The four curves displayed in different colors peaked at A, B, C, and D represent the simulated spectra, assigned for four distinct defects. The curve in light green shows the entire simulated spectrum and the difference is shown by the curve in black. Reprinted with permission from J. Appl. Phys. **113**, 063706 (2013). Copyright 2013 AIP Publishing LLC.

energy, a more hydrophilic surface was obtained at higher laser energies. When an oxygen vacancy forms, two  $\text{Ti}^{4+}$  cations have to be converted to  $\text{Ti}^{3+}$  to preserve the charge neutrality. In other words,  $\text{Ti}^{4+}$  ions trap two electrons that are generated when an oxygen anion leaves the lattice. Formation of  $\text{Ti}^{3+}$  cations gives rise to a decrease in the band-gap energy.<sup>214</sup> The oxygen vacancies, as prerequisites for hydrophilicity, are formed through two different mechanisms. First, energy of the laser photons is absorbed by  $\text{TiO}_2$  via photoexcitation of the valence electrons to the conduction band giving rise to the formation of oxygen vacancies. Second, the surface temperature is increased due to the coupling of the high energy laser beam with the surface of the samples<sup>215</sup> leading to reduction of  $\text{TiO}_2$  and, hence, formation of oxygen vacancies. Then, a water molecule adsorbs on the defect sites and dissociates producing a new hydroxyl group, which is responsible for the highly hydrophilic surface.<sup>216</sup> It was found that the samples became hydrophobic after exposure to ambient atmosphere.

To shed light on this behavior, XPS measurements were obtained from the hydrophobic samples after exposure to ambient atmosphere. The data are presented in Fig. 48. The experimental spectra have been fit by considering four different curves, whose peak positions have been labeled as A, B, C, and D, corresponding to the energies of 532.8, 531.7, 530.2, and 528.7 eV, respectively. These were attributed to  $\text{H}_2\text{O}$ , OH, oxygen in Ti-O-Ti, and Ti interstitials, respectively. The peak amplitudes of the OH peak grew significantly under laser irradiation. They rose to 6.7%, 8.4%, 10.1%, and 12.6% for samples processed with laser energies of 0.16, 0.21, 0.28, and 0.32  $\text{J cm}^{-2}$ , respectively. The amplitude of the OH peak decreased significantly upon subsequent exposure to ambient atmosphere. This result suggests that surface oxygen vacancies are removed through absorption of oxygen from the atmosphere. Since the defect characteristics but not the surface roughness are altered by exposure of the samples to ambient atmosphere, we conclude that point defects can play an important role in altering the photochemical properties of the samples, i.e., the oxygen vacancies are responsible for introducing hydrophilic behavior. In this case, the laser-induced enhancement of hydrophilicity can be reversed by exposing the samples to ambient atmosphere, which remove surface oxygen vacancies through absorption of oxygen.

## VI. CONCLUSIONS AND OUTLOOK

This review highlights recent advances in the integration of multifunctional oxide and non-oxide materials onto silicon (100) substrates, the substrate workhorse of the semiconductor industry. An alternative thin film growth approach, referred to here as “domain matching epitaxy” (DME), has been presented which identifies approaches for minimizing lattice strain and unwanted defects across the lattice misfit scale. In particular, it addresses large misfit systems (7%–25%). This approach broadly expands the choice of materials that might someday be integrated into future CMOS circuitry to produce next generation “smart” devices. An important finding is that in terms of relaxing lattice

mismatch strain, it may actually be advantageous to adopt large lattice misfit systems. These systems have critical thicknesses of only a few monolayers. Thus, they initiate lattice strain relaxation at the earliest initial stages of film formation when barriers to misfit dislocation incorporation are low and strain relief can progress rapidly. Subsequent film growth occurs under strain relieved conditions making the control of defects, composition, and strain much more controllable than is possible under conventional lattice matching epitaxy.

In general, pulsed laser deposition (PLD) has been used to epitaxially grow these materials, although the concepts developed here can be extended to other deposition techniques, as well. Two promising new buffer layers, titanium nitride and yttria-stabilized zirconia (YSZ), have been identified as promising new platforms for the integration of functional oxides into silicon-based electronics. In the case of large lattice misfit systems, we have shown that the misfit strain can be relaxed completely at the growth temperature, and hence only residual thermal and defect strains remain upon cool down to ambient. Specifically, we have presented results on the ferroelectric-ferromagnetic heterostructures including BFO/LSMO, BTO/LSMO, PZT, and  $\text{Cr}_2\text{O}_3$ , and high permeability permalloy films, which are broadly relevant to magnetoelectric, ferroelectric memory, and spintronics applications. Notably, we have explored the novel physical properties of candidate topological insulators such as SSO and smart materials such as  $\text{VO}_2$  and  $\text{NiO}$  when they are integrated with silicon substrates. Furthermore, we have demonstrated the integration of transparent conductors such as  $\text{ZnO}$  and explored their optical and electrical properties. In general, the thin film heterostructures obtained through DME paradigm are of high crystalline quality and exhibit functional properties that are comparable to those grown on single-crystal lattice-matched oxide substrates.

This review also highlights the possibility of using laser irradiation to induce ferromagnetism and to tune electrical and optical properties in BTO,  $\text{TiO}_2$ , and  $\text{VO}_2$  single crystal thin films. Laser irradiation induced ferromagnetic properties seem to originate from the creation of oxygen vacancies. In the case of the BTO film, laser irradiation led to the degradation of the ferroelectric properties well before the onset of ferromagnetism, suggesting that the conversion of a ferroelectric material into a multiferroic with useful combinations of ferroelectric and ferromagnetic properties will be challenging.

The integration of functional thin films in single crystalline form on silicon opens exciting opportunities for the integration on Si of novel memory, sensing, electric and optical signal processing elements. Heterostructures of functional materials integrated with Si (100) computer chips open promising avenues for exciting new discoveries in the areas of multifunctional and smart solid state devices. The ability to grow these structures on silicon further provides a route for large-scale manufacturing, in contrast to oxide substrates that are typically  $<1 \text{ cm}^2$  in size. Not only are the DME-derived films nearly fully relaxed with reduced numbers of dislocations, a desired feature for microelectronics industry, but also the integration of these functional materials on silicon offers significant advantages in terms of heat dissipation

for potential power applications, since the thermal conductivity of silicon is an order of magnitude higher than that of typical oxide substrates. There is still much left to be done before the integration of multifunctional materials with silicon substrates can actually impact technology. But the potential is there. Some of these remaining barriers and challenges for finally realizing the integration of electronic, ferroelectric, optical, and magnetic properties into Si-based electronics are also evident and will be discussed now.

### A. Mastering 2-D layer growth

In order to achieve optimal performance from multifunctional heterostructures, it will be critical that one should be able to exercise complete control over the growth of the active layers to enable the fabrication of defect-engineered layers and compositionally sharp interfaces. DME concepts provide a paradigm for epitaxially growing large mismatch films under low strain conditions. But these films nucleate at multiple sites across the substrate surface, each slightly misaligned with the others. Upon film coalescence, the films result in slight tilt and rotations of neighboring regions. The resultant sub-grain boundaries can lead to unwelcomed sources of leakage currents, enhanced inter-diffusion, interface roughness, and premature device degradation. Processing approaches for minimizing this undesirable sub-grain morphology need to be identified, to determine the benefit of initial low temperature growth steps, post-nucleation high-temperature anneals, interrupted growth annealings, thermal cycling treatments, and surfactant aided growth techniques that potentially can enhance surface diffusion, suppress 3D growth modes, and promote sub-grain consolidation and growth. In general, a two-dimensional growth mode can be promoted by increasing the wetting during the initial stages of the growth. This is intimately related to the interfacial energy. Future work should focus on *in-situ* growth monitoring and computational studies to clarify all aspects of detailed growth mechanisms in these systems. The incorporation of *in-situ* synchrotron x-ray scattering methods and reflection high energy electron diffraction (RHEED) could be very useful in this context.

### B. Buffer layer reduction and interface optimization

In most cases, the growth of high quality heterostructures on Si substrates requires the use buffer layers to accommodate the misfit strain and to avoid unwanted reaction products, such as native silicon oxide, at the film-substrate interface. However, as noted previously in this review paper, the use of buffer layers generally leads to increased surface roughness (variation in film thickness  $\sim 1\%-1.5\%$ ) and diffuse interfaces ( $\sim 10 \text{ \AA}$ ) that can potentially disrupt the exchange interactions and interlayer coupling that are essential for establishing multifunction integration. Surface roughness also greatly complicates the implementation of interface-sensitive techniques such as x-ray reflectivity (XRR) and polarized neutron reflectivity (PNR). It is not uncommon for studies reported in the literature to note that the precise magnetic and ferroelectric nature of multiferroic oxide heterstructure interfaces are masked by interface and surface roughness induced by the underlying buffer layers.

For example, in the case of ferroelectric layers such as  $\text{BiFeO}_3$  and  $\text{BaTiO}_3$  deposited on buffered silicon substrates, it proved virtually impossible to determine the nature of ferroelectric domains due to the rougher surface. Similarly, the topological candidate thin film material  $\text{Sr}_3\text{SnO}$  was epitaxially integrated with the silicon substrates,<sup>158-160</sup> but it was not clear whether or not this material possessed topological properties, even after performing sensitive measurements and analysis. The most plausible reason was that the topological surface states are suppressed by the surface roughness. Hence, it would seem prudent to minimize the number and overall thickness of buffer layers and incorporate the use of optimal thin film deposition techniques that will result in relatively smoother layers with atomically abrupt interfaces. The surface roughness and thickness variations can be reduced by translating and rotating the substrate during the thin film deposition process.

In Sections IVB and IVC, there have been many examples where the magnetic properties were strongly influenced by the nature of the intervening interfaces. For example, when bilayers of two ferromagnetic heterostructures (LSMO/SRO) were integrated<sup>145,147</sup> on silicon, anomalous changes in the magnetic properties (complete up-shift in M-H loop) were reported. These new properties were argued to be arising from orbital reconstruction at the interface or spin pinning of ferroelectric layer, however, without clear experimental evidence. Magnetic and ferroelectric characterization of multiple thin film interfaces is generally a challenging task when using only bulk measurements such as SQUID. Studies are needed that can begin to resolve the local interface and bulk spin structures by employing local and element specific techniques such as PNR, x-ray magnetic circular dichroism, and x-ray absorption and photoemission spectroscopic measurements. Such studies should lead to an improved understanding of the role that the interface plays in determining the electronic and magnetic properties, the band offsets, and the presence or absence of interface strained states of the resulting heterostructures.

### C. Defect control and reliability issues

The first prototype devices<sup>73,80,81,90,101</sup> fabricated using DME-grown electrical and ferroelectric layers prepared on silicon substrates show promising trends in resistive switching and ferroelectric functionality for future non-volatile memory applications. However, they suffer from reliability issues which can be a major challenge even when the ferroelectric layers are deposited on lattice matching substrates such as  $\text{SrTiO}_3$ . Many of the ferroelectric layers reported<sup>72,90</sup> in the literature show slanted and unsaturated hysteresis (as opposed to square-shaped) behavior in macroscopic polarization measurements due to intrinsic defects and substrate clamping effects. Furthermore, these devices break down after a few 10's of cycles and are found to be operational only below room temperatures. This appears to be associated with the large leakage currents generated due to the presence of pinholes and sub-grain boundaries in the films. Even in films where the lattice-strain is relaxed at the growth temperature, the films will still show an un-relaxed strain  $\sim 0.2\%-0.5\%$  that is due to growth-induced defects and thermal strain

arising from the large differences in the thermal expansion coefficient between the overlayers and Si substrates. Thermal mismatch strain can be reduced to some extent by slow cooling ( $\sim 2^\circ\text{C}/\text{min}$ ) the layers after the growth. But alternative approaches need to be identified that can actively counteract small amounts of stress that build up in these structures over time and operation.

Continuous monitoring of the stress state of the films is critical. Unfortunately, in many of the electron and x-ray diffraction patterns collected from the heterostructures, the diffraction spots of the different (active and buffer) layers overlap and do not allow estimating the in-plane strain states. It is important to measure the strain states of all the layers both in-plane and out of plane to clarify the precise origin of the resulting novel properties. Thus, other techniques capable of measuring the interface strain and structure such as Z-contrast scanning transmission electron microscopy (STEM-Z) and electron energy loss spectroscopy (EELS) mapping need to be more universally employed to better assess the influence of strain on defect formation and interface-related chemical and physical properties of the films. Using STEM-EELS study, one can perform atomic-resolution mapping<sup>217–221</sup> to explore the local structure and chemistry (valence state) of interface layers and estimate the displacement of atoms and associated strain and disorder across various interfaces. Furthermore, approaches are needed to minimize or reduce the formation of columnar structures and low angle grain boundaries that arise due to symmetry mismatch and minimize or lower the dangling bonds and trap states that collect at the buffer layer/active layer interfaces, which are detrimental for device performance.

In addition to being of fundamental interest, the engineering of defect populations in these systems is of profound technological importance since the properties of oxide thin films often depend strongly on defect concentrations such as oxygen vacancies and cation non-stoichiometry. These defects, which can be controlled by laser and substrate parameters, strongly affect the lattice parameters and interface structures of the system, which in turn alter their physical properties. Therefore, it is of utmost importance to identify the origins of critical defects in these systems and better understand the underlying formation mechanisms. In this context, studies that combine local probes such as STEM-Z imaging with theoretical first-principles calculations could be very valuable. Future work should also attempt to quantify the strain and charge transfer that takes place across the interfaces and the effect that this has on coupling effects between the respective layers. Similarly, elucidating the role of defects on the bond lengths, bond angles, and octahedral rotations that occur in these oxide heterostructures and determining how they influence the resulting properties would be important. For the oxides, a better understanding of post-deposition thermal anneals under various atmospheres and temperatures is also needed.

## D. Innovative heterostructures

In reality, we have only begun to explore the many material combinations that could provide for new functionality. Future researchers can focus their efforts on integrating more

advanced heterostructures and superlattices onto Si, including, for example, heterostructures containing two-dimensional materials such as topological insulators, graphene, diamond, and boron nitride (BN). Another important near-term opportunity is the integration of thin film heterostructures in less conventional crystallographic directions. At present, as discussed in this review, controlled integration of [001]-oriented heterostructures on silicon is becoming increasingly routine. Developing the expertise needed to move to lower symmetry (non-cubic or hexagonal) crystal structures and templates also needs to be explored as a potential means of expanding the parameter space well beyond current capabilities. However, each system will pose its own unique materials challenges in terms of surface reconstruction, dislocation dynamics, etc. The possibilities are enormous. Developing a predictive modeling capability that can guide these studies will be critical.

## ACKNOWLEDGMENTS

S.R.S. acknowledges National Academy of Science (NAS), USA for awarding the NRC postdoctoral research associate fellowship. The authors are pleased to acknowledge the support of the Army Research Office under Grant No. W911NF-04-D-0003. Also, the authors acknowledge the use of the Analytical Instrumentation Facility (AIF) at North Carolina State University, which is supported by the State of North Carolina and the National Science Foundation.

- <sup>1</sup>D. Sando, A. Barthelemy, and M. Bibes, *J. Phys.: Condens. Matter* **26**, 473201 (2014).
- <sup>2</sup>F. Matsukura, Y. Tokura, and H. Ohno, *Nat. Nanotechnol.* **10**, 209 (2015).
- <sup>3</sup>J. J. Yang, D. B. Strukov, and D. R. Stewart, *Nat. Nanotechnol.* **8**, 13 (2013).
- <sup>4</sup>J. Narayan, P. Tiwari, X. Chen, R. Chowdhury, and T. Zheleva, *Appl. Phys. Lett.* **61**, 1290–1292 (1992).
- <sup>5</sup>J. Narayan, U.S. patent 5,406,123 (1995); T. Zheleva, K. Jagannadham, and J. Narayan, *J. Appl. Phys.* **75**, 860 (1994).
- <sup>6</sup>J. Narayan, “Domain epitaxy for thin film growth,” U.S. patent 6,955,985 (18 October 2005).
- <sup>7</sup>J. Narayan, *Acta Mater.* **61**, 2703–2724 (2013).
- <sup>8</sup>J. Narayan and B. C. Larson, *J. Appl. Phys.* **93**, 278–283 (2003).
- <sup>9</sup>R. Hull and E. A. Stach, *Curr. Opin. Solid State Mater. Sci.* **1**, 21 (1996).
- <sup>10</sup>F. C. Frank and J. H. van der Merwe, Proc. R. Soc. London, Ser. A **198**, 205–216 (1949).
- <sup>11</sup>F. C. Frank and J. H. van der Merwe, Proc. R. Soc. London, Ser. A **200**, 125–134 (1949).
- <sup>12</sup>J. W. Matthews and A. E. Bakeslee, *J. Cryst. Growth* **27**, 118–125 (1974).
- <sup>13</sup>A. J. Purdes, B. F. T. Bolker, J. D. Bucci, and T. C. Tisone, *J. Vac. Sci. Technol.* **4**, 98 (1977).
- <sup>14</sup>R. People and J. C. Bean, *Appl. Phys. Lett.* **47**, 322 (1985).
- <sup>15</sup>R. Hull and J. C. Bean, *J. Vac. Sci. Technol., A* **7**, 2580 (1989).
- <sup>16</sup>J. Narayan and S. Sharan, *Mater. Sci. Eng., B* **10**, 261 (1991).
- <sup>17</sup>S. Sharan and J. Narayan, *J. Appl. Phys.* **66**, 2376 (1989).
- <sup>18</sup>K. Jagannadham and J. Narayan, *Mater. Sci. Eng., A* **113**, 65 (1989).
- <sup>19</sup>H. A. Lu, L. A. Wills, and B. W. Wessels, *Appl. Phys. Lett.* **64**, 2973 (1994).
- <sup>20</sup>V. Srikant, E. J. Tarsa, D. R. Clarke, and J. S. Speck, *J. Appl. Phys.* **77**, 1517 (1995).
- <sup>21</sup>K. Nashimoto, D. K. Fork, and T. H. Geballe, *Appl. Phys. Lett.* **60**, 1199 (1992).
- <sup>22</sup>E. J. Tarsa, M. De Graaf, D. R. Clarke, A. C. Gossard, and J. S. Speck, *J. Appl. Phys.* **73**, 3276 (1993).
- <sup>23</sup>B. Heying, X. H. Wu, S. Keller, Y. Li, D. Kapolnek, B. Keller, S. P. DenBaars, and J. S. Speck, *Appl. Phys. Lett.* **68**, 643 (1996).
- <sup>24</sup>R. F. Davis, T. W. Weeks, Jr., M. D. Bremser, S. Tanaka, R. S. Kern, Z. Sitar, K. S. Ailey, W. G. Perry, and C. Wang, *MRS Proc.* **395**, 3 (1995).

- <sup>25</sup>D. Kapolnek, X. H. Wu, B. Heying, S. Keller, B. Keller, U. K. Mishra, S. P. DenBaars, and J. S. Speck, *Appl. Phys. Lett.* **67**, 1541 (1995).
- <sup>26</sup>M. Kasuga and M. Mochizuki, *J. Cryst. Growth* **54**, 185 (1981).
- <sup>27</sup>V. Srikan, V. Sergio, and D. R. Clarke, *J. Am. Ceram. Soc.* **78**, 1931 (1995).
- <sup>28</sup>D. K. Fork, F. Armani-Leplingrad, J. J. Kingston, and G. B. Anderson, in *Thin Film for Integrated Optics*, edited by B. W. Wessels and D. M. Walba (Mater. Res. Soc. Symp. Proc., Pittsburgh, PA, 1995), p. 189.
- <sup>29</sup>J. Chakhalian, J. W. Freeland, A. J. Millis, C. Panagopoulos, and J. M. Rondinelli, *Rev. Mod. Phys.* **86**, 1189 (2014).
- <sup>30</sup>J. T. Heron, D. G. Schlom, and R. Ramesh, *Appl. Phys. Rev.* **1**, 021303 (2014).
- <sup>31</sup>S. H. Baek and C. B. Eom, *Acta Mater.* **61**, 2734 (2013).
- <sup>32</sup>C. L. Chua, W. Y. Hsu, C. H. Lin, G. Christenson, and Y. H. Lo, *Appl. Phys. Lett.* **64**, 3640 (1994).
- <sup>33</sup>Z. Yang, F. Guarin, I. W. Tao, W. I. Wang, and S. S. Iyer, *J. Vac. Sci. Technol.*, B **13**, 789 (1995).
- <sup>34</sup>R. A. McKee, F. J. Walker, and M. F. Chisholm, *Phys. Rev. Lett.* **81**, 3014 (1998).
- <sup>35</sup>C. Dubourdieu, J. Bruley, T. M. Arruda, A. Posadas, J. Jordan-Sweet, M. M. Frank, E. Cartier, D. J. Frank, S. V. Kalinin, A. A. Demkov, and V. Narayanan, *Nat. Nanotechnol.* **8**, 748 (2013).
- <sup>36</sup>S. H. Baek, J. Park, D. M. Kim, V. A. Aksyuk, R. R. Das, S. D. Bu, D. A. Felker, J. Lettieri, V. Vaithyanathan, S. S. N. Bharadwaja, N. Bassiri-Gharb, Y. B. Chen, H. P. Sun, C. M. Folkman, H. W. Jang, D. J. Kreft, S. K. Streiffer, R. Ramesh, X. Q. Pan, S. Trolier-McKinstry, D. G. Schlom, M. S. Rzchowski, R. H. Blick, and C. B. Eom, *Science* **334**, 958 (2011).
- <sup>37</sup>J. W. Park, D. F. Bogorin, C. Cen, D. A. Felker, Y. Zhang, C. T. Nelson, C. W. Bark, C. M. Folkman, X. Q. Pan, M. S. Rzchowski, J. Levy, and C. B. Eom, *Nat. Commun.* **1**, 94 (2010).
- <sup>38</sup>Y. H. Chu, Q. Zhan, C.-H. Yang, M. P. Cruz, L. W. Martin, T. Zhao, P. Yu, R. Ramesh, P. T. Joseph, I. N. Lin, W. Tian, and D. G. Schlom, *Appl. Phys. Lett.* **92**, 102909 (2008).
- <sup>39</sup>H. Funakubo, M. Dekkers, A. Sambri, S. Gariglio, I. Shklyarevskiy, and G. Rijnders, *MRS Bull.* **37**, 1030 (2012).
- <sup>40</sup>R. Ramesh, S. Aggarwal, and O. Auciello, *Mater. Sci. Eng.* **32**, 191–236 (2001).
- <sup>41</sup>K. Sreenivas, I. Reaney, T. Maeder, N. Setter, C. Jagadish, and R. G. Elliman, *J. Appl. Phys.* **75**, 232 (1994).
- <sup>42</sup>A. Z. Simões, M. A. Ramirez, C. S. Riccardi, E. Longo, and J. A. Varela, *Mater. Lett.* **60**, 2020–2023 (2006).
- <sup>43</sup>J. Deng, W. Zhu, O. K. Fan, and X. Yao, *Sens. Actuators* **77**, 416–420 (2001).
- <sup>44</sup>S. Aggarwal and R. Ramesh, U.S. patent 6,194,754 B1 (February 2001).
- <sup>45</sup>S. Aggarwal, A. M. Dhote, and R. Ramesh, U.S. patent 6,274,388 B1 (August 2001).
- <sup>46</sup>R. Ramesh and D. G. Schlom, U.S. patent 2003/0062553 A1 (April 2003).
- <sup>47</sup>L. Dong, J. Schnitker, R. W. Smith, and D. J. Srolovitz, *J. Appl. Phys.* **83**, 217 (1998).
- <sup>48</sup>L. B. Freund, *MRS Bull.* **17**, 52 (1992).
- <sup>49</sup>V. I. Vdovin, *Phys. Status Solidi A* **171**, 239 (1999).
- <sup>50</sup>F. K. LeGoues, M. C. Reuter, J. Tersoff, M. Hammar, and R. M. Tromp, *Phys. Rev. Lett.* **73**, 300 (1994).
- <sup>51</sup>P. Pant, J. D. Budai, and J. Narayan, *Acta Mater.* **58**, 1097 (2010).
- <sup>52</sup>J. M. Chauveau, P. Venneguès, M. Laugt, C. Deparis, J. Zuniga-Perez, and C. Morhain, *J. Appl. Phys.* **104**, 073535 (2008).
- <sup>53</sup>P. Pant, J. D. Budai, R. Aggarwal, R. J. Narayan, and J. Narayan, *Acta Mater.* **57**, 4426 (2009).
- <sup>54</sup>S. J. Pennycook, H. Zhou, M. F. Chisholm, A. Y. Borisevich, M. Varela, J. Gazquez, T. J. Pennycook, and J. Narayan, *Acta Mater.* **61**, 2725 (2013).
- <sup>55</sup>J. W. Lee, S. K. Han, S.-K. Hong, J. Y. Lee, and T. Yao, *J. Cryst. Growth* **310**, 4102 (2008).
- <sup>56</sup>C. M. Wang, L. V. Saraf, and Y. Qiang, *Thin Solid Films* **516**, 8337 (2008).
- <sup>57</sup>H. Zhou, M. F. Chisholm, P. Pant, H. J. Chang, J. Gazquez, S. J. Pennycook, and J. Narayan, *Appl. Phys. Lett.* **97**, 121914 (2010).
- <sup>58</sup>V. Nagarajan, C. L. Jia, H. Kohlstedt, R. Waser, I. B. Misirlioglu, S. P. Alpay, and R. Ramesh, *Appl. Phys. Lett.* **86**, 192910 (2005).
- <sup>59</sup>H. N. Al-Shareef, B. A. Tuttle, W. L. Warren, T. J. Headley, D. Dimos, J. A. Voigt, and R. D. Nasby, *J. Appl. Phys.* **79**, 1013 (1996).
- <sup>60</sup>K. H. Lee, K. B. Lee, and S. B. Desu, *J. Korean Phys. Soc.* **42**, 538–542 (2003).
- <sup>61</sup>T. Watanabe, K. Ito, S. Tsukimoto, Y. Ushida, M. Moriyama, N. Shibata, and M. Murakami, *Mater. Trans.* **46**, 1975–1978 (2005).
- <sup>62</sup>U. Kumar, K. R. Summerfelt, S. R. Moise, S. Ted, and M. K. Jain, U.S. patent 8,778,700 B2 (15 July 2014).
- <sup>63</sup>R. Molaei, M. R. Bayati, and J. Narayan, *J. Mater. Res.* **27**, 3103–3109 (2012).
- <sup>64</sup>J. F. Scott, *Ferroelectric Memories* (Springer-Verlag, Berlin, 2000).
- <sup>65</sup>J. Hoffman, X. Pan, J. W. Reiner, F. J. Walker, J. P. Han, C. H. Ahn, and T. P. Ma, *Adv. Mater.* **22**, 2957–2961 (2010).
- <sup>66</sup>T. Hidaka, T. Mayurama, M. Saitoh, N. Mikoshiba, M. Shimizu, T. Shiosaki, L. A. Wills, R. Hiskes, S. A. Dicarolis, and J. Amano, *Appl. Phys. Lett.* **68**, 2358 (1996).
- <sup>67</sup>T. Tybell, P. Paruch, T. Giannachi, and J. M. Triscone, *Phys. Rev. Lett.* **89**, 097601 (2002).
- <sup>68</sup>S. Salahuddin and S. Datta, *Nano Lett.* **8**, 405 (2008).
- <sup>69</sup>H. J. A. Molegraaf, J. Hoffman, C. A. F. Vaz, S. Gariglio, D. van der Marel, C. H. Ahn, and J.-M. Triscone, *Adv. Mater.* **21**, 3470 (2009).
- <sup>70</sup>P. M. Leufke, R. Kruk, R. A. Brand, and H. Hahn, *Phys. Rev. B* **87**, 094416 (2013).
- <sup>71</sup>Z. Li, J. Hu, L. Shu, Y. Gao, Y. Shen, Y. Lin, and C. W. Nan, *J. Appl. Phys.* **111**, 033918 (2012).
- <sup>72</sup>C. Wang, D. E. Laughlin, and M. H. Kryder, *Appl. Phys. Lett.* **90**, 172903 (2007).
- <sup>73</sup>C. Wang and M. H. Kryder, *J. Electron. Mater.* **38**, 1921 (2009).
- <sup>74</sup>R. Ramesh and N. A. Spaldin, *Nat. Mater.* **6**, 21 (2007).
- <sup>75</sup>W. Eerenstein, N. D. Mathur, and J. F. Scott, *Nature* **442**, 759–765 (2006).
- <sup>76</sup>S. Fusil, V. Garcia, A. Barthélémy, and M. Bibes, *Annu. Rev. Mater. Res.* **44**, 91–116 (2014).
- <sup>77</sup>Y.-H. Chu, L. W. Martin, M. B. Holcomb, M. Gajek, S.-J. Han, Q. He, N. Balke, C.-H. Yang, D. Lee, W. Hu, Q. Zhan, P.-L. Yang, A. Fraile-Rodríguez, A. Scholl, S. X. Wang, and R. Ramesh, *Nat. Mater.* **7**, 478 (2008).
- <sup>78</sup>D. Lebeugle, A. Mougin, M. Viret, D. Colson, and L. Ranno, *Phys. Rev. Lett.* **103**, 257601 (2009).
- <sup>79</sup>S. M. Wu, S. A. Cybart, D. Yi, J. M. Parker, R. Ramesh, and R. C. Dynes, *Phys. Rev. Lett.* **110**, 067202 (2013).
- <sup>80</sup>S. S. Rao, J. T. Prater, F. Wu, C. T. Shelton, J.-P. Maria, and J. Narayan, *Nano Lett.* **13**, 5814 (2013).
- <sup>81</sup>S. R. Singamaneni, J. T. Prater, S. Nori, D. Kumar, B. Lee, V. Misra, and J. Narayan, *J. Appl. Phys.* **117**, 17D908 (2015).
- <sup>82</sup>J. Wang, H. Zheng, Z. Ma, S. Prasertchoung, M. Wuttig, R. Droopad, J. Yu, K. Eisenbeiser, and R. Ramesh, *Appl. Phys. Lett.* **85**, 2574 (2004).
- <sup>83</sup>P. Yu, J.-S. Lee, S. Okamoto, M. D. Rossell, M. Huijben, C.-H. Yang, Q. He, J. X. Zhang, S. Y. Yang, M. J. Lee, Q. M. Ramasse, R. Erni, Y.-H. Chu, D. A. Arena, C.-C. Kao, L. W. Martin, and R. Ramesh, *Phys. Rev. Lett.* **105**, 027201 (2010).
- <sup>84</sup>D. A. Tenne, P. Turner, J. D. Schmidt, M. Biegalski, Y. L. Li, L. Q. Chen, A. Soukiasian, S. Trolier-McKinstry, D. G. Schlom, X. X. Xi, D. D. Fong, P. H. Fuoss, J. A. Eastman, G. B. Stephenson, C. Thompson, and S. K. Streiffer, *Phys. Rev. Lett.* **103**, 177601 (2009).
- <sup>85</sup>C. Li, Z. Chen, D. Cui, Y. Zhou, H. Lu, C. Dong, F. Wu, and H. Chen, *J. Appl. Phys.* **86**, 4555 (1999).
- <sup>86</sup>T. Shimizu, D. Suwama, H. Taniguchi, T. Taniyama, and M. Itoh, *J. Phys.: Condens. Matter* **25**, 132001 (2013).
- <sup>87</sup>M. El Marssi, F. Le Marrec, I. A. Lukyanchuk, and M. G. Karkut, *J. Appl. Phys.* **94**, 3307 (2003).
- <sup>88</sup>D. L. Kaiser, M. D. Vaudin, L. D. Rotter, Z. L. Wang, J. P. Cline, C. S. Hwang, R. B. Marinenco, and J. G. Gillen, *Appl. Phys. Lett.* **66**, 2801 (1995).
- <sup>89</sup>K. J. Choi, M. Biegalski, Y. L. Li, A. Sharan, J. Schubert, R. Uecker, P. Reiche, Y. B. Chen, X. Q. Pan, V. Gopalan, L.-Q. Chen, D. G. Schlom, and C. B. Eom, *Science* **306**, 1005 (2004).
- <sup>90</sup>S. R. Singamaneni, S. Punugupati, J. T. Prater, F. Hunte, and J. Narayan, *J. Appl. Phys.* **116**, 094103 (2014).
- <sup>91</sup>S. R. Singamaneni, W. Fan, J. T. Prater, and J. Narayan, *J. Appl. Phys.* **116**, 224104 (2014).
- <sup>92</sup>S. R. Singamaneni, J. T. Prater, and J. Narayan, *Emerging Mater. Res.* **4**, 50 (2015).
- <sup>93</sup>L. Huang, Z. Chen, J. D. Wilson, S. Banerjee, R. D. Robinson, I. P. Herman, R. Laibowitz, and S. O'Brien, *J. Appl. Phys.* **100**, 034316 (2006).
- <sup>94</sup>R. Thomas, V. K. Varadan, S. Komarneni, and D. C. Dube, *J. Appl. Phys.* **90**, 1480 (2001).
- <sup>95</sup>B. Jaffe, W. R. Cook, and H. Jaffe, *Piezoelectric Ceramics* (Academic, New York, 1971), p. 78.

- <sup>96</sup>A. P. Chen, F. Khatkhatay, W. Zhang, C. Jacob, L. Jiao, and H. Wang, *J. Appl. Phys.* **114**, 124101 (2013).
- <sup>97</sup>G. Robert, D. Damjanovic, and N. Setter, *Appl. Phys. Lett.* **77**, 4413 (2000).
- <sup>98</sup>M. K. Lee, T. K. Nath, C. B. Eom, M. C. Smoak, and F. Tsui, *Appl. Phys. Lett.* **77**, 3547 (2000).
- <sup>99</sup>H. Lu, T. A. George, Y. Wang, I. Ketsman, J. D. Burton, C.-W. Bark, S. Ryu, D. J. Kim, J. Wang, C. Binek, P. A. Dowben, A. Sokolov, C.-B. Eom, E. Y. Tsymbal, and A. Gruverman, *Appl. Phys. Lett.* **100**, 232904 (2012).
- <sup>100</sup>Y.-L. Zhao, Y. Sun, L.-Q. Pan, K.-S. Li, and D.-B. Yu, *Appl. Phys. Lett.* **102**, 042404 (2013).
- <sup>101</sup>C. Wang and M. H. Kryder, *J. Phys. D: Appl. Phys.* **41**, 245301 (2008).
- <sup>102</sup>M. Scigaj, N. Dix, I. Fina, R. Bachelet, B. Warot-Fonrose, J. Fontcuberta, and F. Sanchez, *Appl. Phys. Lett.* **102**, 112905 (2013).
- <sup>103</sup>T. Nagamiya, K. Yosida, and R. Kubo, *Adv. Phys.* **4**, 1 (1955).
- <sup>104</sup>T. R. McGuire, E. J. Scott, and F. H. Grannis, *Phys. Rev.* **102**(4), 1000 (1956).
- <sup>105</sup>I. E. Dzyaloshinskii, *J. Exp. Theor. Phys. (U.S.S.R.)* **37**, 881 (1959)[*Sov. Phys. -JETP* **10**, 628 (1960)].
- <sup>106</sup>D. N. Astrov, *J. Exp. Theor. Phys. (U.S.S.R.)* **38**, 984 (1960)[*Sov. Phys. -JETP* **11**, 708 (1960)].
- <sup>107</sup>A. Iyama and T. Kimura, *Phys. Rev. B* **87**, 180408(R) (2013).
- <sup>108</sup>J. Wang, A. Gupta, and T. M. Klein, *Thin Solid Films* **516**, 7366 (2008).
- <sup>109</sup>S.-Y. Jeong, J.-B. Lee, H. Na, and T.-Y. Seong, *Thin Solid Films* **518**, 4813 (2010).
- <sup>110</sup>H. Mandar, T. Uustare, J. Aarik, A. Tarre, and A. Rosenthal, *Thin Solid Films* **515**, 4570 (2007).
- <sup>111</sup>T. Kosaka, S. Suzuki, M. Saito, Y. Waseda, E. Matsubara, K. Sadamori, and E. Aoyagi, *Thin Solid Films* **289**, 74 (1996).
- <sup>112</sup>M. Shima, T. Tepper, and C. A. Ross, *J. Appl. Phys.* **91**, 7920 (2002).
- <sup>113</sup>A. Ghosh, K. Dey, S. Sabyasachi, A. Karmakar, S. Majumdar, and S. Giri, *Appl. Phys. Lett.* **103**, 052412 (2013).
- <sup>114</sup>S. Punugupati, J. Narayan, and F. Hunte, *Appl. Phys. Lett.* **105**, 132401 (2014).
- <sup>115</sup>S. S. P. Parkin, M. Hayashi, and L. Thomas, *Science* **320**, 190 (2008).
- <sup>116</sup>J. McCord and J. Westwood, *IEEE Trans. Magn.* **37**, 1755 (2001).
- <sup>117</sup>H. Aurich, A. Baumgartner, F. Freitag, A. Eichler, J. Trbovic, and C. Schönenberger, *Appl. Phys. Lett.* **97**, 153116 (2010).
- <sup>118</sup>V. Skumryev, V. Laukhin, I. Fina, X. Martí, F. Sa'nchez, M. Gospodinov, and J. Fontcuberta, *Phys. Rev. Lett.* **106**, 057206 (2011).
- <sup>119</sup>G. Raatz and J. Woltersdorf, *Phys. Status Solidi A* **113**, 131–141 (1989).
- <sup>120</sup>J. P. McCaffrey, E. B. Svedberg, J. R. Phillips, and L. D. Madsen, *J. Cryst. Growth* **200**, 498–504 (1999).
- <sup>121</sup>E. B. Svedberg, P. Sandstrom, J. Sundgren, J. E. Greene, and L. D. Madsen, *Surf. Sci.* **429**, 206–216 (1999).
- <sup>122</sup>F. Reniers, M. P. Declancke, A. Asskali, V. Rooryck, and O. VanSinay, *Appl. Surf. Sci.* **92**, 35–42 (1996).
- <sup>123</sup>H. Qiu, H. Nakai, M. Hashimoto, G. Safran, M. Adamik, P. B. Barna *et al.*, *J. Vac. Sci. Technol., A* **12**, 2855 (1994).
- <sup>124</sup>R. A. Lukaszew, Z. D. Zhang, V. Stoica, and R. Clarke, *Appl. Surf. Sci.* **219**, 74 (2003).
- <sup>125</sup>S. S. Rao, J. T. Prater, F. Wu, S. Nori, D. Kumar, and J. Narayan, *Curr. Opin. Solid State Mater. Sci.* **18**, 1–5 (2014).
- <sup>126</sup>S. S. Rao, J. T. Prater, F. Wu, S. Nori, D. Kumar, L. Yue, S.-H. Liou, and J. Narayan, *Curr. Opin. Solid State Mater. Sci.* **18**, 140–146 (2014).
- <sup>127</sup>Y. Sun, M. B. Salamon, K. Garnier, and R. S. Averback, *Phys. Rev. Lett.* **91**, 167206 (2003).
- <sup>128</sup>T. Tanaka, M. Ohtake, F. Kirino, and M. Futamoto, *IEEE Trans. Magn.* **46**, 345 (2010);**45**, 2515 (2009).
- <sup>129</sup>T. Trunk, M. Redjali, A. Ka'key, M. F. Ruane, and F. B. Humphrey, *J. Appl. Phys.* **89**, 7606 (2001).
- <sup>130</sup>Y. C. Chen, D.-S. Hung, Y.-D. Yao, S.-F. Lee, H.-P. Ji, and C. Yu, *J. Appl. Phys.* **101**, 09C104 (2007).
- <sup>131</sup>F. Wu, S. S. Rao, J. T. Prater, Y. T. Zhu, and J. Narayan, *Curr. Opin. Solid State Mater. Sci.* **18**, 263–268 (2014).
- <sup>132</sup>U. Luders, A. Barthélémy, M. Bibes, K. Bouzehouane, S. Fusil, E. Jacquet, J. P. Contour, J. F. Bobo, J. Fontcuberta, and A. Fert, *Adv. Mater.* **18**, 1733 (2006).
- <sup>133</sup>V. G. Harris, A. Geilera, Y. Chen, S. D. Yoon, M. Wu, A. Yang, Z. Chen, P. Hea, P. V. Parimia, X. Zuo, C. E. Patton, M. Abe, O. Acher, and C. Vittoria, *J. Magn. Magn. Mater.* **321**, 2035 (2009).
- <sup>134</sup>A. V. Ramos, M. J. Guittet, J. B. Moussy, R. Mattana, C. Deranlot, F. Petroff, and C. Gatel, *Appl. Phys. Lett.* **91**, 122107 (2007).
- <sup>135</sup>F. Sa'nchez, R. Bachelet, P. de Coux, B. Warot-Fonrose, V. Skumryev, L. Tarnawska, P. Zaumseil, T. Schroeder, and J. Fontcuberta, *Appl. Phys. Lett.* **99**, 211910 (2011).
- <sup>136</sup>X. Ke *et al.*, *Appl. Phys. Lett.* **84**, 5458 (2004).
- <sup>137</sup>X. Ke, L. J. Belenkyl, C. B. Eom, and M. S. Rzchowski, *J. Appl. Phys.* **97**, 10K115 (2005).
- <sup>138</sup>A. Solignac, R. Guerrero, P. Gogol, T. Maroutian, F. Ott, L. Largeau, Ph. Lecoeur, and M. Pannetier-Lecoeur, *Phys. Rev. Lett.* **109**, 027201 (2012).
- <sup>139</sup>X. Ke, L. J. Belenkyl, V. Lauter, H. Ambaye, C. W. Bark, C. B. Eom, and M. S. Rzchowski, *Phys. Rev. Lett.* **110**, 237201 (2013).
- <sup>140</sup>M. Ziese, I. Vrejoiu, E. Pippel, P. Esquinazi, D. Hesse, C. Etz, J. Henk, A. Ernst, I. V. Maznichenko, W. Hergert, and I. Mertig, *Phys. Rev. Lett.* **104**, 167203 (2010).
- <sup>141</sup>M. Ziese, F. Bern, E. Pippel, D. Hesse, and I. Vrejoiu, *Nano Lett.* **12**, 4276 (2012).
- <sup>142</sup>M. Ziese, F. Bern, and I. Vrejoiu, *J. Appl. Phys.* **113**, 063911 (2013).
- <sup>143</sup>M. Ziese, E. Pippel, E. Nikulina, M. Arredondo, and I. Vrejoiu, *Nanotechnology* **22**, 254025 (2011).
- <sup>144</sup>S. R. Singamaneni, J. T. Prater, and J. Narayan, *Appl. Phys. Lett.* (submitted).
- <sup>145</sup>S. R. Singamaneni, W. Fan, J. T. Prater, and J. Narayan, *J. Appl. Phys.* **117**, 17B711 (2015).
- <sup>146</sup>S. R. Singamaneni, J. T. Prater, F. Wu, and J. Narayan, *MRS Commun.* (to be published).
- <sup>147</sup>S. R. Singamaneni, J. T. Prater, and J. Narayan, *Curr. Opin. Solid State Mater. Sci.* **19**, 301 (2015).
- <sup>148</sup>J.-S. Lee, D. A. Arena, P. Yu, C. S. Nelson, R. Fan, C. J. Kinane, S. Langridge, M. D. Rossell, R. Ramesh, and C.-C. Kao, *Phys. Rev. Lett.* **105**, 257204 (2010).
- <sup>149</sup>S. Kolesnik, Y. Z. Yoo, O. Chmaissem, B. Dabrowski, T. Maxwell, C. W. Kimball, and A. Genis, *J. Appl. Phys.* **99**, 08F501 (2006).
- <sup>150</sup>Q. Gan, R. A. Rao, C. B. Eom, L. Wu, and F. Tsui, *J. Appl. Phys.* **85**, 5297 (1999).
- <sup>151</sup>X. Qi and S. Zhang, *Phys. Today* **63**(1), 33–38 (2010).
- <sup>152</sup>H. Peng, K. Lai, D. Kong, S. Meister, Y. Chen, X. Qi, S. Zhang, Z. Shen, and Y. Cui, *Nat. Mater.* **9**, 225–229 (2010).
- <sup>153</sup>C. Brune, A. Roth, E. Novik, M. Konig, H. Buhmann, E. M. Hankiewicz, W. Hanke, J. Sinova, and L. W. Molenkamp, *Nat. Phys.* **6**, 448–454 (2010).
- <sup>154</sup>K. Kuroda, G. Eguchi, K. Shirai, M. Shiraishi, M. Ye, K. Miyamoto, T. Okuda, S. Ueda, M. Arita, H. Namatame, M. Taniguchi, Y. Ueda, and A. Kimura, *Phys. Rev. B* **91**, 205306 (2015).
- <sup>155</sup>A. A. Sukhanov and V. A. Sablikov, *J. Phys.: Condens. Matter* **24**, 405301 (2012).
- <sup>156</sup>M. Klinenberg, “The search for strong topological insulators,” preprint [arXiv:1007.4838v1](https://arxiv.org/abs/1007.4838v1) (2010).
- <sup>157</sup>A. Widera and H. Schäfer, *Mater. Res. Bull.* **15**, 1805–1809 (1980).
- <sup>158</sup>Y. F. Lee, F. Wu, R. Kumar, F. Hunte, J. Schwartz, and J. Narayan, *Appl. Phys. Lett.* **103**, 112101 (2013).
- <sup>159</sup>Y. F. Lee, J. Narayan, and J. Schwartz, *J. Appl. Phys.* **116**, 164903 (2014).
- <sup>160</sup>Y. F. Lee, F. Wu, J. Narayan, and J. Schwartz, *MRS Commun.* **4**, 7–13 (2014).
- <sup>161</sup>S. Nori, T. H. Yang, and J. Narayan, *JOM* **63**, 29–33 (2011).
- <sup>162</sup>M. T. Greiner, L. Chai, M. G. Helander, W.-M. Tang, and Z.-H. Lu, *Adv. Funct. Mater.* **22**, 4557 (2012).
- <sup>163</sup>A. Klein, C. Körber, A. Wachau, F. Sauberlich, Y. Gassenbauer, S. P. Harvey, D. E. Proffit, and T. O. Mason, *Materials* **3**, 4892 (2010).
- <sup>164</sup>M. G. Mason, L. S. Hung, C. W. Tang, S. T. Lee, K. W. Wong, and M. Wang, *J. Appl. Phys.* **86**, 1688 (1999).
- <sup>165</sup>P. F. Carcia, R. S. McLean, M. H. Reilly, and G. Nunes, Jr., *Appl. Phys. Lett.* **82**, 1117 (2003).
- <sup>166</sup>C. Ronning, P. X. Gao, Y. Ding, Z. L. Wang, and D. Schwen, *Appl. Phys. Lett.* **84**, 783 (2004).
- <sup>167</sup>Q. Wan, Q. H. Li, Y. J. Chen, T. H. Wang, X. L. He, J. P. Li, and C. L. Lin, *Appl. Phys. Lett.* **84**, 3654 (2004).
- <sup>168</sup>Y. C. Yang, F. Pan, Q. Liu, M. Liu, and F. Zeng, *Nano Lett.* **9**, 1636 (2009).
- <sup>169</sup>M. V. Ponomarev, M. A. Verheijen, W. Keuning, M. C. M. van de Sanden, and M. Creatore, *J. Appl. Phys.* **112**, 043708 (2012).
- <sup>170</sup>R. Groenen, J. Loffler, J. L. Linden, R. E. I. Schropp, and M. C. M. van de Sanden, *Thin Solid Films* **492**, 298–306 (2005).
- <sup>171</sup>S. Mal, S. Nori, J. Narayan, and J. T. Prater, *J. Mater. Res.* **26**, 1298 (2011).

- <sup>172</sup>X. H. Wei, Y. R. Li, J. Zhu, A. W. Huang, Y. Zhang, W. B. Luo, and H. Ji, *Appl. Phys. Lett.* **90**, 151918 (2007).
- <sup>173</sup>S.-B. Mi, *Thin Solid Films* **558**, 237–240 (2014).
- <sup>174</sup>J.-S. Tian, M.-H. Liang, Y.-T. Ho, Y.-A. Liu, and L. Chang, *J. Cryst. Growth* **310**, 777–782 (2008).
- <sup>175</sup>R. Molaei, M. R. Bayati, H. M. Alipour, and J. Narayan, *Appl. Phys. Lett.* **102**, 101602 (2013).
- <sup>176</sup>P. Gupta and J. Narayan, *J. Appl. Phys.* **115**, 043513 (2014).
- <sup>177</sup>R. Cusco, E. Alarcon-Llado, J. Ibanez, L. Artus, J. Jimenez, B. G. Wang, and M. J. Callahan, *Phys. Rev. B* **75**, 165202 (2007).
- <sup>178</sup>R. Aggarwal, H. Zhou, C. Jin, J. Narayan, and R. J. Narayan, *J. Appl. Phys.* **107**, 113530 (2010).
- <sup>179</sup>K. Vanheusden, W. L. Warren, C. H. Seage, D. R. Tallent, J. A. Voigtang, and B. E. Gnade, *J. Appl. Phys.* **79**, 7983 (1996).
- <sup>180</sup>S.-H. Jeong, B.-S. Kim, and B.-T. Lee, *Appl. Phys. Lett.* **82**, 2625 (2003).
- <sup>181</sup>W.-R. Liu, Y.-H. Li, W. F. Hsieh, C.-H. Hsu, W. C. Lee, Y. J. Lee, M. Hong, and J. Kwo, *Cryst. Growth Des.* **9**, 239 (2009).
- <sup>182</sup>T. I. Wong, H. R. Tan, D. Sentosa, L. M. Wong, S. J. Wang, and Y. P. Feng, *J. Phys. D: Appl. Phys.* **45**, 415306 (2012).
- <sup>183</sup>X. N. Wang, Y. Wang, Z. X. Mei, J. Dong, Z. Q. Zeng, H. T. Yuan, T. C. Zhang, X. L. Du, J. F. Jia, Q. K. Xue, X. N. Zhang, Z. Zhang, Z. F. Li, and W. Lu, *Appl. Phys. Lett.* **90**, 151912 (2007).
- <sup>184</sup>F. J. Morin, *Phys. Rev. Lett.* **3**, 34 (1959).
- <sup>185</sup>K. Martens, N. Aetuksi, J. Jeong, M. G. Samant, and S. S. P. Parkin, *Appl. Phys. Lett.* **104**, 081918 (2014).
- <sup>186</sup>D. Ruzmetov and S. Ramanathan, *Thin Film Metal Oxides: Fundamentals and Applications in Electronics and Energy* (Springer, New York, 2010).
- <sup>187</sup>J. de la Venta, S. Wang, J. G. Ramirez, and I. K. Schuller, *Appl. Phys. Lett.* **102**, 122404 (2013).
- <sup>188</sup>R. Molaei, R. Bayati, S. Nori, D. Kumar, J. T. Prater, and J. Narayan, *Appl. Phys. Lett.* **103**, 252109 (2013).
- <sup>189</sup>R. Molaei, R. Bayati, F. Wu, and J. Narayan, *J. Appl. Phys.* **115**, 164311 (2014).
- <sup>190</sup>G. M. Foley, S. R. Singamaneni, J. Prater, and J. Narayan, “Control of magnetic coercivity in epitaxial Ni/VO<sub>2</sub>/YSZ/Si(001) heterostructures by manipulation of Ni thin film growth modes,” *MRS Adv.* (published online).
- <sup>191</sup>A. Gupta, R. Aggarwal, P. Gupta, T. Dutta, R. J. Narayan, and J. Narayan, *Appl. Phys. Lett.* **95**, 111915 (2009).
- <sup>192</sup>J. Narayan and V. M. Bhosle, *J. Appl. Phys.* **100**, 103524 (2006).
- <sup>193</sup>W. Yin, S. Wolf, C. Ko, S. Ramanathan, and P. Reinke, *J. Appl. Phys.* **109**, 024311 (2011).
- <sup>194</sup>B. Lazarovits, K. Kim, K. Haule, and G. Kotliar, *Phys. Rev. B* **81**, 115117 (2010).
- <sup>195</sup>E. Fujii, A. Tomozawa, H. Torii, and R. Takayama, *Jpn. J. Appl. Phys., Part 2* **35**, L328 (1996).
- <sup>196</sup>M. Kitao, K. Izawa, K. Urabe, T. Komatsu, S. Kuwano, and S. Yamada, *Jpn. J. Appl. Phys., Part 1* **33**, 6656 (1994).
- <sup>197</sup>D. Adler and J. Feinleib, *Phys. Rev. B* **2**, 3112 (1970).
- <sup>198</sup>H. Sato, T. Minami, S. Takata, and T. Yamada, *Thin Solid Films* **236**, 27 (1993).
- <sup>199</sup>H. Kumagai, M. Matsumoto, K. Toyoda, and M. J. Obara, *J. Mater. Sci. Lett.* **15**, 1081 (1996).
- <sup>200</sup>X. Chen, N. J. Wu, L. Smith, and A. Ignatiev, *Appl. Phys. Lett.* **84**, 2700 (2004).
- <sup>201</sup>M. Stamataki, D. Tsamakis, N. Brilis, I. Fasaki, A. Giannoudakos, and M. Kompitsas, *Phys. Status Solidi A* **205**, 2064 (2008).
- <sup>202</sup>R. Molaei, R. Bayati, and J. Narayan, *Cryst. Growth Des.* **13**, 5459–5465 (2013).
- <sup>203</sup>S. S. Rao, Y. F. Lee, J. T. Prater, A. I. Smirnov, and J. Narayan, *Appl. Phys. Lett.* **105**, 042403 (2014).
- <sup>204</sup>S. Mal, J. Narayan, S. Nori, J. T. Prater, and D. Kumar, *Solid State Commun.* **150**, 1660 (2010).
- <sup>205</sup>M. R. Bayati, A. Z. Moshfegh, and F. Golestani-Fard, *Appl. Catal., A* **389**, 60 (2010).
- <sup>206</sup>K. Prashant, *J. Phys. Chem. C* **116**, 11849 (2012).
- <sup>207</sup>P. R. Ohodnicki, C. Wang, S. Natesakhawat, J. P. Baltrus, and T. D. Brown, *J. Appl. Phys.* **111**, 064320 (2012).
- <sup>208</sup>B. Santara, B. Pal, and P. K. Giri, *J. Appl. Phys.* **110**, 114322 (2011).
- <sup>209</sup>P. Chinnamuthu, J. C. Dhar, A. Mondal, A. Bhattacharyya, and N. K. Singh, *J. Phys. D: Appl. Phys.* **45**, 135102 (2012).
- <sup>210</sup>N. Naseri, M. Amiri, and A. Z. Moshfegh, *J. Phys. D: Appl. Phys.* **43**, 105405 (2010).
- <sup>211</sup>B. Xi, L. K. Verma, J. Li, C. S. Bhatia, A. J. Danner, H. Yang, and H. C. Zeng, *Appl. Mater. Interfaces* **4**, 1093 (2012).
- <sup>212</sup>M. R. Bayati, S. Joshi, R. Molaei, R. J. Narayan, and J. Narayan, *J. Appl. Phys.* **113**, 063706 (2013).
- <sup>213</sup>P. Gupta, T. Dutta, S. Mal, and J. Narayan, *J. Appl. Phys.* **111**, 013706 (2012).
- <sup>214</sup>T. V. Perevalov and V. A. Gritsenko, *J. Exp. Theor. Phys.* **112**, 310 (2011).
- <sup>215</sup>R. K. Singh and J. Narayan, *Mater. Sci. Eng., B* **3**, 217 (1989).
- <sup>216</sup>N. Sakai, A. Fujishima, T. Watanabe, and K. Hashimoto, *J. Phys. Chem. B* **105**, 3023 (2001).
- <sup>217</sup>C.-P. Chang, M.-W. Chu, H. T. Jeng, S.-L. Cheng, J. G. Lin, J.-R. Yang, and C. H. Chen, *Nat. Commun.* **5**, 3522 (2014).
- <sup>218</sup>N. Gauquelin, E. Benckiser, M. K. Kinyanjui, M. Wu, Y. Lu, G. Christiani, G. Logvenov, H.-U. Habermeier, U. Kaiser, B. Keimer, and G. A. Botton, *Phys. Rev. B* **90**, 195140 (2014).
- <sup>219</sup>Y.-M. Kim, A. Morozovska, E. Eliseev, M. P. Oxley, R. Mishra, S. M. Selbach, T. Grande, S. T. Pantelides, S. V. Kalinin, and A. Y. Borisevich, *Nat. Mater.* **13**, 1019 (2014).
- <sup>220</sup>A. Y. Borisevich, H. J. Chang, M. Huijben, M. P. Oxley, S. Okamoto, M. K. Niranjan, J. D. Burton, E. Y. Tsymbal, Y. H. Chu, P. Yu, R. Ramesh, S. V. Kalinin, and S. J. Pennycook, *Phys. Rev. Lett.* **105**, 087204 (2010).
- <sup>221</sup>T. J. Pennycook, M. P. Oxley, J. Garcia-Barriocanal, F. Y. Bruno, C. Leon, J. Santamaría, S. T. Pantelides, M. Varela, and S. J. Pennycook, *Eur. Phys. J.: Appl. Phys.* **54**, 33507 (2011).